VOLCANIC GEOLOGY OF MAUNGATAUTARI: AN ANDESITIC-DACITIC COMPOSITE CONE, CENTRAL WAIKATO, NEW ZEALAND

A thesis

submitted in partial fulfilment

of the requirements for the degree

of

Master of Science in **Earth Science**

at

The University of Waikato

by

Marlena Lee Prentice

THE UNIVERSITY OF
WAIKATO
Te Whare Wānanga o Waikato

2017

Abstract

Maungatautari is an extinct andesitic-dacitic composite cone volcano, situated 35 km southeast of Hamilton, that rises prominently in the Waikato region. A single radiometric age of 1.8 Ma, indicates volcanic activity here was contemporaneous with subduction-related volcanism of the nearby Alexandra Volcanics and the early Taupo Volcanic Zone. The geology and volcanism of Maungatautari was previously addressed (1950s-80s) in context of the broader volcanic geology of the Waikato region, however, only a single dedicated volcanic study, undertaken over 30 years ago, provided insight into the chemical composition and origin of the magmas. This study applied modern volcanological techniques and concepts to reconstruct the volcanic history of Maungatautari and how it may relate to volcanism elsewhere in the Waikato Region around 2 Ma. The work incorporates field and desktop geomorphic analysis, volcanic stratigraphy and facies analysis, petrographic and mineralogical studies, and elemental and isotopic geochemical analysis.

Maungatautari overlies Jurassic Manaia Hill group rocks of the Waipapa Terrane and abuts a range of the same rocks immediately to the west. It is surrounded to the north, east and south by a thick ignimbrite plateau which overlies the lowermost flanks of the mountain, originating from the Mangakino caldera to the southeast. Catastrophic failure of the northeastern flank produced a 0.28 km^3 rock avalanche deposit over an area of approximately 1.6 km^2. The deposits of rock falls, slides and debris flows were also commonly observed and demonstrate that numerous mass-wasting processes have continued to occur into the present.

Lavas at Maungatautari consist of non-vesicular labradorite, pyroxene and hornblende andesites and hornblende dacites along with olivine basalt at the small cone at Kairangi ~7 km to the northwest. Whole rock geochemical and strontium and neodymium analyses demonstrate these lavas were derived from at least three distinct mantle-melt sources: the fractionation of subduction-related, deep, garnet-bearing, depleted mantle (most andesites and dacites); a shallower,

garnet-free, upper mantle (low SiO_2 hornblende andesites) and an area of deeper enriched mantle (Kairangi olivine basalt). This study considers Maungatautari to reflect andesitic volcanism occurring along the edge of the continental tip of the Colville volcanic arc c. 2 Ma with the near-by Alexandra Volcanics being contemporaneous, behind-arc subduction-related volcanoes. The olivine basalt at Kairangi is more reflective of intraplate over subduction-related melts and is unrelated to magmatism at Maungatautari.

This study is the first to document a record of explosive volcanism at Maungatautari. Eruption styles which occurred at Maungatautari include the effusion of lava resulting in the generation of lava flows and domes, and vulcanian to sub-plinian explosive eruptions which produced both high and low particle concentration pyroclastic density currents.

Acknowledgements

This completion of this thesis comes at the end of nearly five years of continuous study, of which the last two years have been the most challenging and rewarding. This project would not have been possible without the encouragement, assistance and support I received from so many people. I am grateful for this opportunity to acknowledge and thank them.

I am indebted to my principle supervisor Dr Adrian Pittari for his guidance, constant support and hours spent editing chapters. Your door was always open and I thank you for providing me with such a mentally and physically challenging project in which I could play an active role in its planning and direction. I am also thankful for the guidance and advice provided by Dr Shaun Barker and Dr Vicki Moon during field work and geochemical data collection. This research would not have been possible without the expertise and guidance provided by the School of Sciences technical staff; Annette Rodgers, Kirsty Vincent, Renat Radosinksy and Steve Cameron, along with Bruce Charlier and staff from Victoria University of Wellington.

I would like to acknowledge the Waipa District Council, Maungatautari Ecological Island Trust (MEIT), Ngāti Korokī Kahukura along with Ruakawa, Tainui and Ngāti Hauā for granting consent for this study to take place within the confines of the reserve. Practical support within the sanctuary was provided by James Matthews and Craig Laxon. Thank you to Bill Garland, John Scott and Katie and Mo who demonstrated great passion towards the geology and conservation of this national treasure and provided transportation around their farms and allowed me to run around with a sledgehammer collecting rocks, and to the numerous other individual land owners who granted me access to their land.

Thank you to my fellow earth science students at the University of Waikato. The endless discussions and procrastination made a stressful time more enjoyable. Thanks to Oliver McLeod for field assistance and the constant discussion/comparison of our separate, yet semi-related projects.

Funding was received from the University of Waikato Masters Research Scholarship, University of Waikato Taught Postgraduate Scholarship, Science and Engineering Masters Fees Award and the Waikato Graduate Women Educational Trust Masters Study Award.

Finally, a special thank you to my friends and family for putting up with me and listening to my endless talk about this project. I could not have managed this achievement without the constant support and love of my husband Glen and daughters Evelyn and Felicity, to whom I hope I have demonstrated that anything is possible with determination and hard work.

I dedicate this work to my late mother Jeannette, who encouraged me to never give up and reminded me of the importance to experience all life has to offer. You are forever loved and will always be missed xoxo.

Table of Contents

List of Figures

Chapter One: Introduction

Chapter Two: Literature Review

Chapter Three: Geology and Geomorphology

Chapter Five: Physical Volcanology of Two Pyroclastic Successions

List of Tables

Chapter Four: Petrology of Lavas

Chapter One:

Introduction

1.1 Introduction

Composite cones occur in all tectonic environments, however, they are most typically found at subduction zones where the repeated eruption of lava and pyroclastic deposits from a central vent creates a broadly conical edifice. While a range of magma compositions may be observed at a single composite cone, they are typically constructed from viscous intermediate to silicic magmas of andesitic to dacitic composition. The simple conical shape of these volcanoes, however, often belies the complex interplay of different volcanic and sedimentary processes which occur throughout the history of a single edifice.

Maungatautari is an extinct andesitic-dacitic composite cone volcano that rises prominently in the Waikato region. With a single radiometric age date of 1.8 Ma (Robertson, 1983), activity at Maungatautari was contemporaneous with subduction-related volcanism of the nearby Alexandra Volcanics and the early Taupo Volcanic Zone. Maungatautari volcanism was previously addressed in context of the broader volcanic geology of the Waikato region (Cole, 1978; Kear, 1964; Olson, 1950), and the only dedicated volcanic study of Maungatautari (Briggs, 1986b) provided insight into the chemical composition and origin of the magmas.

Despite the development of new techniques and scientific thinking in the last 30 years, no further volcanological studies relating to Maungatautari have been undertaken.

1.2 Research Aim and Objectives

This study aims to apply modern volcanological techniques and concepts to assess the volcano to provide an improved understanding on the volcanic history of the mountain and how it may relate to volcanism elsewhere in the Waikato Region during this time.

The single age date of Robertson (1983) is poorly constrained, and no previous studies have attempted to determine the range of eruption styles associated with

the volcano. Furthermore, recent track construction has uncovered rock exposures in areas of the mountain which have never before been studied.

Therefore, the objectives for this study are to;

- re-assess and map the major geological and geomorphological components of Maungatautari and immediate surrounds using field observation and GIS software,
- petrographic and whole rock elemental and isotopic characterisation of the Maungatautari lavas, and
- assessment of the physical volcanology of Maungatautari pyroclastic successions

Each year, thousands of people of all ages visit Sanctuary Mountain Maungatautari to learn about the native flora and fauna which makes it unique. The findings of this study will add to the visitor experience by highlighting the volcanic origins of the mountain and help increase public awareness of the local landscape and natural history of this unique environment.

1.3 Methods

The following methodology was used to achieve the above objectives: (1) field work which included field mapping, descriptions of outcrop and hand specimens and stratigraphic logging of pyroclastic sequences, (2) desktop GIS studies, and (3) laboratory analysis, including optical microscopic petrography of thin sections, component point counting, X-ray powder diffraction, whole-rock geochemistry (X-ray fluorescence spectroscopy, laser ablation inductively coupled plasma mass spectrometry and strontium and neodymium isotope analysis.

Detailed descriptions of each method are presented in each of their respective chapters. Additional raw data are presented in the appendices.

1.4 Study Area

Maungatautari is a bush-covered, andesitic-dacitic composite cone situated 35 km southeast of Hamilton within the Waipa District, Waikato (Figure 1.1). The investigation site is centered on Mt Maungatautari with the Pukekura Hills and Oreipunga Road respectively defining the western and eastern boundaries. The northern limit is the top of Hicks Road which provides access to the Northern Enclosure and to the south it is Arapuni Road.

The introduction of rabbits and possums in the 1950's was highly devastating to the native bush and wildlife of the area. In recent years, great effort has been made to restore this unique environment to its natural state. The construction of a 47 km-long, predator-proof fence enclosing 34 km^2 of the mountain's upper slopes, creates an environment where native trees and ferns have been able to grow uninhibited. As a result, re-introduced bird populations are now flourishing, creating the largest ecological island on the mainland of New Zealand (Maungatautari Ecological Island Trust, 2010). The lower slopes are mostly privately owned lands covered in pasture for livestock grazing.

Figure 1.1. Image of the central North Island showing the location of Maungatautari and the field area (red box) in relationship to three main population centres – Auckland, Hamilton and Tauranga (Google Earth 2017).

1.5 Thesis structure and chapter outline

Chapter 2 is a review of literature relevant to the regional geology and includes a brief overview of the geologic evolution of the New Zealand, current tectonic setting and descriptions of the volcanic fields of the central and western North Island where active volcanism occurred prior to and/or contemporaneous with Maungatautari.

Chapter 3 describes the general geology and geomorphology of the mountain with emphasis on the description and stratigraphical relationships between units and the deposits of various mass-wasting processes.

Chapter 4 presents the mineralogical descriptions of the various rock types based on petrographic microscopy and the results of X-ray powder diffraction and whole-rock major, trace, REE and strontium and neodymium elemental analysis.

Chapter 5 describes the location, field and facies characteristics and componentry of Maungatautari eruptive deposits which are then interpreted to define possible eruption styles and eruptive processes associated with the volcano.

Chapter 6 is a summary of the main findings and interpretation of the overall study and how these compare with current understandings.

Chapter Two:

Literature Review

2.1 Structural evolution and geological setting of New Zealand

The present-day plate tectonic regime of New Zealand (Figure 2.1) consists of subduction of the Pacific Plate underneath the Australian plate along the Hikurangi Trench, transpressive transform faulting forming the Southern Alps and subduction of the Australian Plate beneath the Pacific Plate at the Puysegur Trench. However, this current setting is a geologically recent phenomenon, and this simplistic description masks the complex geological evolution which has occurred over the last 100 - 80 million years.

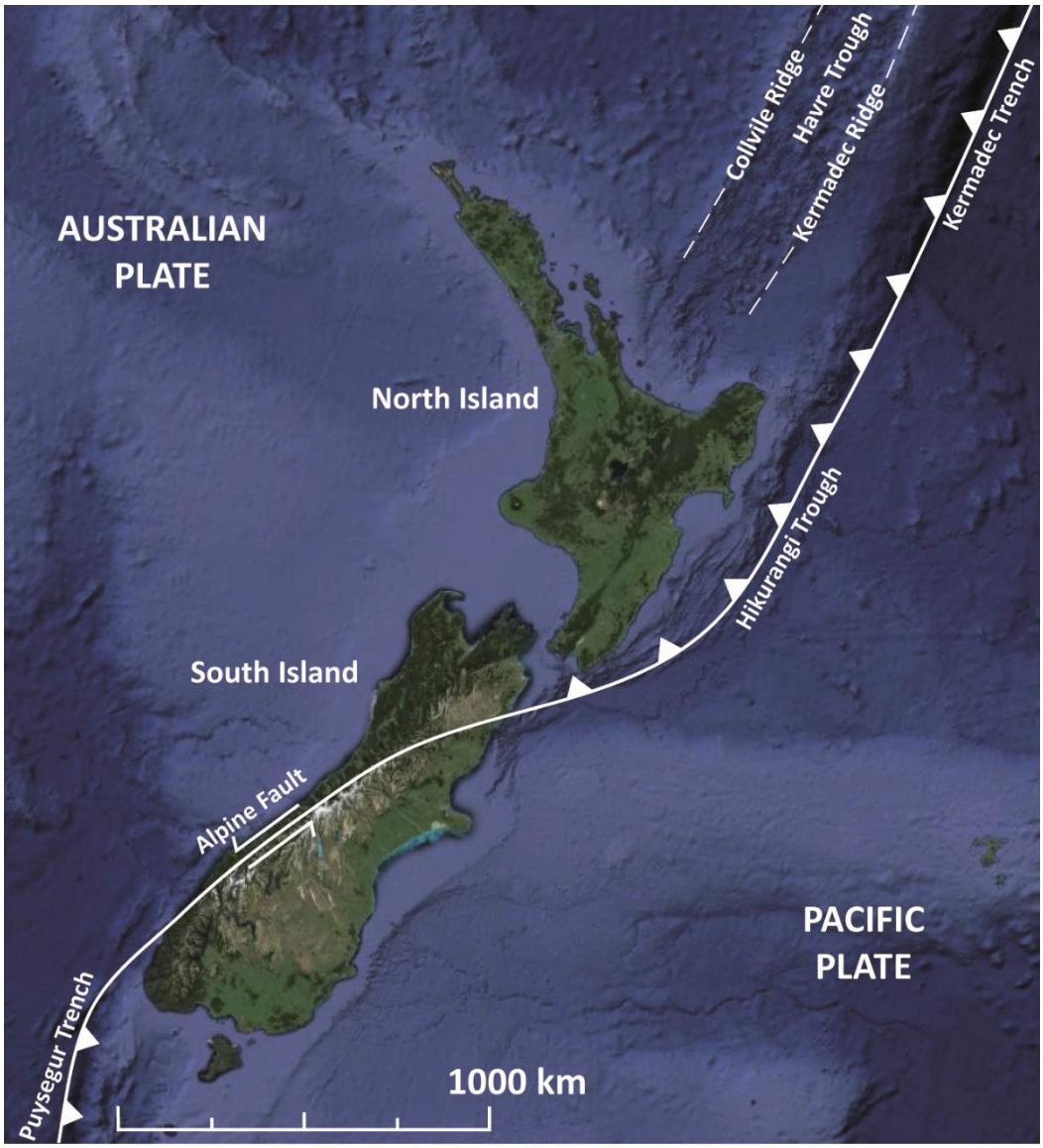

Figure 2.1. Present tectonic setting and important geological features of New Zealand. Base image taken from Google Earth ™

The sedimentary, metamorphic and igneous rocks which comprise the basement of New Zealand are divided into two broad groups, the Western and Eastern Provinces consisting of mainly granite and gneiss, and greywacke and schist respectively. The Eastern Province is subdivided into eight regional terranes which originated from sediment being scraped off the top of a subducting oceanic plate into an accretionary wedge, adding to the eastern Gondwana landmass over several hundred million years (Mortimer, 2008). These terranes were uplifted, folded and faulted during an extended period of continental extension during the breakup of Gondwana about 85 Ma. Eventually a fragment of continental crust was broken off and pushed north and east by newly formed oceanic crust to create the continent of Zealandia. After separation, lithospheric cooling resulted in gradual subsidence during which time cover rocks, consisting of mostly thick sequences of marine sediments, were deposited (Campbell *et al.*, 2014).

Varying relative rotation of both the Australian and Pacific Plates, and the simultaneous formation of the plate boundary has influenced the development of virtually all parts of New Zealand (Furlong & Kamp, 2009; King, 2000), especially the location and duration of active volcanic fields. Intra-plate volcanic activity was widespread throughout the South Island during the Paleogene (65-24 Ma), before becoming sporadic and confined to relatively small areas (Cole, 1986; Smith & Briggs, 2008). A change in relative plate motion during the Eocene led to the initiation of subduction to the north between the Reinga Basin and New Caledonia 45–30 Ma. Synchronous with this, was the onset of extension to the south (Bache *et al.*, 2012). Throughout this time, New Zealand remained part of a single plate until the propagation of a convergent margin through New Zealand (30 – 20 Ma), and the creation of the Alpine Fault which linked the subduction zones within the Pacific and Australian plates to the north and south respectively (Furlong & Kamp, 2009).

North Island arc-related volcanism began in Northland c. 25-23 Ma, forming two volcanic belts - a narrow eastern frontal belt (23-11 Ma) and a broad western belt (25-15.5 Ma) which included both subaerial and submarine volcanic edifices

(Hayward *et al.*, 2001). This Northland Volcanic Arc is believed to have extended at least 500 km to the northwest to include the Eocene to late Miocene volcanoes of the Loyalty and Three Kings ridges (Hayward *et al.*, 2001; Herzer *et al.*, 2009) (Figure 2.2). Backarc extension expressed by the opening of Norfolk Basin was accommodated along the Vening Meinesz Fracture Zone (VMFZ) – a NW trending transform fault delineating the New Zealand continental crust with oceanic crust to the north. As a result, the Three Kings Ridge has been displaced eastwards (Herzer & Mascle, 1996). Parallel deformation to the north of the VMFZ is well documented (Herzer *et al.*, 2011; Herzer *et al.*, 2009; Mortimer *et al.*, 2007) and is believed to also extend south into northern continental New Zealand (Wilson & Rowland, 2016). Over the past 15 million years, arc-related volcanism has continued to migrate south and eastwards forming the Colville-Coromandel arc and the presently active Kermadec-Tonga Ridge (Furlong & Kamp, 2009; Giba *et al.*, 2010; Herzer *et al.*, 2009; Herzer & Mascle, 1996; Seebeck *et al.*, 2014).

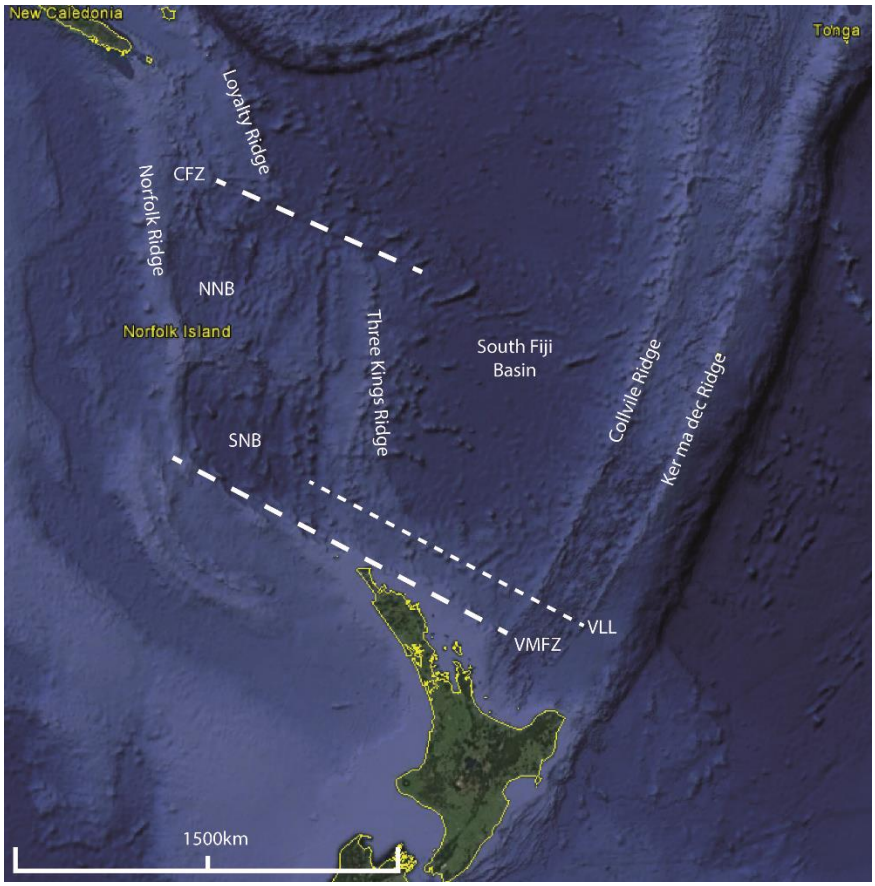

Figure 2.2. Northern continental margin of New Zealand identifying major geographic features. VMFZ = Vening Meinesz Fracture Zone, VLL = van der Linden Lineament, SNB = South Norfolk Basin, NFB = North Fiji Basin, CFZ = Cook Fracture Zone. Base image taken from Google Earth ™

2.2 Volcanic regions of the North Island

The central North Island contains 11 distinct volcanic zones (Figure 2.3) resulting from either subduction or intraplate processes. Intraplate volcanism is confined exclusively along the west coast within four distinct volcanic fields (Auckland, South Auckland, Ngatutura and Okete) that comprise the Auckland Volcanic Province. Subduction-related predominately andesitic volcanism is located off shore along the western margin of the Taranaki Basin (Giba *et al.*, 2010), while to the east, separated by the Waikato Basin and the Hauraki Rift, is the predominately rhyolitic volcanism of the Coromandel and Taupo volcanic zones. Lying between is found the basaltic-andesitic volcanism of the Alexandra, Maungatautari and Kiwitahi volcanic groups of the Waikato region (Cole *et al.*, 2008).

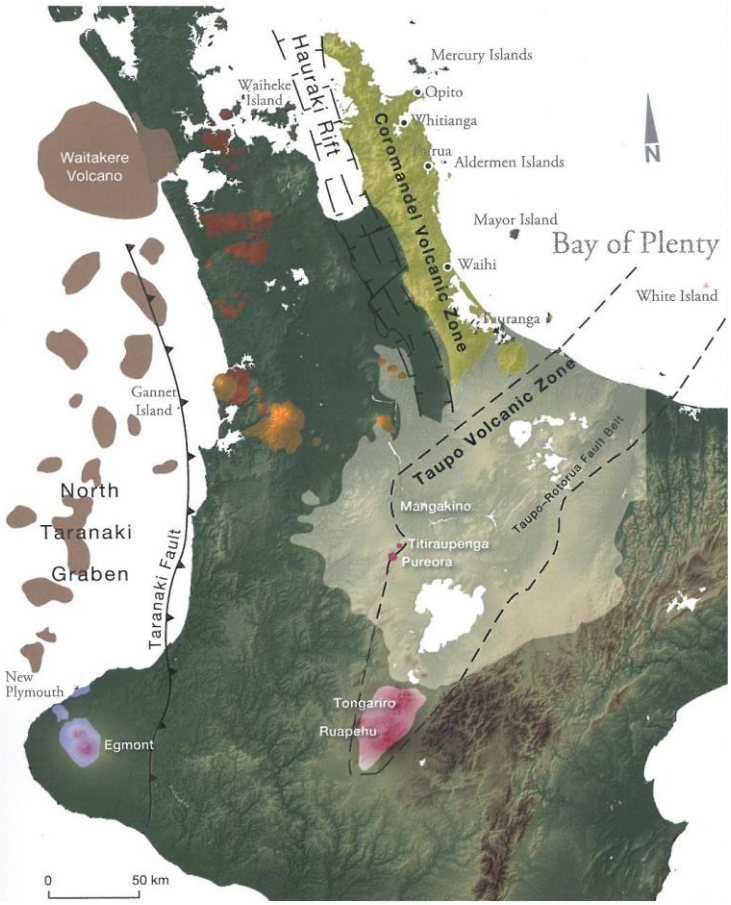

Figure 2.3. Volcanic zones of the central North Island, New Zealand. Auckland Volcanic Province (including Auckland, South Auckland, Ngatutura and Okete Volcanic fields) = Red. Alexandra, Maungatautari and Kiwitahi volcanics = orange. North Taranaki Graben volcanics = brown. Coromandel Volcanic Zone = yellow. Taranaki Volcanic Lineament = purple and the currently active Taupo Volcanic Zone (Cole et al., 2008).

2.2.1 Auckland Volcanic Province

The Auckland Volcanic Province consists of a series of volcanic fields which includes the currently active Auckland field (0.14 Ma-500 yrs ago), and the extinct fields of South Auckland (1.59-0.51 Ma), Ngatutura (1.83-1.54 Ma) and Okete (2.69-1.8 Ma). Activity began within the Okete Volcanic Field where deposits are interbedded with lavas from nearby Mt Karioi of the Alexandra Volcanic Group. Once activity ceased c. 1.8 Ma, volcanism migrated to the north eventually creating a chain of monogenetic fields which are progressively younger from south to north (Briggs *et al.*, 1994).

While the volcanic arcs and many isolated volcanoes found throughout the North Island are directly linked to subduction, the fields of the Auckland intra-plate province lie behind the present-day convergent boundary, approximately 350 – 400 km to the northwest (Weaver & Smith, 1989). Spaced 35-38 km apart, these fields are spatially and geochemically distinct from nearby arc volcanoes and are dominated by basaltic monogenetic, phreatomagmatic or magmatic eruptions producing maars and tuff rings or scoria cones, lava flows and occasional shield volcanoes respectively (Briggs *et al.*, 1994; Smith & Briggs, 2008). Rafferty and Heming (1979) proposed that the origin of intra-plate volcanism of the SAVF was the progressive melting of a mantle diapir rising through a zone of low velocity in the upper mantle. Heming (1980) published a further paper which focused on the temporal changes in geochemistry from early alkaline to later tholeiitic magmas. This linked the diapir model to convection in the mantle wedge behind the New Zealand volcanic arc which was then extended to the remaining volcanic fields within the Auckland and Northland provinces. More recent studies (Briggs *et al.*, 1994; Cook *et al.*, 2005) have discounted the diapir model and concluded no link between magmatic geochemistry and the temporal and spatial variations found between or among the volcanic complexes comprising each field. As magmas show no geochemical relationship to subduction, it is now thought that the northward-migrating magma source of the Auckland Province, results from decompression melting of the sub-continental lithospheric mantle due to back-arc spreading associated with the southward migrating active subduction margin.

The link between faulting, magmatism and the location of volcanic vents is well established in literature (Briggs *et al.*, 1994; Rafferty, 1977; Rafferty & Heming, 1979). Within the South Auckland Field faults, resulting from tensional stresses associated with back-arc spreading, have provided an easy route to the surface for magmas formed due to decompression (Rafferty, 1977). Over one third of volcanoes are aligned along known faults, and offset volcanic centres may be explained by dike-sill complexes which formed at points where faults intersect joints or bedding structures or by faults now buried under younger volcanic deposits and landforms (Briggs *et al.*, 1994).

2.2.2 North Taranaki Graben Volcanics

The buried andesitic submarine volcanoes and associated intrusions of the Mohakatino Volcanic Centre in the North Taranaki Graben, form a continuous chain that extends south from the western volcanoes of the Northland Volcanic Arc (Figure 2.2;Figure 2.3) (King & Thrasher, 1996). Identified by the interpretation of seismic reflection profiles, volcanic centres are oriented in an approximately NNE–SSW direction and are mostly cone-shaped, semi-circular to ovoidal edifices with diameters ranging from 2 to 40 km, with the largest of centres likely to be composite structures of two or more individual cones (Giba *et al.*, 2013; King & Thrasher, 1996). Samples obtained from drilled offshore exploration wells show mainly low- to med-K, calcalkaline basaltic andesite and andesite compositions commonly associated with subduction-related volcanism, consistent with an arc origin related to the subducting Pacific Plate along the Hikurangi margin (Giba *et al.*, 2010; Gill, 1981; King & Thrasher, 1996).

Andesitic volcanism commenced in the northern part of the basin at ~16 Ma, with the development of normal faulting from ~12 Ma (Figure 2.4). During this time, contraction continued in the southern part of the basin (Giba *et al.*, 2010). Over the next 12 Ma, this general pattern of volcanism followed by extension migrated southward (Ballance, 1976; Giba *et al.*, 2010; Herzer, 1995; Kear, 1994), until ~4 Ma, when displacement rates in the northern basin slowed

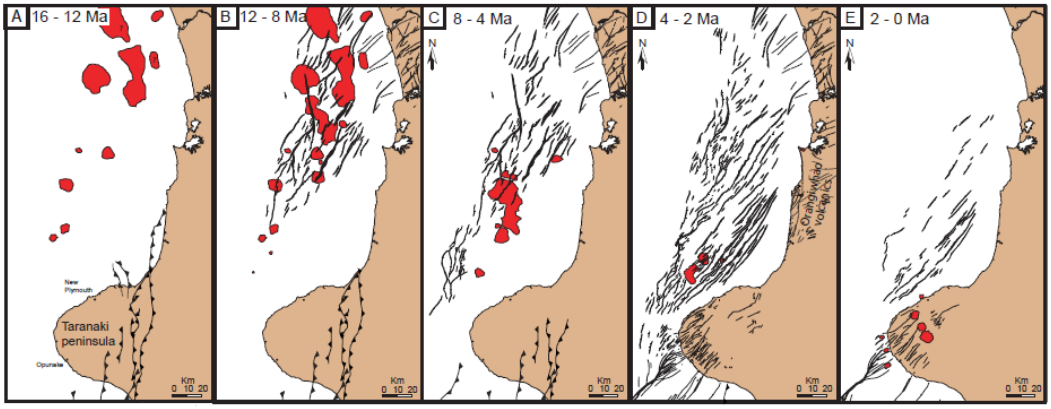

Figure 2.4. Tectonic-volcanic evolution of the Taranaki Basin. For the time period indicated, each map, A-E, displays active volcanoes in red and active normal and reverse faults with black lines. Maps highlight the general southward migration of volcanism and faulting within the basin (Giba et al., 2013).

before finally ceasing at ~2 Ma (Giba *et al.*, 2010). This pattern of southward migration of andesitic volcanism and rifting is mirrored within the Coromandel and Taupo volcanic zones (Figure 2.5A) and consistent with the clockwise rotation and eastward migration of the subduction margin due to progressive steepening and slab roll-back (Figure 2.5B) (Giba *et al.*, 2013; Seebeck *et al.*, 2014).

Today, the only remaining active cone within the Taranaki region is the southernmost and onshore volcano of Mt Taranaki.

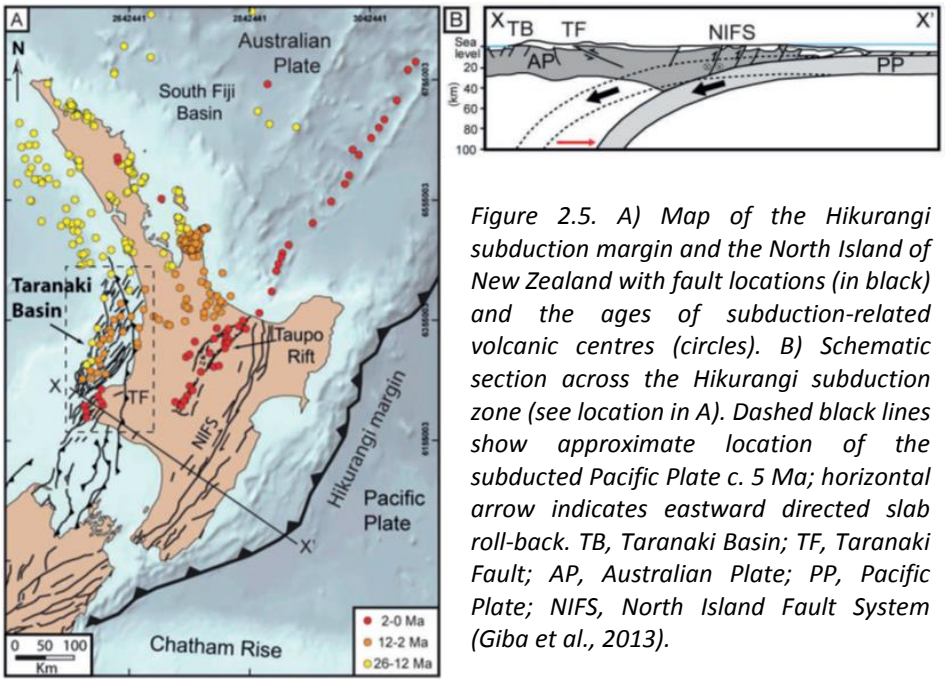

Figure 2.5. A) Map of the Hikurangi subduction margin and the North Island of New Zealand with fault locations (in black) and the ages of subduction-related volcanic centres (circles). B) Schematic section across the Hikurangi subduction zone (see location in A). Dashed black lines show approximate location of the subducted Pacific Plate c. 5 Ma; horizontal arrow indicates eastward directed slab roll-back. TB, Taranaki Basin; TF, Taranaki Fault; AP, Australian Plate; PP, Pacific Plate; NIFS, North Island Fault System (Giba et al., 2013).

2.2.3 Coromandel Volcanic Zone

The Coromandel Volcanic Zone (CVZ) covers both the Coromandel and Kaimai Ranges and includes a wide range of igneous rocks from basalt to rhyolite. Volcanism began during the mid Miocene (c. 18 Ma) and was andesitic in nature (Adams *et al.*, 1994; Booden *et al.*, 2012). Preserved in resistant lava flows and dikes, remnants of these long eroded volcanoes are found in the north of the field. Around 12 Ma, activity in the CVZ evolved to include rhyolitic volcanism which began to migrate SSE toward the central North Island until c. 2 Ma when activity ceased (Adams *et al.*, 1994; Booden *et al.*, 2012; Briggs *et al.*, 2005; Cole *et al.*, 2008). The north-south orientation of the Coromandel peninsula is believed to be a feature imposed on the area by the faulting associated with the development of the Hauraki Rift and not a reflection of a fundamental north-south alignment of volcanic structures (Wilson & Rowland, 2016). As such volcanism throughout the region reflects the southeast migration of a NNE-SSW-trending arc.

The Tauranga Volcanic Centre was active between 2.7-1.9 Ma and represents the final phase of silicic volcanism within the CVZ before activity transferred south to the newly formed Taupo Volcanic Zone (Briggs *et al.*, 2005). However, unlike areas further north, there is no evidence of a caldera within the Tauranga Basin. This transition marks a significant time in the volcanic and tectonic history of New Zealand and includes the commencement of volcanism which led to the development of the present Kermadec Ridge, the Hauraki Rift and extensional block faulting of the western North Island (Figure 1).

Briggs *et al.* (2005) divides the rhyolite domes and flows of the Tauranga Volcanic Centre into four groups (Minden Peak, Mount Maunganui, Mangatawa and Mount Misery) based on spatial, mineralogical and geochemical characteristics. The youngest rocks include the Upper Papamoa Ignimbrite, Puwhenua and Otanewainuku lava domes of the Mangatawa Group and the Minden Peak lava dome which consist of hornblende-orthopyroxene rhyolites and dacites and hornblende rhyolite respectively. These predate all known silicic activity within the TVZ but have calc-alkaline compositions with similar major and trace element

and isotopic compositions, suggesting a similar magmatic origin involving fractionation and partial melting of continental crust.

2.2.4 Taupo Volcanic Zone

The Taupo Volcanic Zone (TVZ) has been defined by the location of known volcanic centres and is c. 350 km long and up to 100 km wide at the northern end, with ongoing rifting currently estimated at 7-12 mm per year (Cole *et al.*, 2008; Wilson *et al.*, 1995). The northern and southern ends are marked by the andesitic composite cones of White Island, and Ruapehu and Tongariro respectively. Rhyolitic caldera volcanoes dominate the central region and have produced numerous large ignimbrite sheets which extend well beyond the boundaries of the zone (Figure 2.3).

Titiraupenga and Pureora

Activity began c. 2 Ma along the western margin of the TVZ at the now-eroded volcanoes of Titiraupenga and Pureora with the eruption of basaltic-andesite to andesites characteristically low in K_2O and MgO-rich. Strongly porphyritic, the phenocryst population consists of plagioclase, clinopyroxene and orthopyroxene with glomeroporphyritic textures (Cole & Teoh, 1975; Froude & Cole, 1985).

Mangakino Caldera

Rhyolitic activity began with the development of the Mangakino caldera c. 1.6 Ma, and has migrated east over time (Booden *et al.*, 2010; Briggs, 1986b; Cole *et al.*, 2008; Wilson *et al.*, 1995). This trend mirrors the development of the CVZ, and may be linked to crustal extension resulting from rifting (Booden *et al.*, 2012). While the recent history of the TVZ is reasonably well established, that of older centres such as Mangakino have proved more challenging due to erosion and the subsequent burial by younger deposits from centres located to the east. However, seven major welded ignimbrites, along with voluminous fall deposits and rhyolitic lava domes have been attributed to this centre. The largest eruptions occurred in two periods of caldera-forming activity during 1.68-1.53 Ma and 1.21-0.95 Ma, the

deposits of which are widely distributed over the North Island (Briggs *et al.*, 1993; Krippner *et al.*, 1998).

At Maungatautari, the 1.21 Ma Ongatiti Ignimbrite (Wilson *et al.*, 2008) is known to lie unconformably above the Jurassic basement and volcanically-derived sedimentary breccias and lahar deposits, and can be found outcropping along the edges of the Waikato River within the Maungatautari Gorge (Olissoff, 1981). Overlying this, are the younger ignimbrites of the Mangaokewa and Raepahu Formations found to the south and east respectively.

The Mangaokewa Formation consists of two ignimbrite units which can be found to the south and southeast of the mountain (Figure 3.6). The lower Unit D is a firm, non-welded and pumice-poor ignimbrite and phreatomagmatic fall sequence and has a U-Pb zircon date of 1.2 Ma (Wilson *et al.*, 2008). The upper unit is the 1.18 Ma Ahuroa ignimbrite (Wilson *et al.*, 2008), which is hard, welded and eutaxitic (Leonard *et al.*, 2010).

The youngest ignimbrite units originating from Mangakino caldera are those of the Raepahu Formation which consists of upper Rocky Hill (1.00 Ma) and lower Kidnappers ignimbrite and fall deposit (1.01-1.02 Ma) (Wilson *et al.*, 2008). The Kidnappers fall deposit contains accretionary lapilli and is overlain by a non-welded biotite-rich ignimbrite while the Rocky Hill ignimbrite is a creamy grey, poorly to non-welded, crystal-rich, lithic-poor, lenticular pumiceous ignimbrite (Leonard *et al.*, 2010).

Geochemical analysis of juvenile pumice clasts conducted by Briggs *et al.* (1993) showed significant compositional variations in silica content of between 65 and 77%, and widely variable major and trace element compositions indicating the likelihood of compositional zoning and subsequent mixing of magmas prior to and during eruptions. Krippner *et al.* (1998) found the composition of lithics to include fragments of sedimentary, low grade metamorphic basement rocks and emplaced igneous rocks. However, lithic populations from earlier ignimbrites of the Mangakino Caldera were found to be dominated by andesite lavas, suggesting that there was a pre-existing andesite volcano in the Mangakino area. With higher

abundances of Ba, Rb, Zr, and Ti these andesite fragments are geochemically distinct from the nearby andesitic Titiraupenga and Pureora volcanoes.

2.3 Volcanoes of the Western Waikato Region

The many volcanoes found scattered throughout the western Waikato Region are the result of both intraplate- and subduction-related volcanism. Historically, these predominately northwesterly aligned volcanoes in the south and west have been classified by general geographic location and broad lithology and petrography descriptions into the Alexandra and Kiwitahi volcanics respectively. However, detailed geochemical and isotope analysis conducted during the 1980's and early 90's identified four geochemically distinct volcanic groups, known today as the Alexandra Volcanic Group, Okete Volcanic Field, and the Kiwitahi and Maungatautari volcanics (Briggs, 1983, 1986b; Briggs et al., 1989; Cole, 1978) (Figure 2.6).

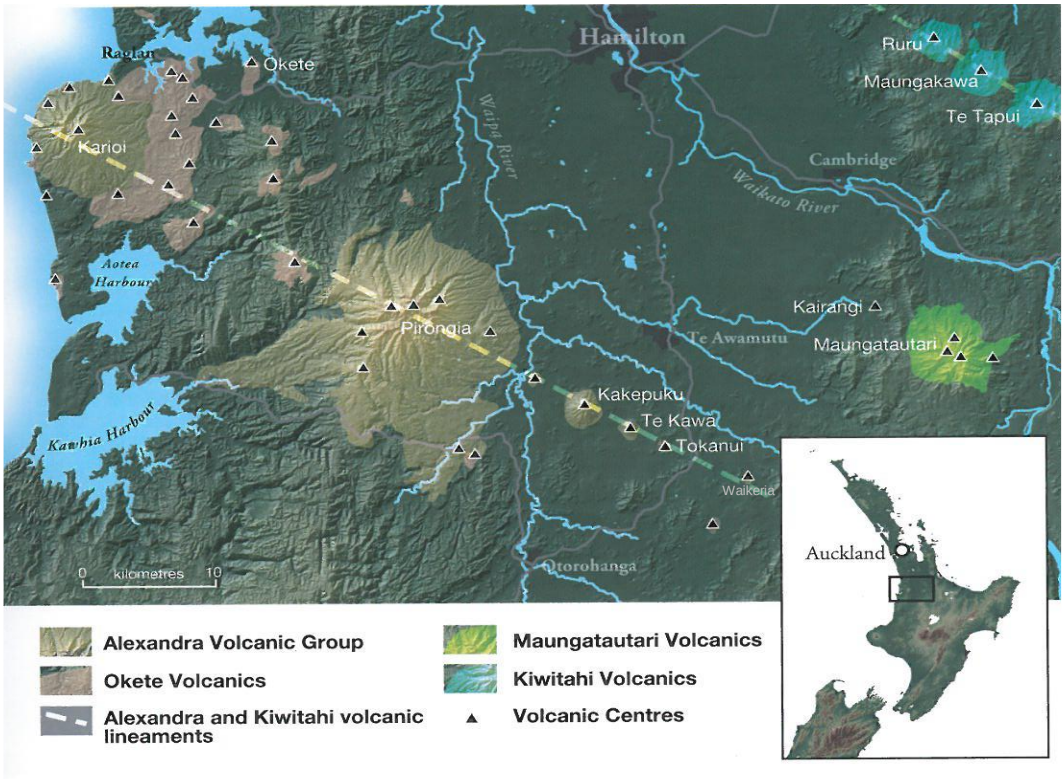

Figure 2.6. Volcanoes of the Waikato Region (Smith & Briggs, 2008).

2.3.1 Alexandra and Okete Volcanic Groups

Initially named by Kear (1964), the Alexandra Volcanics covered an area of 450 km^2 and produced approximately 55 km^3 of volcanic material from a minimum of 40 volcanic centres. Their form ranges from small scoria cones and lava flows to the large low-angled shields with overlying composite cones of Pirongia and Karioi. These two distinct types of landforms, along with differences in distribution, petrography and petrochemistry, led Briggs (1983) to propose a formation called the Okete Volcanic Formation within the Alexandra Volcanics. The Okete Volcanics are concentrated in the region south of Raglan Harbour and consist of numerous small scoria flows, thin lava flows and occasional tuff rings that are alkali in nature. Although their deposits are stratigraphically entwined with those from mounts Pirongia and Karioi, they are enriched in large ion lithophile elements (LILE) and rare Earth elements (REE), have low $^{87}Sr/^{86}Sr$ ratios, typical of intraplate basalts and are therefore geochemically distinct. As such, despite their close spatial association, the Okete Volcanics are now recognised as the southern-most monogenetic field within the Auckland Volcanic Provence (Briggs, 1983; Briggs *et al.*, 1989; Briggs & McDonough, 1990; Smith & Briggs, 2008).

The Alexandra Volcanic Group now consists of the extinct volcanoes of Karioi, Pirongia, Kakepuku, Te Kawa and Tokanui. These volcanoes form a chain 65 km long and have a distinct 300^o northwest alignment which is at right angles to current activity in the TVZ. It has been proposed that this alignment may result from magma rising through a major northwest fracture at deep crustal levels, although this is not consistent with the current tectonic regime and no surface expression is evident (Briggs, 1983; Briggs & McDonough, 1990).

The rocks that comprise the Alexandra Volcanics are predominately basaltic with minor amounts of basaltic-andesite to andesite. The composite cones of mounts Pirongia and Karioi are the largest of the volcanoes within the group, measuring 959 m and 756 m high respectively and consist of andesite cones overlying broader low angled basaltic shield volcanoes. The remaining cones are comprised entirely of basalt (Briggs, 1983; Smith & Briggs, 2008). Unlike their monogenetic

contemporaries, these volcanoes have geochemical signatures typical of subduction-related magmas yet show no evidence of crustal contamination (Briggs & McDonough, 1990). It is thought that each batch of magma was derived from the mantle wedge above the subducting slab in a continental back-arc setting and evolution from basalt to andesite occurred as a result of fractional crystallization (Briggs, 1986a; Briggs & McDonough, 1990).

Briggs *et al.* (1989) used K-Ar whole-rock radiometric dating to determine the ages of 20 volcanic centres within the Alexandra Volcanics and when combined with the limited age data previously available, activity within the field was constrained between 2.74-1.60 Ma. While geomorphic evidence suggested that the volcanoes within the Alexandra Volcanic Group were progressively younger toward the southeast, this study revealed that mounts Karioi, Pirongia, Kakepuku and Te Kawa, instead of younging, are all in fact of broadly similar age. Therefore, assumed ages based solely on geomorphic evidence should be used with caution. Secondly, the overlapping K-Ar radiometric ages and interbedded stratigraphic relations show that these subduction-related magmas formed independently yet contemporaneously with their intraplate counterparts and without any change in the tectonic regime (Briggs & McDonough, 1990).

2.3.2 Kiwitahi Volcanics

The Kiwitahi volcanics includes a group of highly eroded basaltic-andesitic cones, lavas and dikes which form a NNW-striking chain along the western margin of the Hauraki Rift, extending from Waiheke Island in the north to Te Tapui (west of Hamilton) in the south (Figure 2.7).

The individual centres which comprise the Kiwitahi Volcanics, erupted through and onto the Jurassic greywacke basement rocks of the Waipapa terrane and range in age from c. 15 to 5.5 Ma. Overall, these centres generally decrease in age toward the SSE, a pattern which mirrors the development of volcanism within the nearby Coromandel Volcanic Zone (CVZ) (Black *et al.*, 1992; Edbrooke, 2001).

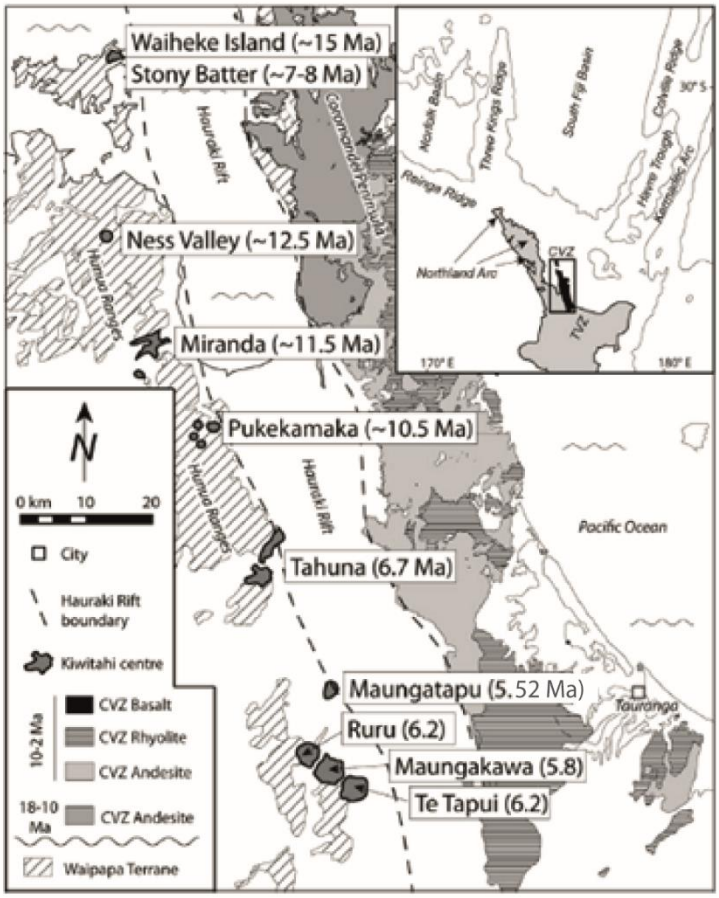

Figure 2.7. Geologic map of the Hauraki Volcanic Region showing the age (in Ma) and location of individual centres comprising the Kiwitahi Volcanics. CVZ: Coromandel Volcanic Zone (Booden et al., 2010).

Within the northern volcanic centres active prior to 6.2 Ma, the erupted rocks consist of plagioclase- and hornblende-dominated andesites. These are comparable to coeval andesites of the CVZ in both age and geochemistry (Booden *et al.*, 2010). The Kiwitahi andesites, however, show a more subdued enrichment in incompatible elements, relatively non-radiogenic Sr isotope compositions and limited crustal contamination. These features, and the small eruption volumes involved, suggests that the Kiwitahi Volcanics formed over the edge of a magmatic system that was centered on the CVZ that was subsequently separated from it by the opening of the Hauraki Rift (Booden *et al.*, 2010).

The four southern centres of Ruru, Te Tapui, Maungakawa and Maungatapu were active between 6.2 and 5.5 Ma and erupted clinopyroxene-dominated, high-

magnesium basaltic andesites with minor plagioclase. Booden *et al.* (2010) confirmed that while these rocks are geochemically distinct from their CVZ contemporaries, they are similar to other Quaternary high-magnesium andesites erupted along the edge of the Taupo Volcanic Zone (Figure 2.8), and thus represent the earliest known high-magnesium andesitic volcanism within the North Island which marks the inception of the current configuration, where high-magnesium andesite eruptions preceded those of regular andesitic volcanism at the leading edge of the arc.

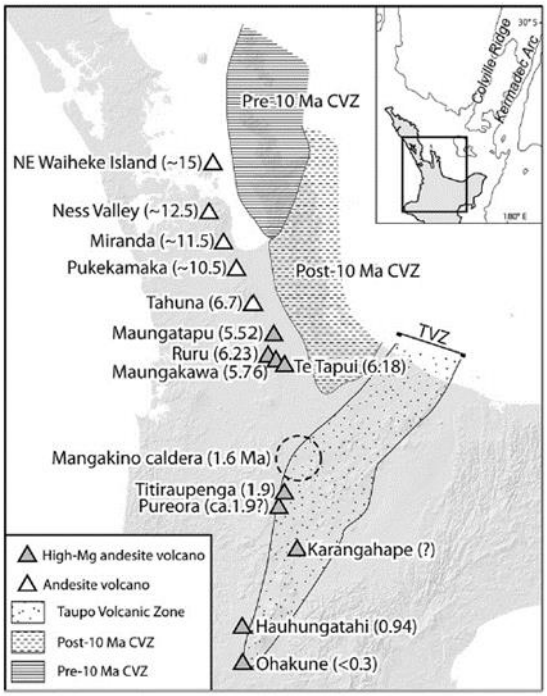

Figure 2.8. The Kiwitahi chain and high-Mg andesite volcanoes in the North Island. Ages in Ma. White triangles: pre-6.7 Ma Kiwitahi centres. Grey triangles: high-Mg andesite volcanoes. CVZ: Coromandel Volcanic Zone; TVZ: Taupo Volcanic Zone (Booden et al., 2010)

2.3.3 Maungatautari

The geology of the Maungatautari area has received little attention from geologists with only brief notes describing the general area prior to the 1950s. In an MSc thesis, Olson (1950) described the mountain as an extinct multi-vent

volcano built of hypersthene-bearing andesite sitting on an ignimbrite plateau (outcropping in the south and east), which abuts a range of greywacke (Pukekura Hills) immediately to its west and surrounded by a ring-plain of lahars. This study appears to be the first to describe the geology of the mountain and its surrounds in detail and focussed particularly on the physical geography and stratigraphy with some petrological descriptions of the different rock types. The age of the mountain was thought to be Late Pliocene with periods of activity during the Pleistocene.

A paleomagnetism and geochronology study completed by Robertson (1983) used standard K-Ar dating techniques to subsequently date the mountain at c. 1.8 ± 0.1 Ma. The grain size fraction tested was split into 4 subsamples to allow for duplicate analyses of both potassium and argon. Although five samples were taken from various points across the mountain, only one age for the mountain has been published. It is unclear which sample site this date reflects, and as the mountain is a large composite cone it would have formed as a result of many eruptions over a considerable period of time. Therefore, this age can only be used as a rough guide as to the period when the mountain was likely to have been active and it still remains uncertain where it fits within the broader volcanic history of the mountain.

This age is, however, broadly similar to the andesitic cones of Titiraupenga and Pureora which lie to the south along the western boarder of the Taupo Volcanic Zone (TVZ) and to later activity within the Alexandra Volcanic group, yet significantly younger than the Kiwitahi Volcanics (Black *et al.*, 1992; Briggs, 1986b) (Figure 2.9). It also predates known rhyolitic activity of the Mangakino caldera which is consistent with the current understanding that now recognises onlapping of the ignimbrites over the lower south and eastern flanks of the mountain (Leonard *et al.*, 2010), in contrast to the stratigraphic order proposed by (Olson, 1950).

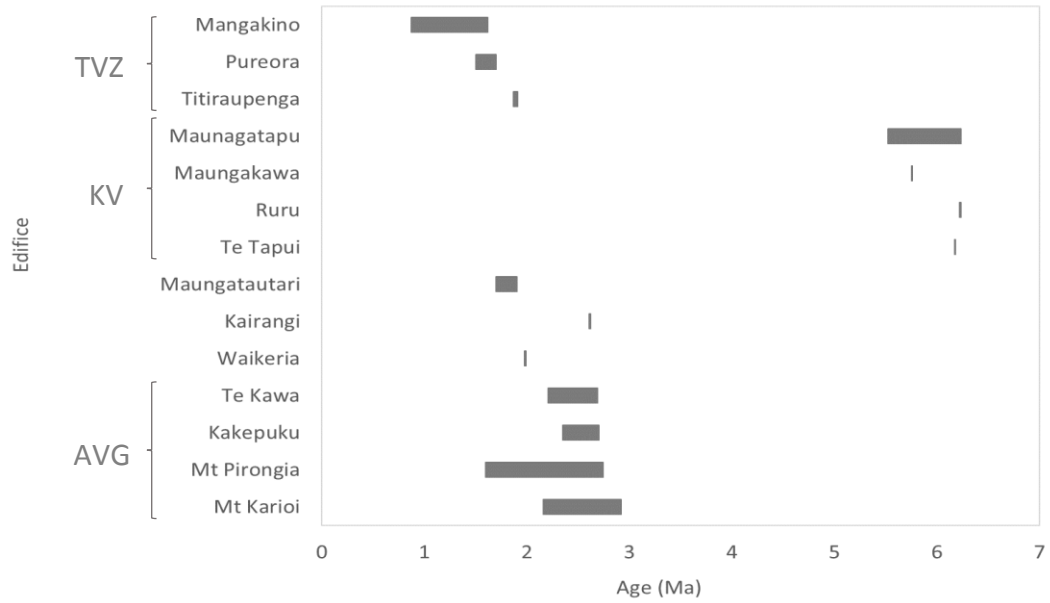

Figure 2.9. Range bar graph showing relative ages of dated volcanoes from the Waikato Region. TVZ: Taupo Volcanic Zone; KV: Kiwitahi Volcanics; AVG: Alexandra Volcanic Group. Age data taken from Black et al. (1992), Briggs et al. (1989); Krippner et al. (1998); Cole and Teoh (1975); Froude and Cole (1985) and Robertson (1983).

Historically, the volcanic complex of Maungatautari has been considered part of the Kiwitahi Volcanics – the chain of basaltic-andesitic cones extending south along the western margins of the Hauraki Gulf from Waiheke Island (Cole, 1978; Kear, 1964). Cole (1978) conducted a study that focused on the distribution, petrography and geochemistry of these volcanoes and included Maungatautari. Petrographically, all lavas were found to be porphyritic with the Kiwitahi Volcanics consisting of low-Si olivine or pyroxene andesite, labradorite-pyroxene andesite and hornblende andesite. The lavas from Maungatautari are mid to high-K, low-Si andesites to dacites and include olivine basalt, labradorite andesite and hornblende andesite which are texturally similar. These lavas were regarded as being derived from the fractionation of labradorite-pyroxene andesite or olivine basalt respectively which suggested different magma source areas. Major and trace element analyses were also found to differ with Maungatautari lavas having higher K_2O, Rb, Zr, V and Sc than their Kiwitahi counterparts, which were in fact comparable to andesites of the Coromandel Volcanic Zone. Based on these distinctions, Cole (1978) excluded Maungatautari from the Kiwitahi Volcanics and suggested that it should instead be considered part of the Alexandra Volcanic

group where lavas were generally more mafic and dominated by olivine basalt – the suggested parent magma for the Maungatautari Volcanics.

Briggs (1986a, 1986b) followed Cole's work with further petrographic and geochemical analyses on Maungatautari lavas, separating them from the Alexandra Volcanic Group. Petrographically, the lavas were again described as porphyritic and often glomeroporphyritic. Phenocrysts included plagioclase, orthopyroxene, clinopyroxene, hornblende, titanomagnetite, ilmenite with rarer olivine and biotite. With the exception of hornblende, groundmass minerals included all phenocrysts with the addition of chlorite and apatite and textures were fine grained with variation between intergranular to intersertal and felted. The mineralogical prefixes used are defined using modal abundances as follows: pyroxene andesites contain total pyroxene > plagioclase, labradorite andesites have modal plagioclase > pyroxene, and hornblende dacites contain significant visible hornblende crystals in hand specimens. Sub-spherical xenoliths containing mineral assemblages similar to the host lavas, were also found to be abundant and ranged in size from a few millimetres to > 10 cm. These inclusions have been interpreted as cognate xenoliths which formed at the bottom and sides of the magma chamber and incorporated as the result of disruption due to magma mixing.

Geochemically, Briggs (1986b) found lavas from Maungatautari to have similar major and trace element contents as Cole (1978). This time, analyses were compared to Titiraupenga and Pureora along the TVZ's western border and andesites from Tongariro. Relative to the TVZ volcanoes, Maungatautari lavas were found to be higher in Rb, Sr, Ba, Zr, Th, La, Ce, P and ratios of Rb/Sr and La/Ya. K/Rb ratios, however were found to be generally lower. The general trends of progressive increases in SiO_2, K_2O and incompatible trace elements while decreasing MgO, total Fe and CaO qualitatively suggest the evolution of magma by fractional crystallisation of a parent magma, combined with magma mixing. However, all attempts at modelling the fractionation of olivine basalt to pyroxene andesite were unsuccessful.

Due to the limited rock exposure across the mountain, most samples have been collected from near the top of the four main peaks of Maungatautari Trig, Hook Nose, Pukeatua and Te Akatarere and the long narrow ridge known as Little Rock (Figure 2.10). Lavas from the symmetrical cone of Oreipunga Hill were found to be exposed in a small cave on the eastern side of the hill while samples of olivine-basalt from the Kairangi scoria cone were collected from boulders scattered across its slopes.

It is now accepted that Maungatautari is an isolated, multi-vent, subduction-related volcanic complex that was active approximately 1.8 Ma. The mountain overlies Jurassic Manaia Hill group rocks of the Waipapa Terrane which consists of well-indurated, massive to poorly bedded, coarse to medium-grained volcaniclastic sandstones and mudstone sequences. The surrounding ignimbrite plateau overlies the lower flanks of the mountain and is comprised of deposits of the Pakaumanu Group, which includes the Rocky Hill and Kidnappers (Raepahu Formation) plus the Ahuroa (Mangaokewa Formation) ignimbrites throughout the east and south, and other mostly welded, undifferentiated ignimbrites found to the west of the mountain. Lahar deposits are concentrated to the north of the mountain and within a thin ribbon surrounding it (Leonard *et al.*, 2010). Many of the lahars originating from the western side of the mountain were diverted north by the Pukekura Hills (Olson, 1950). While the hornblende dacite cone of Orepunga hill is thought to represent a late-stage flank eruption controlled by faulting, this is yet to be confirmed and the relationship of the nearby basalt cone of Kairangi remains uncertain. Therefore, future studies focusing on radiometric dating and the isotopic composition of lavas may help to answer these questions and further our understanding of how the Maungatautari Volcanic Centre fits within the broader context of Late Cenozic volcanic history of the central and western North Island.

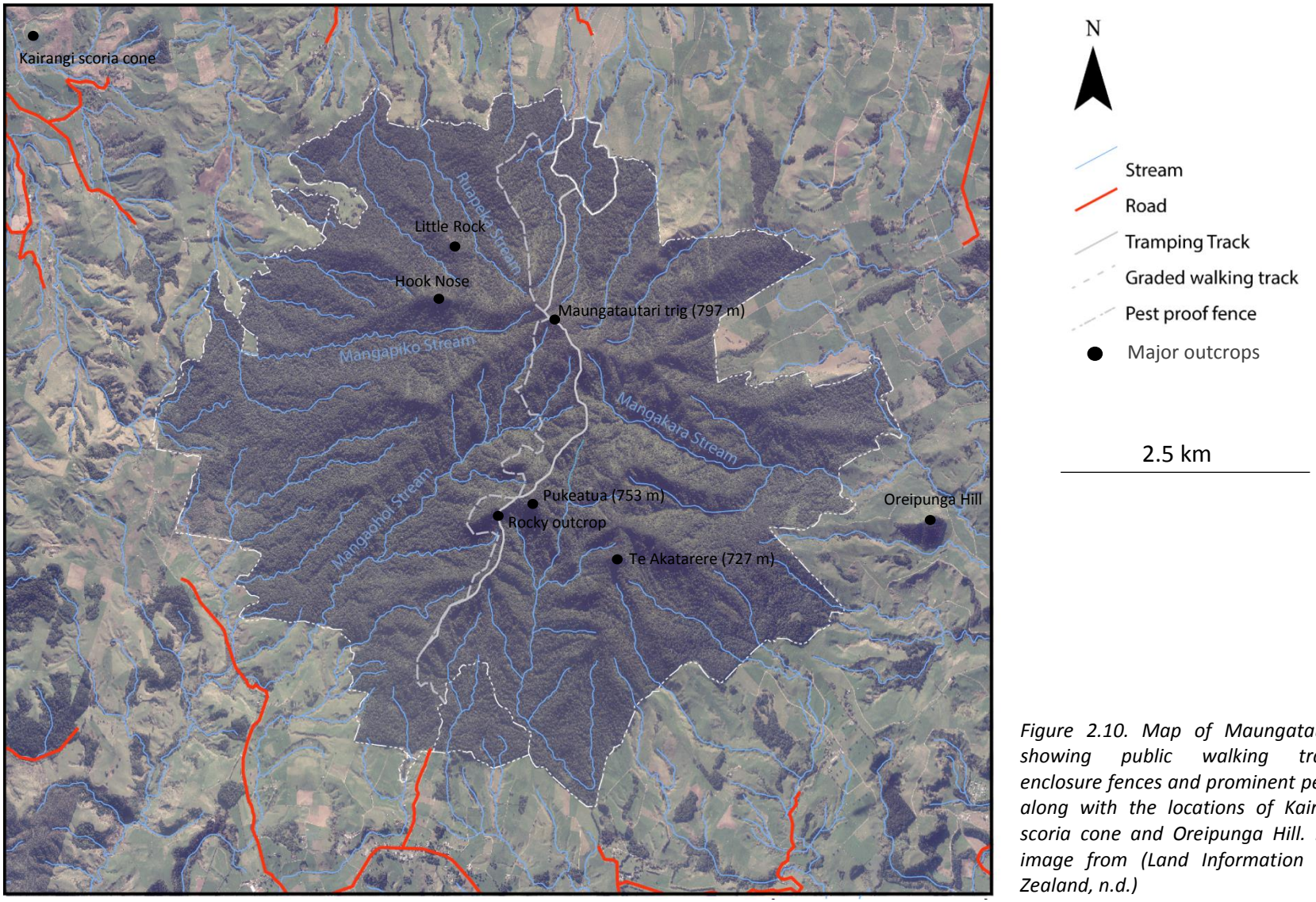

Figure 2.10. Map of Maungatautari showing public walking tracks, enclosure fences and prominent peaks, along with the locations of Kairangi scoria cone and Oreipunga Hill. Base image from (Land Information New Zealand, n.d.)

2.3.4 Undefined volcanoes

Two volcanoes have yet to be officially classified into a particular volcanic group – Waikeria and the basaltic cone of Kairangi.

The small basaltic cone of Kairangi (Figure 2.6) is situated 7 km northwest of Maungatautari (Briggs *et al.*, 1989) and was considered by Cole (1978) to be part of the Maungatautari Volcanics. Subsequent work by Briggs (1986a) points out that its composition is quite distinct from the range of lava compositions found across Maungatautari and is therefore unrelated. However, dated at 2.62 Ma (Briggs *et al.*, 1989), Kairangi is understood to be older than Maungatautari, and as the latter would have formed over a wide time span it is possible that Kairangi represents the inception of volcanic activity within the area.

The volcanic centre at Waikeria (Figure 2.6) has no surface expression and was identified after drill cores revealed dacite at the site of a magnetic anomaly identified during geophysical investigations surrounding Te Kawa (Briggs *et al.*, 1989). This lava complex is situated at the southeastern end of the Alexandra alignment, its geographical location suggests a relationship to the Alexandra Volcanic Group, however its composition is more reflective of dacites found at Maungatautari (Briggs, 1986a).

As no further work on Kairangi and Waikeria has been undertaken, how these centres fit within the complex Late Cenozoic volcanic history of the western North Island currently remains uncertain.

Chapter Three:

Geology and Geomorphology

3.1 Introduction

In contrast to most other landforms, the growth of composite cones is rapid over geological time and involves penecomtemporaneous constructive and destructive processes. As a result, volcanic landforms need to be studied carefully. Formed from a variety of lithological materials, coherent lavas and unconsolidated or poorly welded pyroclastic deposits overlie each other with a complex lateral distribution. This combination of inherently weak rocks and rapid growth, predisposes composite cones to a wide variety of mass-wasting processes.

Catastrophic volcanic mass movements are not as rare as were once considered, having occurred at more than 350 Quaternary volcanoes worldwide, with many showing a complex history of collapse and regrowth (Siebert, 2002; Thouret, 1999). The widespread occurrence of slope failure within a variety of tectonic settings, suggests that it is the dominant catastrophic edifice-modifying process. While slope destabilisation is a long-term process, catastrophic collapse occurs suddenly and results in a voluminous landslide which disaggregates rapidly into a fragmental granular flow. This leaves behind a characteristic horse-shoe shaped, steep-sided break-away scarp and deposits which typically include hummocky terrain with block and matrix facies of largely unsorted and unstratified angular to sub-angular debris (Andrade & van Wyk de Vries, 2010; Siebert, 2002; Thouret, 1999).

Careful study of volcanic geomorphology provides clues to how the landscape has evolved through time, and indirectly provides relative ages of the land's surface over which the erupted material lies and the succession in which it is intercalated. Knowledge of volcanology and the widespread use of new tools such as Global Information Systems (GIS), Digital Elevation Models (DEM) and satellite (along with improved airborne) imagery has expanded over the last 30 years since the geology of Maungatautari was last studied. Field observations and the geomorphic analysis used during this study highlights the complex landscape evolution which has occurred over time.

3.2 Methods

The geomorphology of Maungatautari was examined using a combination of observations made during field work, aerial photographs (SN5945 D1-11, E1-11 and F1-11, Crown Copyright, 1:20,000), 20 m contour topographic data from NZTopo Database, an 8 m resolution digital elevation model (DEM) (Land Information New Zealand, n.d.) and an additional unpublished 5 m DEM from the Waikato Regional Council (n.d.)

ArcGIS™ software was used to derive a hill-shaded DEM of the mountain and surrounding area, illuminated from the northwest at an altitude of 45^{o}. A standard curvature model with stretch shading from blue (gullies) to brown (ridges) was combined with a four-category slope model using a 35% transparency to produce a composite image. Topographic profiles were obtained using 3D analyst tools.

All maps and figures presented here were constructed using ArcMap 10.3 and/or Adobe Illustrator.

3.3 Geomorphology

The geomorphology of the Maungatautari area is a direct result of volcanic, fluvial and mass wasting erosion processes, and the differences in the physical properties of the different rock types. These processes have created a landscape dominated by a combination of ridges, steep-sided yet rounded hillslopes, deep valleys and swampy low-lying flat land.

Roughly circular in shape, Maungatautari measures 6-8 km in diameter at its base. Rising to 797 m above sea level, it is the second highest volcano of the Waikato Region after Mount Pirongia of the Alexandra Volcanic Group. The extensive cover of native forest vegetation results in poor outcrop exposure, with the majority being found around the main peaks, along the sides of very steep gullies and in cuttings along the length of publicly accessible walking tracks. Thus, visually

identifying the stratigraphic relationship between exposed lava flows and pyroclastic deposits is limited.

A hillshade DEM of Maungatautari is presented in Figure 3.1, along with a 3D curvature and slope map in Figure 3.2. The mountain displays extreme relief which is highlighted in Figure 3.2 and typified by sharply convex ridgelines with steep (>25^{o}) slopes in the upper portions of the mountain grading to more rounded, moderate to gentle (6-25^{o}) slopes. The flanks are dissected by deeply incised gullies, with those of the Ruapeka and Mangapiko streams on the north-western and Mangaohoi and Mangakara streams southern slopes (Figure 2.10) being especially broad at ~800-1000 m wide, and well developed. Just below the summit these gullies curve and merge with the upper reaches of each other, to form distinct horseshoe patterns (Figure 3.1). The prominent, well known peaks of Hook Nose and Little Rock (Figure 3.1) are located along the fringe of one of these gullies.

The volcanic vents of Kairangi, Oreipunga and an inferred eroded summit vent centred near Maungatautari Trig display a distinct northwest alignment (Figure 3.1), a trend well recognised in the nearby Alexandra and Kiwitahi volcanic groups.

Outside the perimeter fence of the ecological reserve, the rounded lower flanks of the volcano are covered in pasture yet still descend steeply into stream channels (Figure 3.4). Andesite boulders are regularly found protruding from these slopes and littering the valley floors. One exception to this is found in the north-eastern corner of the mountain, where a horse-shoe shaped, steep-sided break-away scarp surrounds an area of predominately flat, poor-draining land dotted with large hummocks. These features are characteristic of a voluminous rock avalanche event resulting from sudden and catastrophic sector collapse.

Surrounding the mountain, ignimbrites originating from Mangakino Caldera to the south-east onlap the lowest slopes of the mountain, occasionally outcropping prominently to form steep bluffs as in the south-eastern corner of

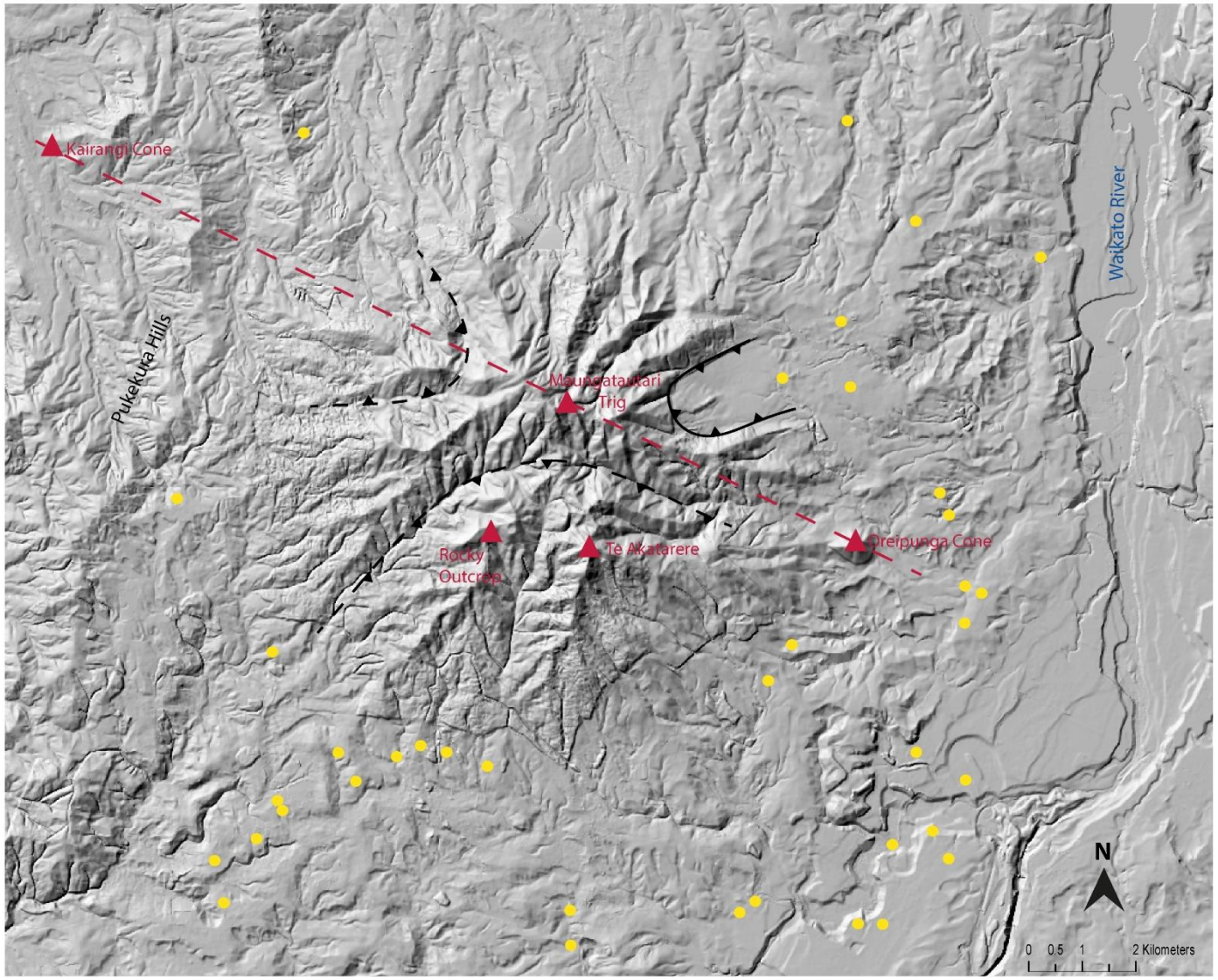

Figure 3.1. Hillshade DEM of the Rotoorangi, Pukeatua and Maungatautari area. The eroded composite cone of Maungatautari is clear in the centre of the image and is bounded on the east and west by the Waikato River and Pukekura Hills respectively. The horseshoe shaped excavation in the northeast is highlighted along with prominent gullies of interest. The northwest alignment (dashed line) of major volcanic vents (triangles) is also shown. Yellow dots are locations of water bore holes from Waikato Regional Council (n.d.).

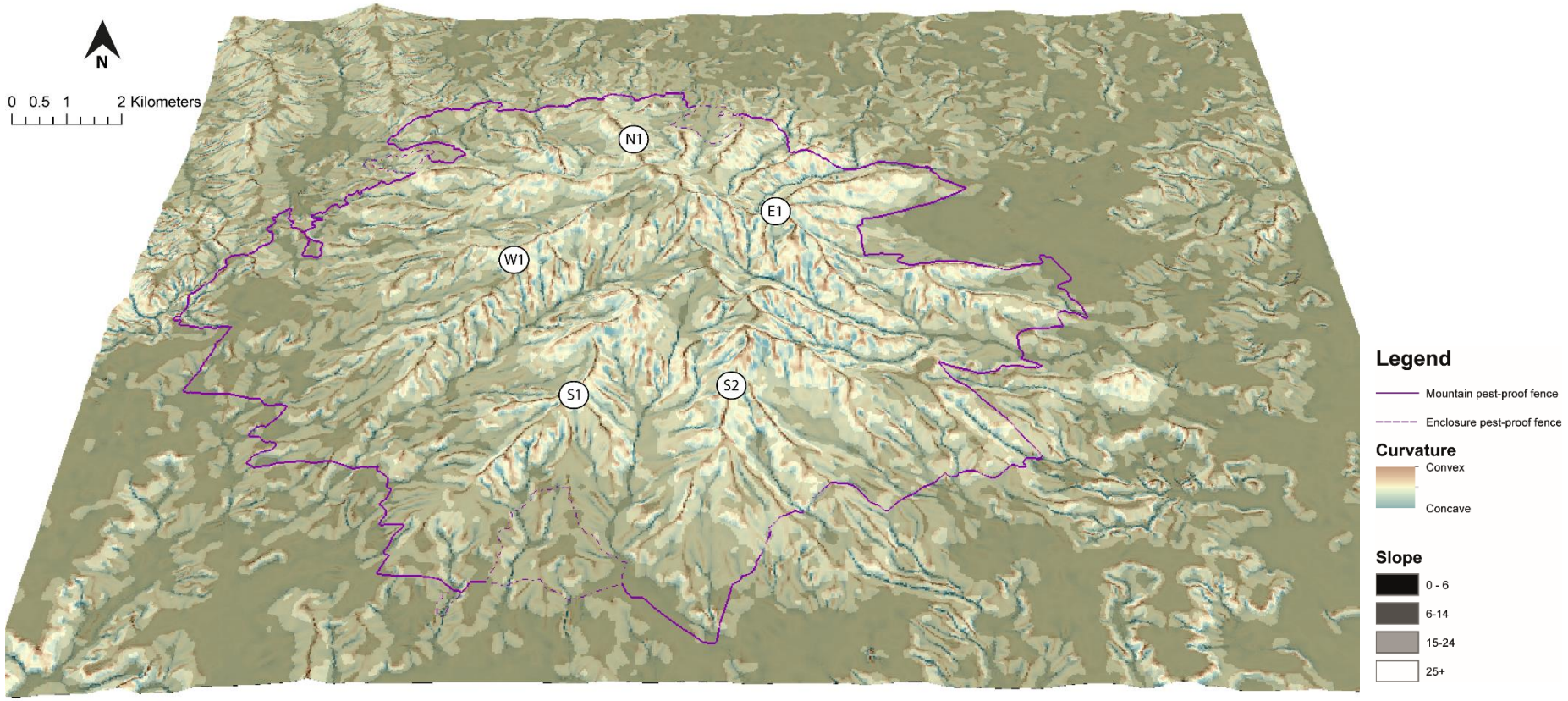

Figure 3.2. 3D image of Maungatautari showing curvature overlying slope. Ridge lines are shown in brown and gullies and streams in blue with the sharpness of lines reflecting the intensity of concavity or convexity. Slope is reflected from light to dark representing high to low angled slopes respectively. The relatively flat area to the north and south of the mountain is a thick (>100 m) and extensive plateau comprised of Pakaumanu Group ignimbrites originating from the Mangakino Caldera. Major ridgelines (S1, S2, E1, W1, N1) referred to in the text are labelled.

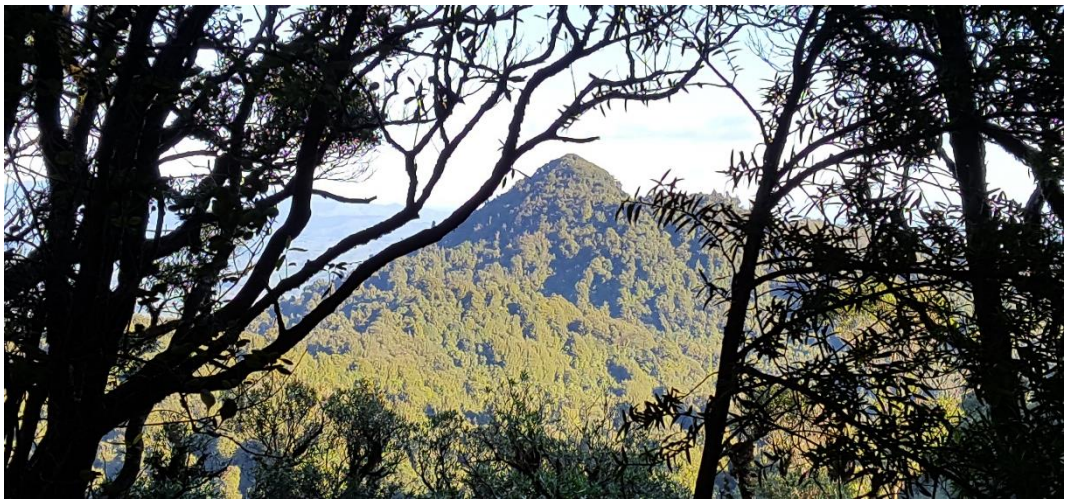

Figure 3.3. View of Te Akatarere peak, facing south, from a track along the main eastern ridgeline to Maungatautari Trig.

Figure 3.4 Mangaohoi Stream emerging from native forest to cut through farmland on the lower south-western slopes of Maungatautari.

the field area (Figure 3.5). River terraces created during the entrenching of the Waikato River are found to the east and valleys here are infilled by alluvium (Figure 3.5).

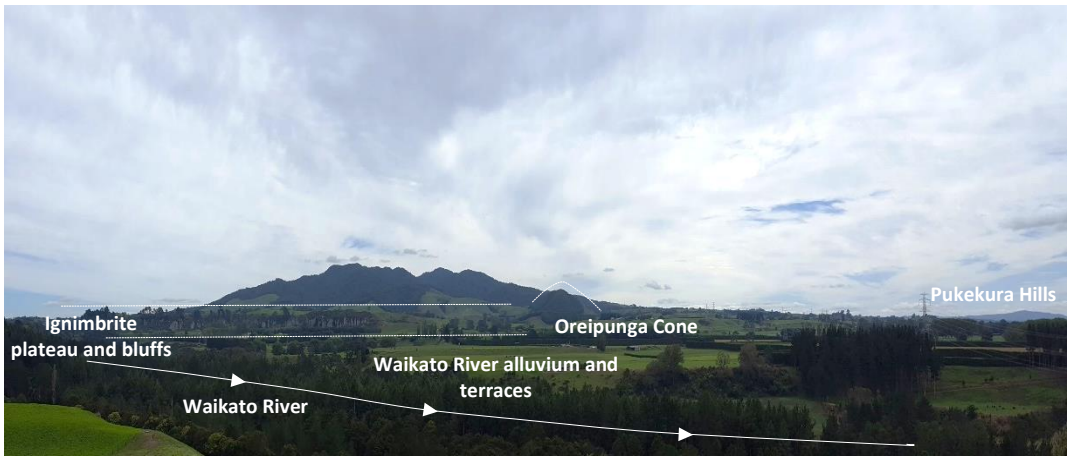

Figure 3.5 Maungatautari as viewed towards the northwest from Arapuni. Large bluffs comprising of ignimbrite from Mangakino Caldera surround the lower slopes of the mountain to the south (left). The dacite cone of Oreipunga is visible in the centre of this picture. The foreground shows the path (in trees) and terraces of the Waikato River, while in the far-right background is the outline of a northern section of the basement range – Pukekura Hills.

3.4 Geological map and cross section

A geological map of the Maungatautari field area (Figure 3.6) was compiled as part of the larger study focusing on the volcanic evolution of the mountain using a combination of field observations and interpretation of topographic contour data along with published QMAP data.

A geological cross section is shown in Figure 3.7.

Eight different stratigraphic units are found to occur within the field area, and their distribution is shown in Figure 3.6. Maungatautari overlies Jurassic Manaia Hill group rocks of the Waipapa Terrane and abuts a range of the same rocks known as the Pukekura Hills (Olson, 1950) immediately to the west. Much of the cone remains undifferentiated, however where possible, the lavas have been classified into either andesite or dacite based on their SiO_2 content and mineralogical prefixes were assigned according to modal composition following Cole (1978) and Briggs (1986b). The hornblende dacite cone of Oreipunga (352 m) is situated on top of the lower flanks of the eastern margin of the Maungatautari edifice.

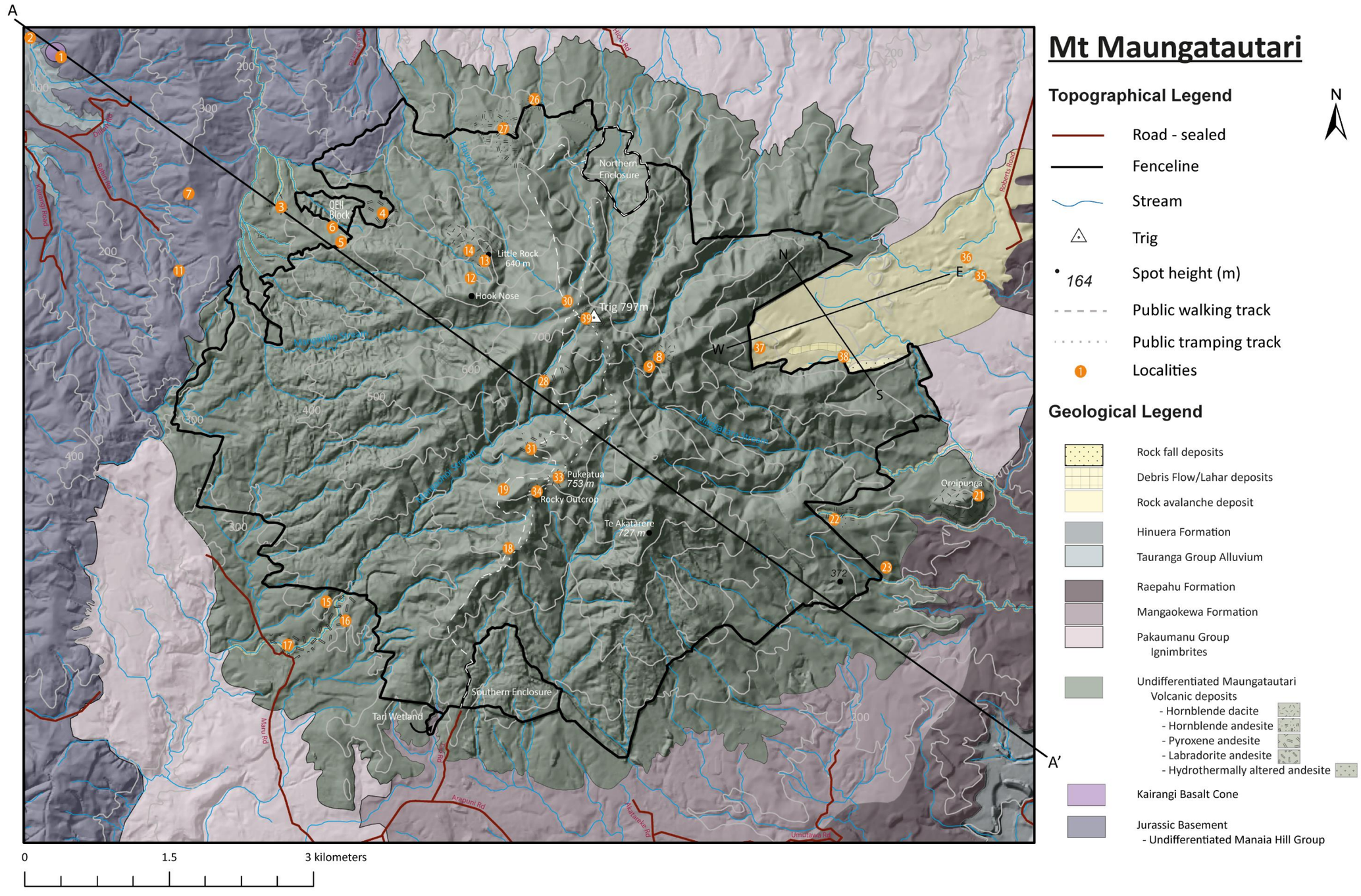

Figure 3.6. Geological map for Mt Maungatautari and its surrounds.

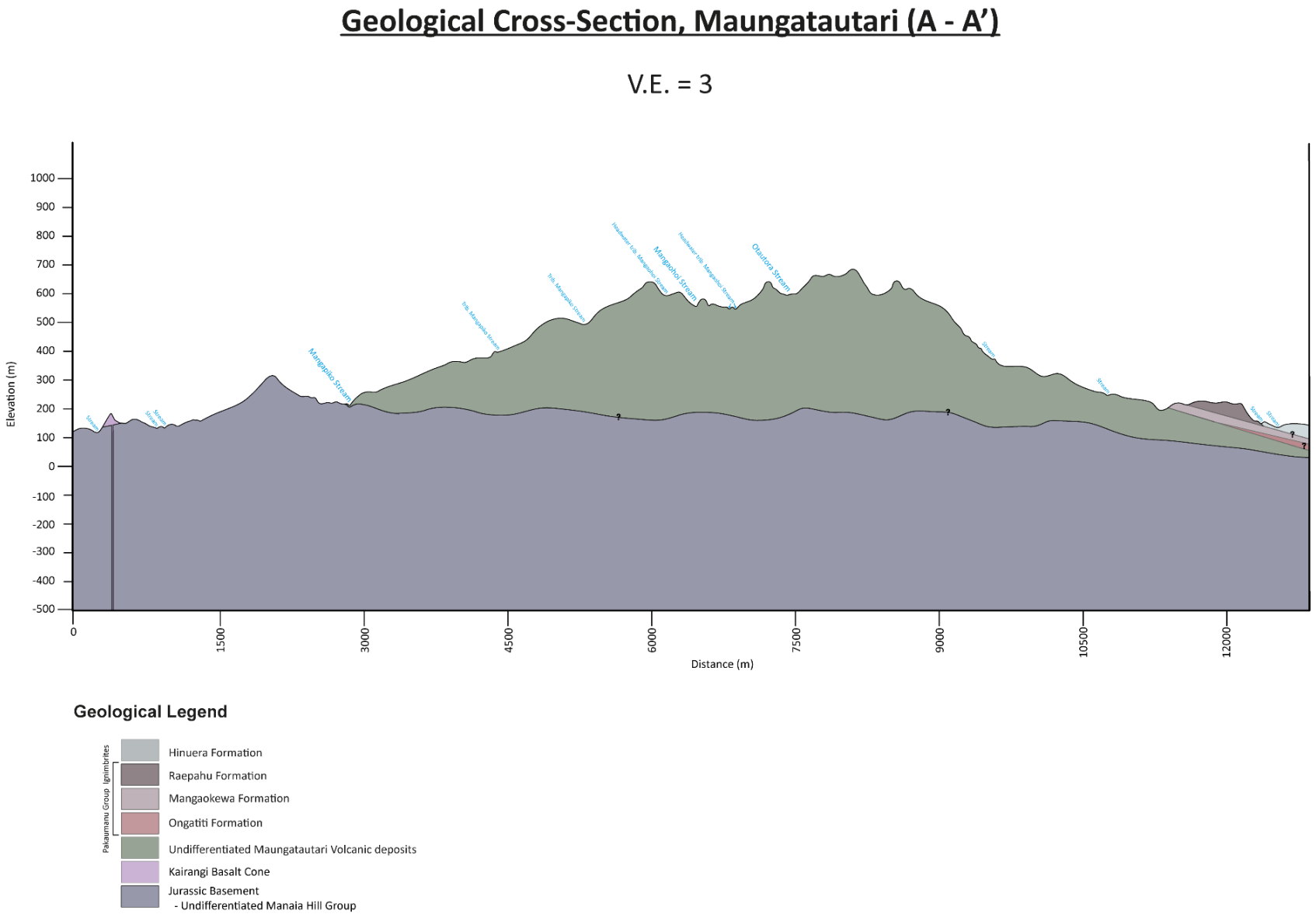

Figure 3.7. *Geological cross section A-A' as shown in Figure 3.6.*

The small Kairangi basalt cone occurs amongst the Pukekura Hills (Figure 3.7) in the north-eastern corner of the field area, approximately 750 m north of the junction of Rahiri and Dillon Roads (Figure 3.6). Surrounding Maungatautari to the north, east and south is a thick (>100 m) ignimbrite plateau which overlies the lower flanks of the mountain (Figure 3.7) and is comprised of deposits of the Pakaumanu Group, which includes the Rocky Hill and Kidnappers (Raepahu Formation) and the Ahuroa (Mangaokewa Formation) ignimbrites. The differentiation and distribution of these units did not fall within the scope of this project, and as such are strongly based on data published by the Institute of Geological and Nuclear Sciences, New Zealand (GNS Science) as part of the QMAP series (Leonard *et al.*, 2010). In the north, the extended ring plain of lahar deposits mapped originally by Healy *et al.* (1964) and included in Leonard *et al.* (2010), has been replaced in Figure 3.6 with undifferentiated Pakaumanu Group Ignimbrites. This variation from previous geological maps reflects field evidence of lahar deposits being highly channelised within the stream valleys and often below the uppermost surface level. Stratigraphic logs of water bores from Waikato Regional Council (n.d.) (Figure 3.1) also supports the reduced surface distribution of ring plain deposits, with an overwhelming dominance of units described in drill logs as either ignimbrites or 'rhyolites', the latter interpreted here as ignimbrites. The lack of other lithologies, with conspicuous absences of any andesitic boulders/gravels, supports the observation that older lahar and more recent debris flows are very localised and do not form an extensive exposed ring plain surrounding the mountain. Basement rock is also rarely reached in bore holes, except for those that were drilled along the eastern margin of the Pukekura Hills.

In the northeast corner of the volcano, early Tauranga Group alluvial deposits of Leonard *et al.* (2010) have been replaced with a rock avalanche deposit. This newly identified unit extends north-eastwards towards Roberts Road from an amphitheatre-shaped scarp and is characterised by a hummocky terrain of large, boulder-filled mounds at the foot of the scarp, just past the modern-day enclosure boundary fence.

Valley infill consisting of Early Tauranga Group and Holocene Hinuera Formation alluvium are found in the northwest and southeast respectively consistent with the published QMAP (Leonard *et al.*, 2010).

3.5 Description and stratigraphic relationship of geological units

3.5.1 Jurassic Basement

Basement rocks within the Maungatautari field area belong to the Late Jurassic Manaia Hill Group of the Waipapa Terrane and unconformably underlie Maungatautari andesitic rocks and the Ongatiti Formation west of Arapuni (Olissoff, 1981).

Deposited during the Late Jurassic Period (~147-164.3 Ma) along the eastern Gondwana margin, these rocks are dominated by well-indurated, massive or poorly bedded, volcaniclastic sandstone, with minor interbedded mudstone (Leonard *et al.*, 2010). Conglomerates also form part of Manaia Hill Group rocks, but were not observed during this study. Outcrops are found within quarries and streams throughout the rolling Pukekura Hills.

Occasionally hills are conical-shaped, with steep sides and large boulders outcropping along various slopes. These hills consist of grey-green compositionally immature, volcaniclastic sandstone with angular, dark grey mudstone clasts, mostly 2-3 mm in diameter (Figure 3.8).

Collectively, these sandstones and chipwackes are known locally as greywacke which is commonly highly fractured, and quartz and/or zeolite veins are also present. Weathering changes the colour of these rocks to a distinctive yellow-orange colour.

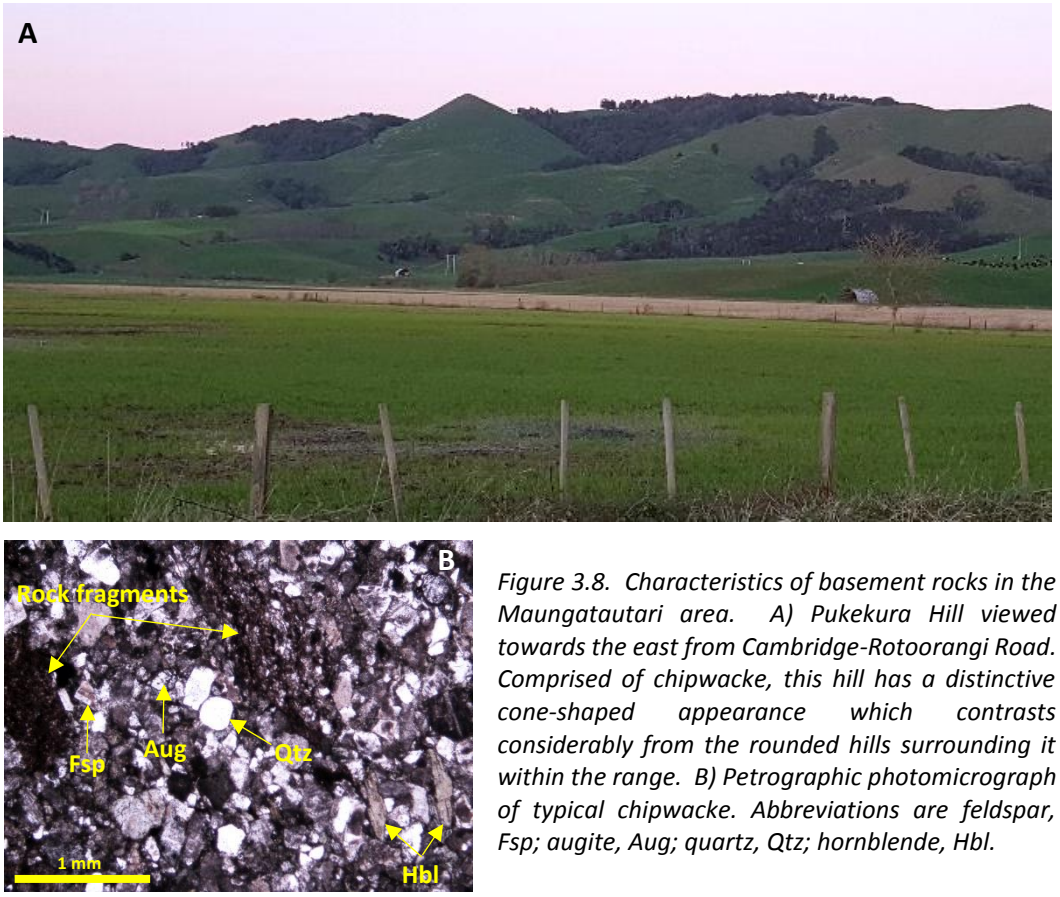

Figure 3.8. Characteristics of basement rocks in the Maungatautari area. A) Pukekura Hill viewed towards the east from Cambridge-Rotoorangi Road. Comprised of chipwacke, this hill has a distinctive cone-shaped appearance which contrasts considerably from the rounded hills surrounding it within the range. B) Petrographic photomicrograph of typical chipwacke. Abbreviations are feldspar, Fsp; augite, Aug; quartz, Qtz; hornblende, Hbl.

3.5.2 Kairangi Scoria Cone

The small basalt cone at Kairangi is located on top of the lower flanks of the Pukekura Hills (Figure 3.9). Named the Hewson Formation (Leonard *et al.*, 2010), it comprises dense, porphyritic basalt with phenocrysts of olivine and rarer pyroxene and common mantle xenoliths.

Less than 80 m high with steep ~30^{o} slopes, geomorphically this cone resembles the scoria cones of the nearby Okete volcanic field, although no scoria has been observed. Dated at 2.62 Ma (Briggs *et al.*, 1989), the age of this volcano suggests that any surface scoria would likely to have been eroded and small, more resistant lava flows preserve the well-developed cone.

Samples of unweathered basalt can be obtained from a field of large boulders which can be traced from the summit down into the gully on the northern side of the cone and has been interpreted to be the remains of a lava flow (Figure 3.10).

Figure 3.9. Kairangi scoria cone (inside circle) as viewed from Kairangi Hill, 1.5km to the south-west.

Figure 3.10. Large boulders showing the path of an eroded lava flow down the northern flank of the Kairangi scoria cone.

3.5.3 Maungatautari Volcanic Deposits

Volcanic deposits from Maungatautari are varied and in this study, were found to occur as lavas, dikes, volcanic breccias, and lapilli tuffs. Rock exposures within the enclosure are mostly limited to the main peaks and small quarries made during the construction of the over-the-mountain public walking track (Figure 3.6).

Predominantly, lavas show pervasive blocky or platy jointing (Figure 3.11), and are comprised of dark grey, porphyritic, feldspar-rich, non-vesicular andesite or dacite with varying amounts of both pyroxene and hornblende along with mantle and crustal xenoliths. Joint spacings range from a few centimetres to up to 15 cm and in exposures at Little Rock (Figure 3.11-A) and Pukeatua Peak, the platy-jointed lavas have layers which taper and pinch out while others are continuous across the face of the outcrop. Joints observed in the small cave on the eastern slopes of Oreipunga Cone (Figure 3.11-B) show similar thickness but are more continuous.

On the lower slopes, two eroded lava flows have been found extending from the tree-line into farmland. The first, is aligned with a bearing of 110^{o} and located in the north-western corner of the mountain exposed along the western slope of a small depression, east of the QE2 block (locality 4, Figure 3.6). It is characterised by rounded boulders ranging in diameter from ~25 cm to 2-3 m (Figure 3.12), and composed of non-vesicular, dark grey porphyritic andesite. The second lava flow was found on a farm between Hicks and Luck at Last roads on the lower flanks of the main northern ridgeline of the volcano (locality 27, Figure 3.6). These boulders ranged in size from approximately 0.5 to 3 m, and were also composed of non-vesicular, porphyritic dark grey andesite. Boulders here are found scattered across

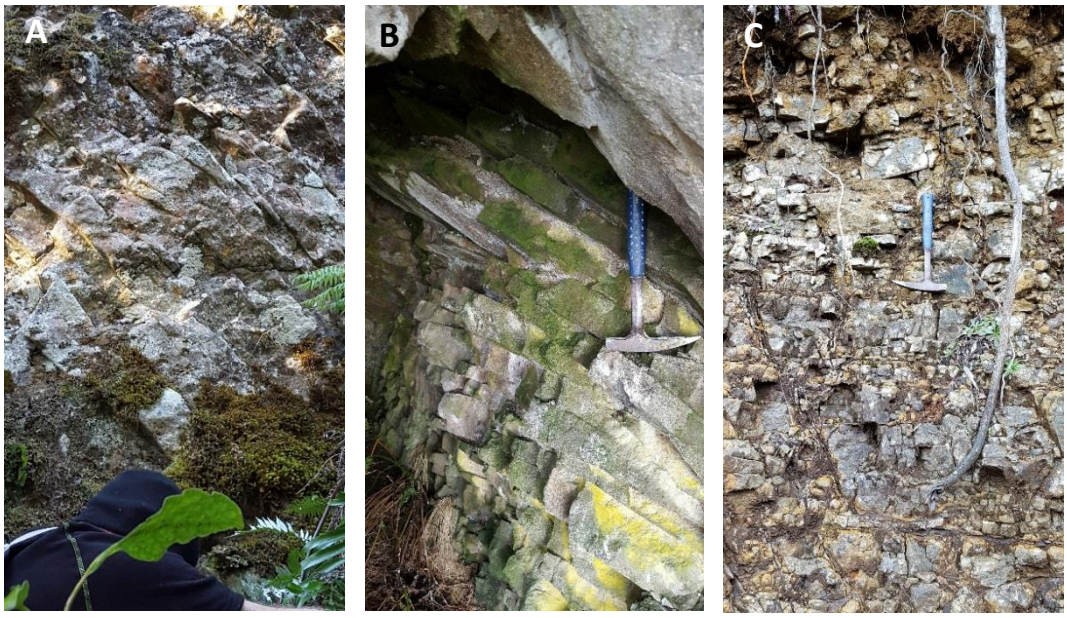

Figure 3.11. Examples of platy-jointed lavas at A) Little Rock Peak and B) Oreipunga Cone. C) Blocky jointing at Quarry 58.

Figure 3.12. Rounded and elongated boulders of an eroded lava flow on the lower north-western slopes.

the width of the ridge and descend to the treeline of an area of privately owned native bush (Figure 3.13), but are not observed on either the western or eastern slopes. Two to three clusters of rocks were observed, where rocks had been moved to accommodate the construction of the perimeter fence. Large boulders can also be traced from this location uphill through bush to the main public walking track where they can be found lying next to the track en route to the summit. The boulders are thought to have been uncovered and pushed to the side during relatively recent track construction.

Figure 3.13. Rounded boulders of an eroded lava flow on the lower northern slopes. Rock clusters are where rocks had been moved to accommodate the construction of the perimeter fence.

Located in the northwest corner of the mountain (Figure 3.6), Little Rock forms a conspicuous ridge 190 m long by 2-4 m wide which dips to the northwest where it grades into the general slope of the mountain. This prominent peak along with Hook Nose, and two undefined outcrops on the main northern tramping track and south of Te Akatarere, have previously been described as late-stage radial dykes (Briggs, 1986b; Olson, 1950). In addition to these, one more was located just south of Pukeatua Peak along the main mountain tramping track. This exposure of massive hornblende dacite is known as Rocky Outcrop and is orientated at 084^{o}.

A localised area of hydrothermally-altered andesite was found in the headwaters of the Mangakara Stream in a pit which was excavated in the late 19th or early 20th century during gold prospecting on the mountain (Figure 3.14). Hydrothermal fluids flowing through the host andesite has created zones with variable degrees of alteration. The most intense zones consist of bleached angular andesite fragments with preserved relict texture and small (~1cm) red-brown veins which give the rock its overall orangey colour.

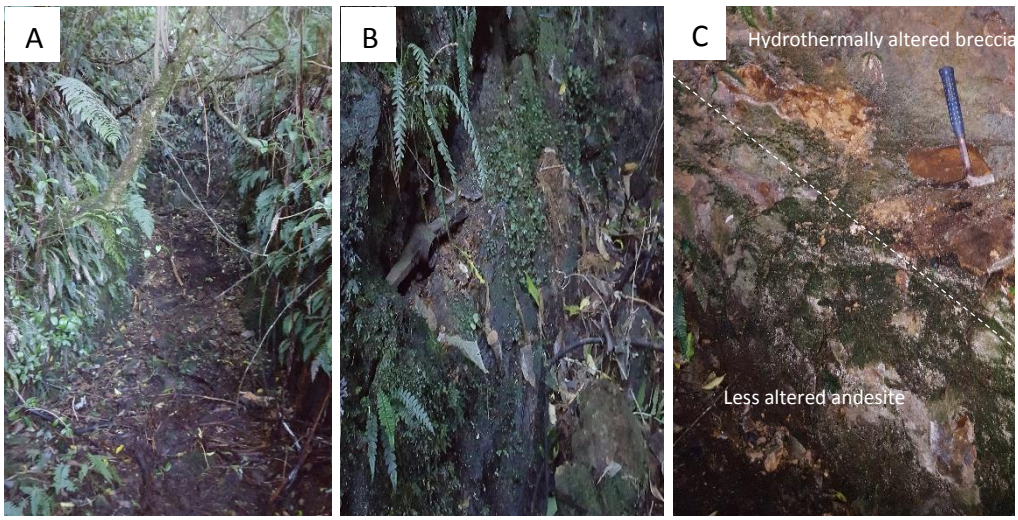

Figure 3.14. Small pit style gold working in the headwaters of the Mangakara Stream. A) Open box cutting. B) Tip of pick axe left behind after gold exploration ceased. C) Zone of intense hydrothermally altered breccia above less altered andesite below.

In the south, track construction has uncovered the first pyroclastic sequence to be observed at Maungatautari, which consists of an 8 m section of massive, non or normally graded, very coarse lapilli tuff with regular angular blocks, crystal and lithic rich coarse tuff and fine lapilli laminations, and coarse tuff, overlain by reworked colluvium and in situ soil.

3.5.4 Pakaumanu Group Ignimbrites

Ignimbrites of the Pakaumanu Group originate from the Mangakino caldera form an extensive plateau which surrounds Maungatautari on three sides. This plateau has been eroded by streams to create valleys in which exposures of various ignimbrites can be found. During this study, Rocky Hill Ignimbrite was located in one such valley northeast of Oreipunga Cone (Figure 3.15). It was sampled from a small bluff ~10 m high which formed the valley wall. Numerous other outliers are also found throughout the valley. This ignimbrite is the youngest unit of the Raepahu Formation and consists of a creamy grey, poorly to non-welded, crystal rich, lithic poor, pumiceous ignimbrite. This unit extends along the eastern margin of Maungatautari and is known to form the 30 m high bluffs on the south-eastern corner behind Pohara Pa (Olissoff, 1981) (Figure 3.5).

Figure 3.15. Bluffs of Rocky Hill ignimbrite outcropping around the edge of a valley east of Maungatautari. The tree covered southern side of the dacite cone of Oreipunga can be seen in the background between the main andesitic mountain and the bluffs.

While no contact between the Rocky Hill Ignimbrite and Maungatautari andesite was found, andesitic lava was observed in a track cutting south Oreipunga cone at an elevation of 260 m and no ignimbrite was located up slope from this location.

Bluffs of undifferentiated ignimbrite were also observed within the valley between Maungatautari and the Pukekura Hills in the southwest corner of the field area west of Maru Road. The bluffs are the result of erosion of the plateau surface by the Mangaohoi Stream whose headwaters are located near the summit of Maungatautari. Together with its numerous tributaries, this stream system is the major drainage pathway for the entire south-western corner of the mountain. East of Maru Road, no ignimbrite was located between the road and the enclosure fence within Mangaohoi stream valley.

3.5.5 Alluvium

Alluvial deposits comprise the youngest geological units within the field area. The valleys to the west of the Pukekura Hills are infilled with Early Quaternary Tauranga Group. In the southeast and east valleys are filled with ignimbrites until east of Oreipunga Road where terraces formed due to the redirection and subsequent entrenchment of the Waikato River c. 17000 years ago (Leonard *et al.*, 2010).

These units have not been investigated as part of this study and have been mapped in accordance with the published QMAP by Leonard *et al.* (2010).

3.5.6 Mass wasting deposits

Deposits of rock falls and slides, debris flows and rock avalanches have all been observed at Maungatautari.

Rock avalanche deposit

On the north-eastern flank of Maungatautari (Figure 3.1) there is a horse-shoe-shaped, steep-sided break-away scarp surrounding an area of predominately flat, poor-draining land. At the eastern end of the scarp, large hummocks aligned perpendicular to the direction of flow (Figure 3.16A) mark the beginning of a depositional area approximately 1.6 km^2, which extends to the northeast where hummocks are found to be numerous (Figure 3.6). East of Roberts Road their presence becomes obscured as a result of fluvial processes during the formation of the present Waikato River channel. The northern and southern deposit boundaries mirror the scarp of the mountain. As such, the volume of the original rock avalanche deposit has been determined using cross-sectional GIS topographical profiles of the best-preserved feature – the scarp, and is estimated to be 0.28 km^3.

The interior of an in situ hummock was examined next to a farm race which led to a small creek crossing where its eastern edge had been exposed (Figure 3.17). Internally it consisted of mid-sized, non-sorted, angular to sub-angular blocks of porphyritic andesite within a finer grained matrix of similar lithology. A general increase in block size was observed towards the centre of the hummock which was more poorly exposed. The hummock was covered by 0.5 m of a red-orange, well-developed soil overlain by ~15 cm of dark brown organic rich soil.

Large angular to sub-angular blocks up to 2 m wide by 3-4 m long were arranged neatly in the centre of the dairy farm's access loop road (Figure 3.18); which were extracted from a nearby hummock by the farmer to create a flat platform for the construction of a milking shed. Most blocks consisted of dense, feldspar-rich porphyritic andesite with coarse jointing. Some contained abundant, sub-spherical < 10 cm-sized clasts of hornblende-rich, yellow xenoliths, interpreted by Briggs (1986b) to be cognate xenoliths which became incorporated into the lavas as a result of disruption of the cumulate layers at the bottom and sides of the magma chamber. A few smaller blocks, however, were found to be composed of chipwacke (Figure 3.18B).

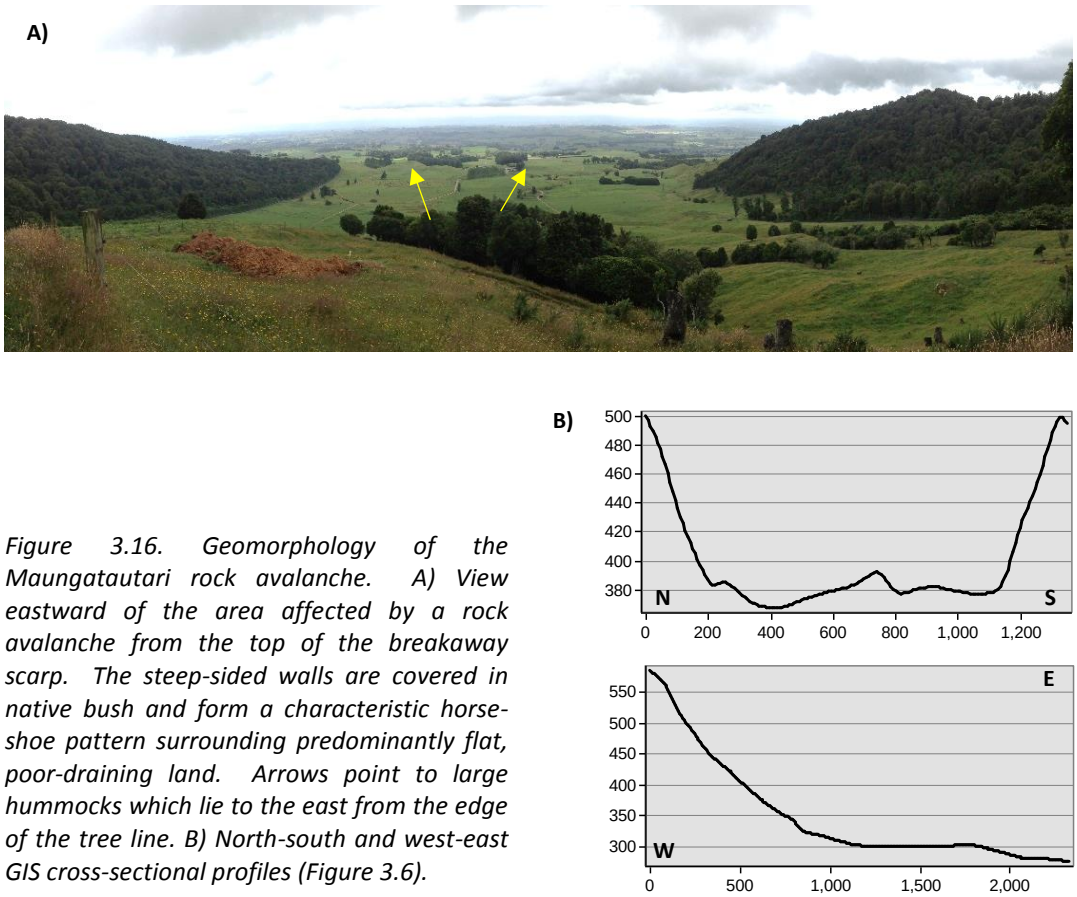

Figure 3.16. Geomorphology of the Maungatautari rock avalanche. A) View eastward of the area affected by a rock avalanche from the top of the breakaway scarp. The steep-sided walls are covered in native bush and form a characteristic horse-shoe pattern surrounding predominantly flat, poor-draining land. Arrows point to large hummocks which lie to the east from the edge of the tree line. B) North-south and west-east GIS cross-sectional profiles (Figure 3.6).

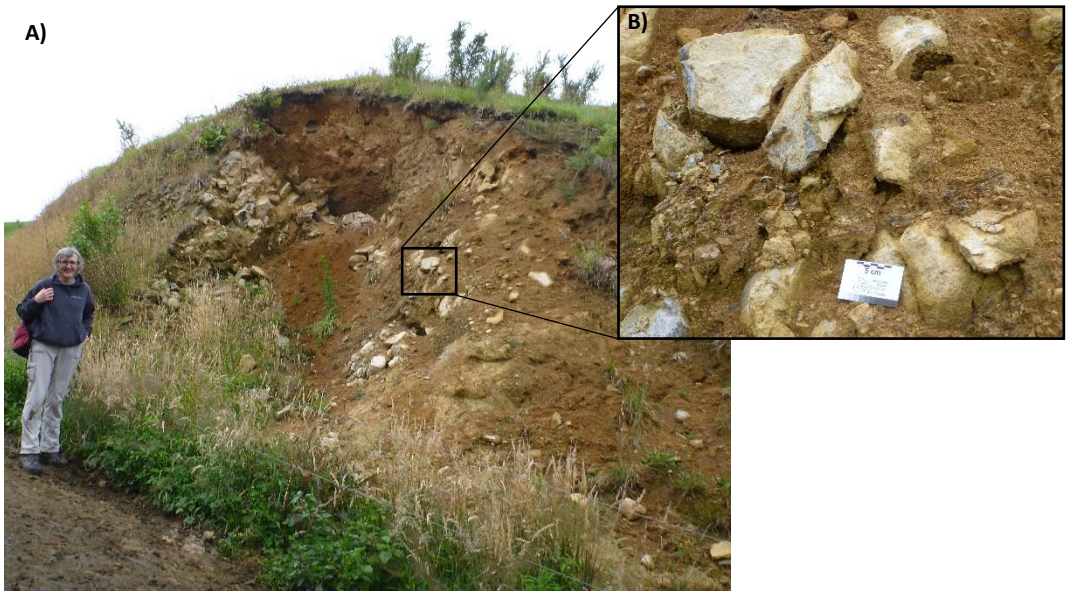

Figure 3.17. Rock avalanche deposit texture. A) Large proximal hummock consisting of mid-sized, unsorted and unstratified angular to sub-angular blocks and matrix mantled by post-collapse tephra deposits. B) Close up of block and matrix facies.

The head of the collapse scarp is obscured by a steep talus slope comprised of debris which accumulated within the rock avalanche source area when material failed to be incorporated into the main flow, and extends approximately 700 m into the centre of the excavated area (Figure 3.16). An exposure 3 m wide by 1.9 m deep into this surface was located near the highest point in the middle of the scarp and lacked a typical well-established soil profile. Instead, dark brown/black silty clay graded downwards into medium brown clayey silt, which then overlay 1.6 m of yellow clay yellow clay with relict weathered andesite clasts and sporadic plant fragments. In the upper zone of this section clasts were contained within a reddish brown clayey silt matrix. These features are consistent with a talus slope comprised of highly weathered mass-wasting deposits.

Figure 3.18. A) Large mostly andesite angular-subangular blocks in an artificial pile retained from the centre of a hummock that had been removed by the landowner. B) Smaller boulders of chipwacke surrounded by andesite blocks

Debris flow deposits

Debris flows is the type of flow which occurs when sediment concentrations reach a level where the flow exhibits significant yield strength. This yield strength enables the flow to support large clasts, inhibits sorting and the development of bedding or other sedimentary structures and causes the flow to stop suddenly (Selby, 1993). Within an active volcanic environment, this type of flow is known as a lahar. At Maungatautari the deposits of many such flows were observed, but as the timing of these events remains uncertain, the generic term of debris flow will be used.

The deposits of debris flows originating from Maungatautari have been discussed in previous studies (Briggs, 1986b; Cole, 1978; Olissoff, 1981; Olson, 1950) and on the lower mountain slopes form channelised deposits which underlie and overlie ignimbrites of the Pakaumanu Group (Olissoff, 1981).

Within the rock avalanche scarp, small debris flow deposits were found at the base of the southern wall near the enclosure fence and were distinguished by their distinctive lobate fronts and appear to originate from a small gully within the tree line (Figure 3.19). One lobe is noticeably smaller than the other and may represent either separate pulses of a single flow or two individual events. A larger lobe could be traced from its lobate front (Figure 3.19B) back up the talus slope, originating from somewhere near the head of the scarp. Therefore, the upper portion of the talus slope (Figure 3.16) is composed of the deposits of small debris flows, which have occurred since the rock avalanche event and is consistent with the weathered debris identified at the top of the slope.

Figure 3.19. A) Lobate fronts of two small debris flow deposits (Lobe II & III) penetrating out onto the floor of the rock avalanche scarp from a small gully within the tree line. The slope in the foreground (Lobe I) represents the upper surface of a larger debris flow deposit originating from somewhere near the head of the main scarp. B) Boulders comprising the front of Lobe I.

Rock fall and planar slide deposits

Rock fall and planar sliding events at Maungatautari are predominately small-scale events, restricted to the upper reaches of the mountain in areas of steep slope.

Evidence of small rock falls were found at the base of the southern edge of the rock avalanche scarp where there is located a boulder field consisting of mid- to large-sized boulders 0.5-1.5 m in diameter. Boulders were concentrated in a thin band a few metres out from the tree line at the base of the slope (Figure 3.20).

Several small-scale planar landslides are concentrated along the steep slopes that surround Te Akatarere peak and are visible in aerial photos and Google Earth™ (Figure 3.21). The scars of these slides on the mountain slopes have been present for several decades (J. Matthews, personal communication, March 31, 2017) and the largest of these slides, located on a north-facing slope measures 15 m wide by ~100 m in length.

Figure 3.20. Talus from a rock fall event consisting of andesite boulders at the base of the rock avalanche scarp.

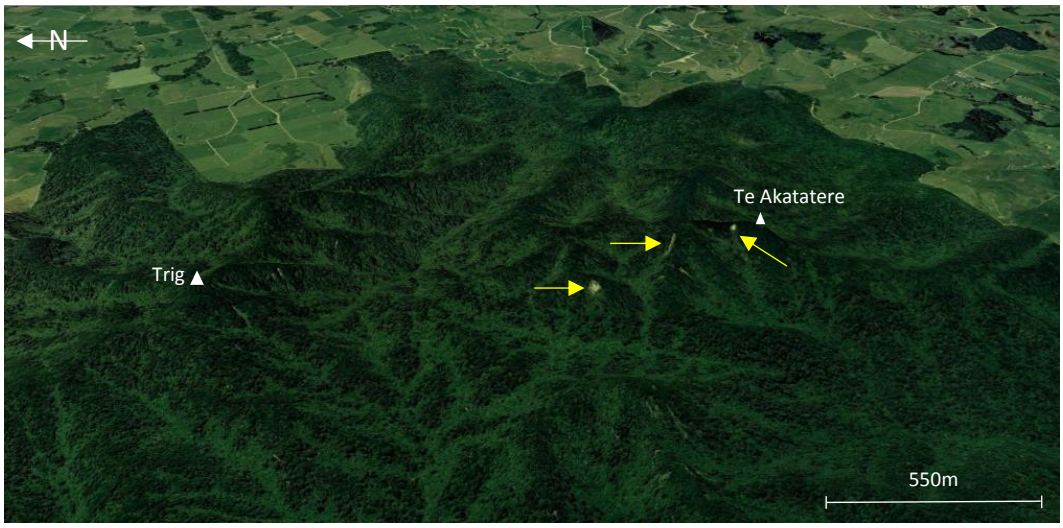

Figure 3.21. Google Earth ™ image showing a cluster of small planar landslide scars around Te Akatatere peak.

3.6 Discussion

The stratigraphic relationship between units, volcanic structure and mass-wasting events described above is discussed and compared with previous studies.

3.6.1 Stratigraphical relationships between units

The only detailed geological study of Maungatautari and its surrounds was conducted by Olson (1950) who described the mountain as an extinct multi-vent volcano built of hypersthene-bearing andesite which sits on an ignimbrite plateau, abuts a range of greywacke immediately to its west and is surrounded by a ring-plain of lahars. The mountain is now recognised to directly overlie Jurassic Manaia Hill group rocks of the Waipapa Terrane and that the thick ignimbrite plateau, now defined as the Pakaumanu Group (Mangaokewa and Raepahu Formations) originating from Mangakino Caldera to the south-east, onlaps the lower slopes of Maungatautari (Leonard *et al.*, 2010).

This study supports this current understanding with three pieces of geological evidence. Firstly, only blocks of chipwacke were found alongside various types of

andesite within the pile of rocks preserved from the removal of a large rock avalanche hummock (Section 3.56). Jurassic basement does not outcrop at the surface in the north-eastern section of the mountain, and its exact depth below the present ground level remains uncertain. However, the presence of basement strata within the rock avalanche deposit suggests that at this point, basement is relatively shallow and was excavated along with Maungatautari andesite during flank failure. Such deep-seated failures may occur in response to gravitational spreading due to extensional deformation of weak sub-edifice bedrock, a process that has been invoked for large volume rock avalanches worldwide (Clavero *et al.*, 2002; De Vries & Francis, 1997; Gaylord & Neall, 2012; Shea *et al.*, 2008). With an estimated volume of 0.28 km^3, the rock avalanche event at Maungatautari is not as large as some of its recognised counterparts, but Gaylord and Neall (2012) and Shea *et al.* (2008) highlight great diversity in the deposits and mechanisms of volcanic flank collapses at single edifices and as such, failure of sub-edifice bedrock should not be ruled out as a potential the cause of the Maungatautari rock avalanche event. The timing of this event is poorly constrained, but the lack of edifice reconstruction and absence of ignimbrites over or between hummocks suggests it occurred within the last one million years after both the volcanic activity at Maungatautari had ceased and the ignimbrite plateau had been emplaced.

Secondly, it will be shown in Chapter 4 that xenoliths of greywacke/low-grade metamorphic schists are relatively common in Maungatautari lavas. Also, lithic clasts from the pyroclastic sequence at quarry #34, described in Chapter 5, are composed of both fresh or variably altered andesite along with greywacke. The abundance of greywacke xenoliths/lithic clasts suggests fragmentation below the volcano occurred within the basement material and the absence of any other country rock lithologies, consistent with the blocks of the rock avalanche deposit, implies that the mountain sits directly above this.

Finally, field observations of the stratigraphical relationship of the units in the valleys along the eastern margins of Maungatautari, confirm the onlap of ignimbrites over the mountain's lower flanks. While the contact between

Maungatautari andesite and Mangakino caldera-derived ignimbrites is not observed, it has been inferred in Figure 3.6 using topographic contours and GIS slope models where the predominately flat plateau surface strongly contrasts with the steep slopes of the mountain (Figure 3.2). This is supported by field observations around Oreipunga, where it is apparent the Rocky Hill Ignimbrite has flowed up and around the small cone, infilling the pre-existing topography. The surface has subsequently been eroded to form broad valleys with steep bluff-like walls and isolated outliers. The andesitic lava exposure in a track cutting just to the south of Oreipunga cone at an elevation of 260 m constrains the limit of the ignimbrite plateau in this area.

The undifferentiated ignimbrite within the valley between Maungatautari and the Pukekura Hills in the southwest corner of the field area west of Maru Road shows similar geomorphology to that observed around Oreipunga Cone. The extent of the ignimbrite plateau here is constrained by the absence of ignimbrite east of Maru Road and stratigraphic logs of water bores from Waikato Regional Council (n.d.).

The relationship of the small basaltic cone of Kairangi (Figure 3.9) to Maungatautari has been considered by previous authors (Briggs *et al.*, 1989; Cole, 1978). Compositionally, Kairangi is quite distinct from the range of lava compositions found across Maungatautari and as such Briggs (1986a) determined it is geochemically unrelated, however, the possibility that Kairangi represents the inception of volcanic activity within the area was not ruled out. Situated 7 km northwest of Maungatautari, this volcanic cone sits directly on top of basement greywacke and appears to be an isolated centre. This relationship and its geochemistry are addressed further in Chapter 4.

3.6.2 Volcanic structure

Northwest-trending lineaments are a common feature associated with the volcanic centres of the North Island and have been documented within the Alexander Volcanic Group (Briggs, 1983; Kear, 1964), the southern centres of the

Kiwitahi volcanics (Cole, 1986; Kear, 1964) (Figure 2.6), the sub-parallel Little Barrier-Whangarei Volcanics (Lindsay *et al.*, 1999) and Taranaki Volcanics (Price *et al.*, 1999). This same lineament has also been documented within the TVZ with 60% of current geothermal fields located within northwest-trending accommodation zones between major fault splays (Rowland & Sibson, 2004).

The repetitive nature of northwest-trending structures across the North Island certainly suggests a significant underlying basement control which dictates the ascent of magma, and/or hydrothermal fluids and vent location at the surface. However, despite extensive seismic profiling offshore within the Taranaki Basin, no evidence of any major northwest trending structures has been found. Lindsay *et al.* (1999) proposed that these lineaments could represent crustal fractures parallel to the Vening Meinesz Fracture Zone (VMFZ). Such parallel deformation is well documented to the north of the VMFZ (Herzer *et al.*, 2011; Herzer *et al.*, 2009; Mortimer *et al.*, 2007) and is also thought likely to extend south into northern continental New Zealand (Wilson & Rowland, 2016). At Maungatautari, the major recognised volcanic vents of Kairangi, Oreipunga and an inferred eroded summit vent centred near the trig also display this northwest alignment (Figure 3.1), an observation which is consistent with the theory of an underlying structural control at depth.

A number of prominent peaks have previously been described as late-stage radial dykes and include Little Rock and Hook Nose along with two undefined outcrops on the main northern tramping track and south of Te Akatarere (Briggs, 1986b; Olson, 1950). Only the peak of Little Rock was visited during this study and rock outcrops show textural and petrographic similarities to those found at Pukeatua Peak, consisting of platy-jointed hornblende dacite lavas which taper and pinch out while others are continuous over the face of the outcrop (Figure 3.11) – features strongly characteristic of lava flows observed elsewhere on the mountain. On the north-western side of Little Rock, this short and narrow ridge dips to the northwest where it grades into the general slope of the mountain but on the other side it is bounded by bluffs. As such, in this study, Little Rock is not considered to be a radial dyke, but instead an isolated block of lava which appears to have

broken away from a more central point further up slope and a similar origin is inferred for the neighbouring peak of Hook Nose. The peak named Rocky Outcrop, however, was interpreted as a dyke and is located just south of Pukeatua Peak along the main mountain tramping track. This rocky outcrop of massive hornblende dacite is orientated at 084^{o} and has a radial attitude towards the summit, consistent with the interpretation of late-stage radial dykes by Olson (1950).

3.6.3 Mass-wasting events

The current orientation and exact location of Rocky Outcrop and the dyke south of Te Akatarere, however, may not be entirely reflective of their true in situ location. Briggs (1986b) recognised a set of subvertical shear or fault zones striking northwest in the headwaters of the Mangakara Stream which is found within the deeply incised, yet broad gully on the eastern side of the mountain (Figure 3.2). This gully extends to just below the summit where it appears to curve and merge with the upper reaches of Mangaohoi Stream gully in the west to form a distinct horseshoe shape. Figure 3.2 highlights the contrast between ridgelines in the north and south of the mountain. On the northern and north-eastern flanks the ridgelines are continuous, extending from a central point near the summit eventually blending with the topography of the surrounding ignimbrite plateau (e.g. Ridge N1). In the south, two prominent ridges (S1 and S2) are separated from the those on the east (E1) and west (W1) and each other by gullies over 800 m wide – twice the width of gullies on the northern slopes. Ridge S1 becomes increasingly discontinuous up slope, with large sections rotated off strike. While S2 is more continuous, parallel blocks are found at its base along the eastern margin of the Otautora Stream (Figure 3.2). This morphology may represent a failed rock avalanche event, with the ridges E1 and W1 forming the prominent horseshoe shaped scarp which bears strong resemblance to that of the rock avalanche at Lake Waikaremoana (Leonard *et al.*, 2010). Analogue models for the development of large volcanic rock avalanches by Paguican *et al.* (2014),

demonstrate how such events begin with faulting and fracturing of the upper edifice to create summit grabens. As strain increases, the sliding layer may split apart to create steeply-dipping escarpments parallel to the slide direction. Over-time erosional processes have exploited these structural weaknesses within the edifice to produce the broad gully systems containing the Mangakara, Mangaohoi and Otautora Streams. The oblique upper segments of ridge S1 and the blocks parallel to ridge S2 along the eastern margin of the Otautora Stream reflect the normal and strike-slip faulting required to accommodate extension, spreading, sliding and rotation of large blocks which would have evolved into hummocks within the depositional zone. Full collapse of the southern sector of Maungatautari did not occur, however, as the mountain is buttressed by the onlapping ignimbrite plateau which is known to be thickest in the south and southeast.

While gravitational spreading remains the most probable cause for slope instability, wide-angled collapse scarps like that described here, have been linked to the reactivation of one or more faults beneath large composite cones (Vidal & Merle, 2000). While no known faults lie beneath Maungatautari, active basement structures in the southern Waikato Basin around this time are unknown and therefore tectonic-induced collapse cannot be excluded.

Chapter Four:

Petrology of lavas

4.1 Introduction

This chapter describes and interprets the petrographic characteristics, whole rock major and trace element compositions of 21 new lava samples collected from the Maungatautari field area. Five of the samples were also analysed for $^{87}Sr/^{86}Sr$ and $^{143}Nd/^{144}Nd$ isotope ratios. Lava samples range from basalts to porphyritic andesites and dacites with varying amounts of plagioclase, pyroxene and hornblende phenocrysts and xenoliths, and have been differentiated using modal composition and SiO_2 content following Cole (1978) and Briggs (1986b).

The obtained results highlight similarities and differences between individual lava units with uncertain stratigraphical relationships, to investigate the origin and evolution of magmas and to aid in the understanding of how activity at Maungatautari relates to the broader context of active volcanism within the North Island of New Zealand c. 2 Ma.

4.2 Methods

Petrographical techniques involved optical microscopy, which included component analysis by point counting and X-ray powder diffraction (XRD) analysis. Whole rock geochemical analyses included X-ray fluorescence spectrometry (XRF) for major and trace elements and laser ablation inductively coupled plasma mass spectrometry (LA-ICP-MS) for rare Earth elements (REE) and selected trace elements at the Faculty of Science and Engineering, University of Waikato. A representative subset of lava samples was sent to the Geochemistry Laboratory at Victoria University of Wellington to acquire strontium and neodymium isotope data.

4.2.1 Thin Section Preparation

34 samples were cut into blocks approximately 4 cm by 2 cm and the cut face on each was then ground flat using #600 polish powder. The prepared surface was mounted onto the frosted side of a glass petrographic microscope slide using Hillquist thin section resin and hardener at a ratio of 2.3:1. Once set, the mounted

blocks were firstly cut to a thickness of ~1 mm, then ground to ~30 µm using a Struers Discoplan-TS. Coverslips were applied using petropoxy 154 at a ratio of 10:1 and allowed to cure on a hotplate until set.

4.2.2 Optical Microscopy

Thin sections were examined using a petrographic microscope in both plane and cross polarised light to identify and describe the different mineral components and textures. Quantitative data on mineral and groundmass abundances of selected samples was obtained by point counting. For each sample the stage interval was set at 0.3 mm and the number of counts per slide were recorded (minimum of 350 counts) to ensure a fair representation of the sample. The thin sections that were point counted were selected based on their representative properties.

4.2.3 X-ray powder diffraction (XRD)

X-ray powder diffraction (XRD) was used to help identify primary and secondary mineralogy of selected hydrothermally altered and extensively weathered samples obtained from localities 3, 9 and 39 (Figure 3.6) where thin section analysis was inconclusive. XRD analysis was carried out on whole rock samples which were dried and crushed into a fine powder using a tungsten-carbide ring mill. Approximately 10 grams of each of the prepared samples were then processed through the Panalytical Empyrean XRD in the Faculty of Science and Engineering, University of Waikato. The prepared samples were run for 2-80°2Θ, at 50 seconds per step. The indexing software, Highscore Plus, was used to identify mineral peaks within the resulting diffraction pattern.

4.2.4 X-ray fluorescence spectrometry (XRF)

Major and trace element geochemical analysis was conducted at the University of Waikato using the Bruker S8 Tiger XRF machine. The raw results for these geochemical analyses are presented in Appendix III.

For major element analysis, glass fusion beads were made by fusing approximately 0.8 g of powdered sample with 8 g flux (either pure 100 % Li-metaborate or 35 % Li-tetraborate, 65 % Li-metaborate) and ~ 0.7 g of NH_4 and heated in a furnace at 1050°C for 20 minutes. The sample was then poured onto a mould and fan cooled.

For trace element analysis, pressed pellets were made by mixing about 8 g of sample with 25 drops of PVA binder. This was pressed into an aluminium cap using a hydraulic press. The pressed pellet was left in an oven at 70°C for a minimum of 2 hours to evaporate off the binder.

Loss on ignition was determined by calculating the percent weight lost for ~2 g of sample after having been in the furnace at 1100 °C for about 1 hour.

4.2.5 Laser Ablation Inductively Coupled Plasma Mass Spectrometry (LA-ICP-MS)

Trace and rare earth elemental data of 21 samples were measured by LA-ICP-MS within the Faculty of Science and Engineering, the University of Waikato. A RESOlution 193 nm excimer laser within a Laurin Technic laser ablation (LA) cell was used to ablate each sample. The laser ablated phase was digested and ionised in an inductively coupled argon plasma torch (~ 8000^{o}C) (ICP) before being introduced into an Elan 6100 DRCII inductively coupled plasma mass spectrometer. In addition to Maungatautari samples and international standards, a NIST 612 standard was also analysed at the beginning, end and after every 10 unknowns. Elements analysed included Si, Al, K, Sc, Ti, V, Rb, Sr, Y, Zr, Nb, Sn, Cs, Ba, La, Ce, Pr, Nd, Sm, Eu, Gd, Dy, Ho, Er, Yb, Lu, Pb, Th and U.

Samples for LA-ICP-MS were prepared using the method outlined by Eggins (2003) which utilises lithium borate glass fusion beads following standard preparation procedures for XRF analysis. Fusion beads were stacked vertically and set in epoxy resin K36 with a ratio of 2:1 and allowed to cure on a cold, flat surface until set. The upper one third was removed using a laser saw to expose the discs as a sandwich in cross-section. The cut surface was ground flat using progressively finer abrasives before polishing to a scratch-free surface using 0.3 µm polishing alumina on a felt lap.

LA-ICP-MS specifications are presented in Appendix IV along with all raw data collected.

4.2.6 Sr and Nd extraction chromatography and isotope ratio determinations by thermal ionization mass spectrometry (TIMS)

A representative subset of lava samples were sent to the Geochemistry Laboratory at Victoria University of Wellington using the concomitant isolation procedure of Pin *et al.* (2014) where sufficiently pure fractions of Sr and Nd are obtained from a single sample.

Dried whole rock samples were crushed into a fine powder using a tungsten-carbide ring mill which was digested using a combination of HF and HNO_3. Following digestion with HF–HNO_3 and evaporation, the sample residue was dissolved using HNO_3 before the addition of ascorbic acid to reduce Fe(III) to Fe(II). The resulting solution was passed through two tandem columns containing 250 mL of Sr Spec and TRU Spec extraction chromatography resins, respectively. The upper Sr Spec column extracts Sr, while the lower TRU Spec column extracts the LREE. Sr was then back-extracted using HNO_3. The LREE were eluted directly onto a longer column containing 300 mg of the HDEHP-based EXC material Ln Spec, to obtain, through sequential elution with HCl, a Nd fraction free of any Sm contribution.

The collected Sr and Nd fractions were analysed for isotopic ratios by the high-precision mass spectrometric method of thermal ionization mass spectrometry (TIMS). Raw data for these analyses are presented in Appendix V.

4.3 Petrography and Minerology

Lavas from Maungatautari are all non-vesicular and many have seriate porphyritic textures with phenocrysts sometimes clustered as glomerocrysts. Phenocrysts include plagioclase, orthopyroxene, clinopyroxene, hornblende, opaque Fe-Ti

oxides and, within the Kairangi basalt, olivine. Phenocryst abundances range from 22 % to 53% and are set in a fine grained, plagioclase lath-dominated groundmass with intergranular, intersertal, trachytic and hyalopilitic textures. Quantification of the chemical composition of different mineral phases was not undertaken as part of this study but results of electron microprobe analyses can be found in Briggs (1986b).

Samples have been differentiated using modal composition and SiO_2 content (section 4.5.1) based on previous classifications by Cole (1978) and Briggs (1986b). Olivine basalts contain abundant olivine phenocrysts in thin section which are visible in hand specimens. Andesites and dacites are separated into: labradorite andesites, defined as containing total modal plagioclase > pyroxene; pyroxene andesites have total modal pyroxene > 15 %, while hornblende andesites and dacites contain significant hornblende which is visible in hand specimen. Representative modal analyses are presented in Table 4.1.

Table 4.1. Modal analyses of selected Maungatautari lavas based on a minimum of 350 counts per slide. OB, olivine basalt; PA, pyroxene andesite; LA, labradorite andesite; HA, hornblende andesite; HD, hornblende dacite.

Sample No.	**KSC001**	**GF006**	**MSE019**	**MRd022**	**ORE039**	**ORE040**	**HF044**	**MSE054**	**MSE056**	**MSE057**	**MSE062**
Location	Kairangi Scoria Cone	Garland lava flow	Little Rock	Hillside, Sth Mangaoha Stream	Oreipunga Cone	Gully between Oreipunga cone and fence	Hicks farm lava flow	Quarry 45	Pukeatua peak	Rocky outcrop	Trig
Petrographic classification	**OB**	**PA**	**HD**	**LA**	**HD**	**HD**	**HA**	**PA**	**HD**	**HD**	**HA**
Plagioclase (%)	2	28	28	37	26	34	28	33	18	20	27
Olivine (%)	17	-	-	-	-	-	-	-	-	-	-
Pyroxene (total %)	3	18	13	13	1	13	16	18	14	1	1
Hornblende (%)	-	-	2	-	15	3	6	1	5	15	19
Fe-Ti Oxides (%)	-	3	1	2	1	2	1	1	2	2	1
Quartz (%)	-	-	-	-	-	-	-	-	1	-	-
Groundmass (%)	78	51	56	48	57	48	49	47	60	62	52
Total (%)	100	100	100	100	100	100	100	100	100	100	100
Total crystals (%)	22	49	44	52	43	52	51	53	40	38	48

4.3.1 Phenocrysts

Olivine

The dominant phenocryst in basalt samples obtained from Kairangi Scoria Cone is olivine (Figure 4.1) with an abundance of 17 % of the whole rock. Crystals are typically euhedral to subhedral in nature and range in size from 0.5 mm to 2.25 mm. Well-developed red-brown iddingsite alteration is concentrated along the outer margins and along cracks within the larger crystals. Many of the smaller crystals have been completely altered to iddingsite pseudomorphs.

Olivine was not present within lavas obtained from the main Maungatautari edifice.

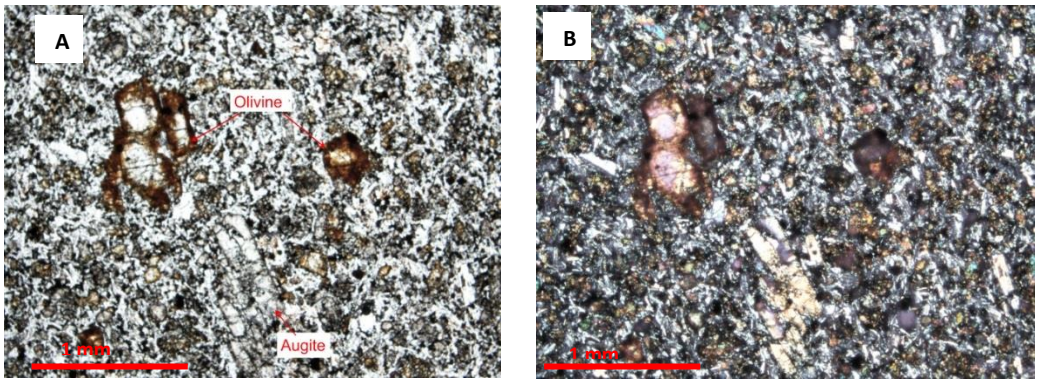

Figure 4.1. Photomicrographs of olivine basalt, sample KSC001. Olivine phenocrysts under plane polarized light (ppl) (A) and crossed-polarized light (xp) (B) show well-developed iddingsite alteration rims while smaller crystals are completely altered.

Plagioclase

Plagioclase is highly abundant and is found as large and small phenocrysts (either individual or as glomeroporphyritic crystal aggregates) (Figure 4.2) within the andesites and dacites with proportions ranging from 18 to 37 % of the whole rock and sizes typically 1.5-2 mm. A few megacrysts, however, were found to be as large as 2.5-3 mm in size. Oscillatory zoning (Figure 4.2B) and sieve-textures (Figure 4.2C) are common and some crystals show sieved centres with non-sieved rims.

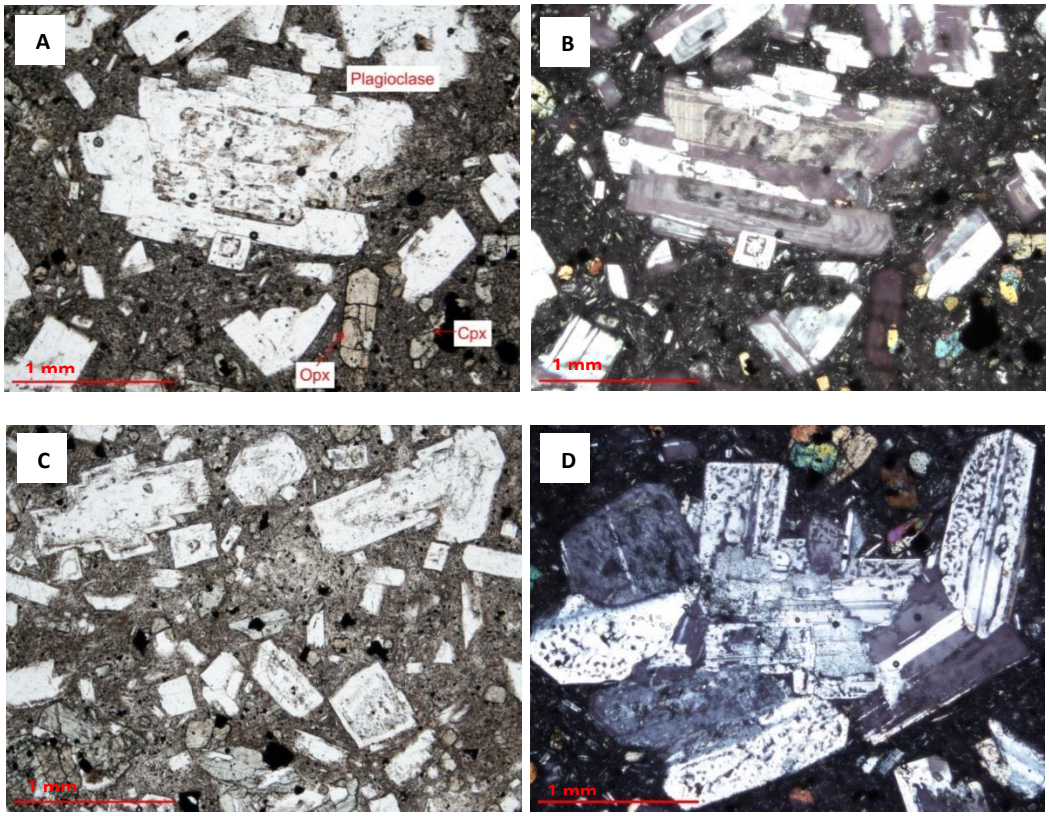

Figure 4.2. Photomicrographs of plagioclase textures. (A) Large plagioclase phenocryst from sample GF006 with sieved centre surrounded by a non-sieved rim under ppl. (B) Oscillary zoning of plagioclase crystal in image A under xp. (C) Seriate texture of sample MSE020 (ppl). (D) Glomeroporphyritic texture of plagioclase from the Garland lava flow under xp (sample GF006).

Clinopyroxene

The abundance of total pyroxene ranged from < 1-18 % of the whole rock. Clinopyroxene crystals show petrographic characteristics consistent with petrographically augite confirmed earlier with electron microprobe analysis by Briggs (1986b). They occur as euhedral to subhedral, colourless to pale green crystals of moderately high relief and inclined extinction (Figure 4.3A) and are always more abundant than orthopyroxene. Crystal sizes typically range from 0.5 mm – 1.25 mm but rarely crystals up to 2 mm were also observed. Occasionally clusters of numerous smaller crystals were observed; some having poikilitic texture with small feldspar and opaque mineral inclusions (Figure 4.3B).

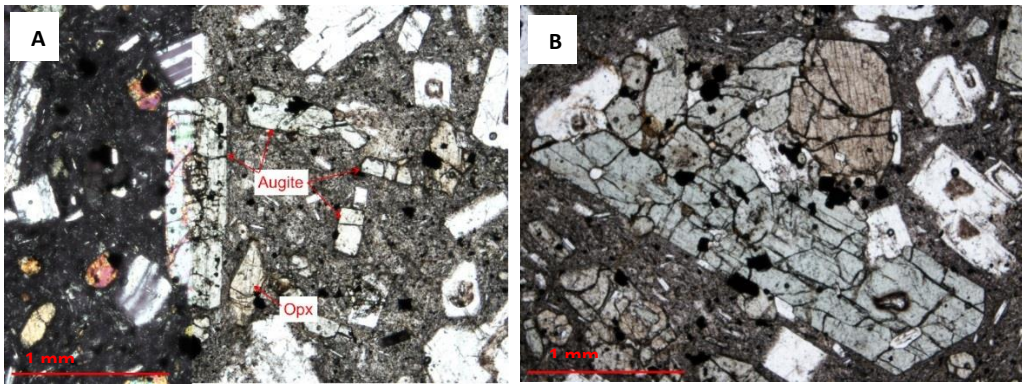

Figure 4.3. Photomicrographs of augite crystals from the Garland lava flow (sample GF006). A) Augite crystals in xp (left) and ppl (right). B) Glomeroporphyritic and poikilitic texture with inclusions of opaque minerals and feldspar.

Orthopyroxene

With sizes ranging from 0.3 mm – 1 mm, orthopyroxene phenocrysts are smaller than their clinopyroxene counterparts and are generally euhedral to subhedral in nature extinction (Figure 4.4). Petrographically, orthopyroxene crystals are distinguished from clinopyroxene by a pale peach to green pleochroism and straight extinction.

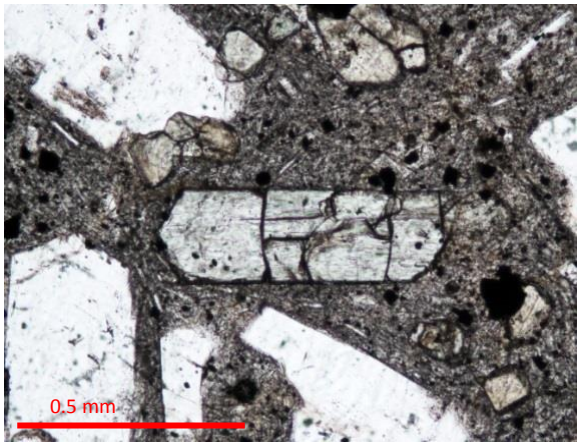

Figure 4.4. Photomicrograph of orthopyroxene crystal (centre) from the Garland lava flow (sample GF006).

Hornblende

Undifferentiated amphibole crystals, hereafter referred to as hornblende, are a common mineral phase in all dacites and some andesites (Figure 4.5) occurring as phenocrysts up to 2.5 mm in length with modal abundances ranging from < 1 % up

to 19 % in lava near the trig (sample MSE062). Crystals are pleochroic in shades of green-brown or straw-yellow to dark red-brown (Figure 4.5). Many crystals show varying degrees of alteration which ranges from thin rims of Fe-oxide and/or pyroxene to complete replacement of the original crystal by tiny Fe-oxide, pyroxene and feldspar grains.

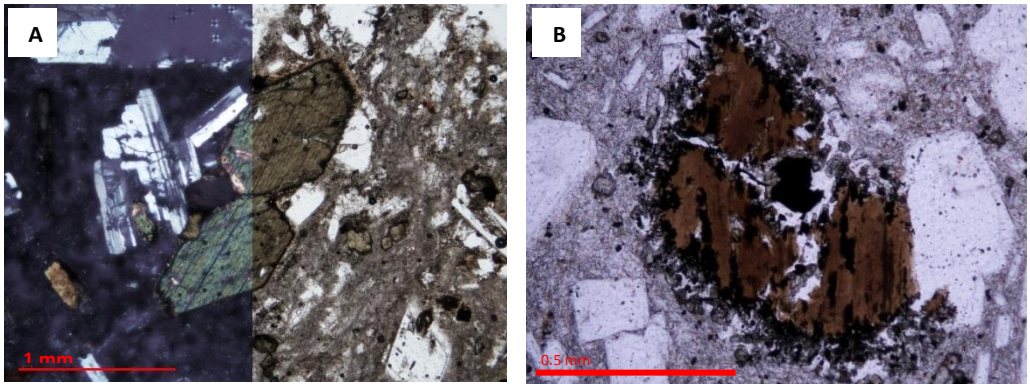

Figure 4.5. Photomicrographs of hornblende crystals. A) Fresh crystal under xp (left) and ppl (right) in lava from Oreipunga cone (sample ORE040). B) Crystal with outer rim of small pyroxenes and Fe-oxides (sample MSE019).

Opaque minerals

Small (up to 0.3 mm) microphenocrysts of Fe-oxide opaque minerals, identified as titanomagnetite by Briggs (1986b), were found in all rock types and are characterised by black cubic-shaped grains. These minerals form a minor component of the lavas with point count data showing a range of between 1 and 3% in their proportion of the bulk rock.

4.3.2 Groundmass textures

The groundmass of Maungatautari lavas is generally fine grained, dominated by plagioclase laths with intergranular, intersertal, trachytic and hyalopilitic textures (Figure 4.6).

Intergranular textures were observed in samples of olivine basalt. Plagioclase laths ranged in size from 0.1-0.3 mm which formed an interconnect network enclosing smaller grains of the other mineral phases olivine, pyroxene and

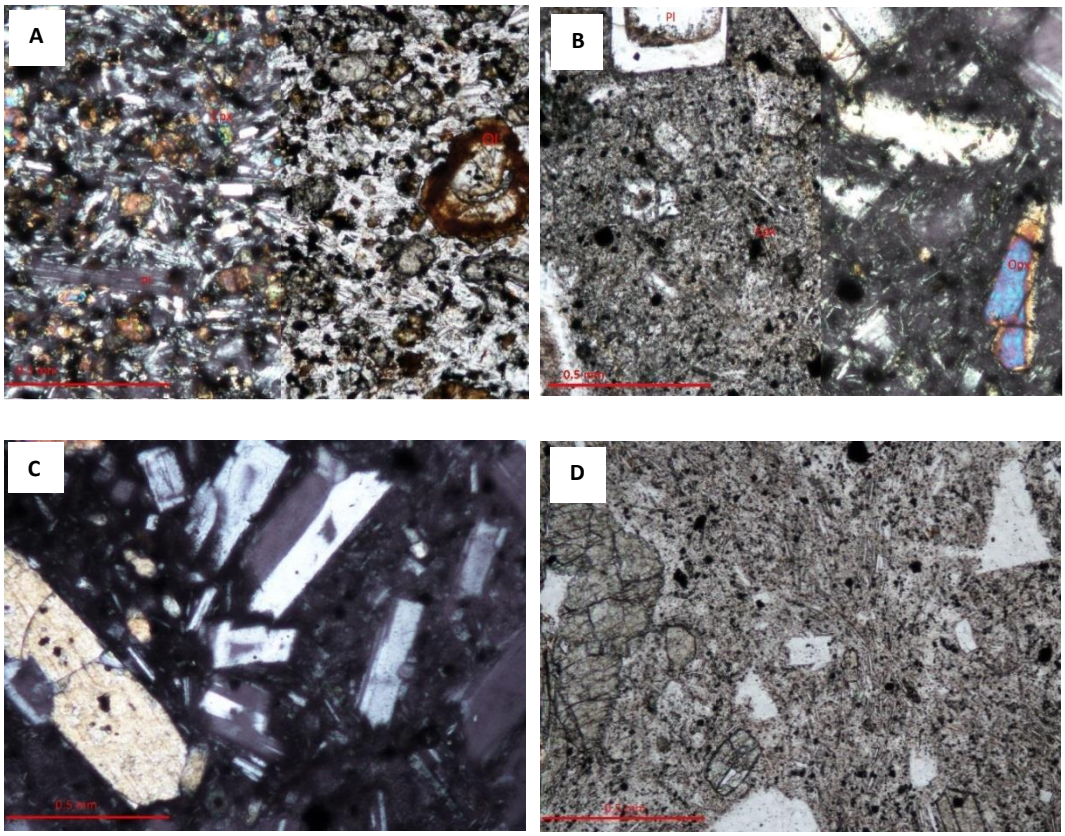

Figure 4.6. Photomicrographs of groundmass textures. A) Combined xp and ppl photo showing intergranular texture of olivine basalts (sample KSC001). B) Combined xp and ppl photo showing intersertal textures of andesites consisting of microlites and crystallites forming a random network which are set in a cryptocrystalline-glassy medium. C) Mixed hyalopilitic (left) and intersertal (right) texture in lava from Oreipunga cone (xp, sample ORE040). D) Trachytic texture with sub-parallel plagioclase laths with interstitial pyroxene and opaques (ppl, sample MSE017).

opaque minerals. Olivine and pyroxene ranged in size from 0.04-0.14 mm where individual opaque crystals were smaller measuring 0.02-0.04 mm.

Groundmass textures of the andesites and dacites consisted of intersertal and hyalopilitic textures. Typically measuring between 0.04 and 0.2 mm in size, plagioclase laths were generally smaller in these rocks than in the basalt. Within rocks with intersertal textures, microlites and crystallites formed a randomly oriented network and were set in a cryptocrystalline-glassy medium. Some samples (Figure 4.6D) displayed a trachytic texture due to flow. Other mineral phases included pyroxene, occurring as both small microlites and crystallites, and disseminated opaque minerals. In samples HF043, HF044 and MSE054, microlites of plagioclase and pyroxene were randomly distributed within a significant amount of glass, giving these samples a hyalopilitic groundmass texture.

4.3.3 Xenoliths

Two types of xenoliths were found within Maungatautari lavas (Figure 4.7). The most common xenoliths consisted of sub-spherical clasts ranging in size from < 1 cm to > 10 cm in diameter and were found in samples across the mountain. Non-vesicular, these xenoliths typically exhibited hypidiomorphic-granular textures and were comprised of predominately plagioclase and augite plus hypersthene (Figure 4.7A) or hornblende. Small opaque minerals were found disseminated throughout.

In some samples, xenoliths consisted of small (0.5 – 1.4 cm in diameter), fine-grained, dark grey angular clasts which in hand specimen displayed fine-scaled schistosity or massive textures. In thin-section, these clasts were dominated by quartz (Figure 4.7B), but also contained sparse fragments (< 0.5 mm in size) of mafic minerals such as hornblende and larger (~1 mm) crystals of an unidentified mineral.

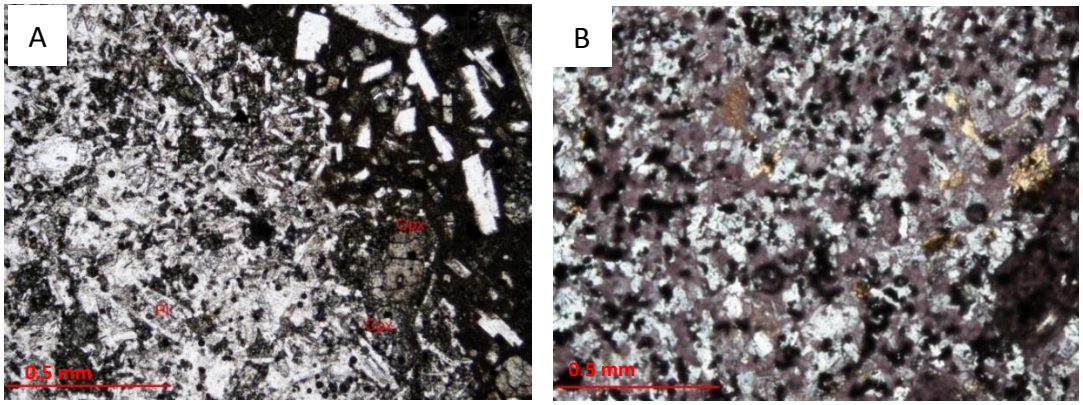

Figure 4.7. Photomicrographs of xenoliths, all in xp. A) Sub-spherical, non-vesicular xenolith consisting of mostly subhedral plagioclase and pyroxene crystals in sample MSE054. B) Quartz-dominated basement xenolith in sample MSE055.

4.3.4 Hydrothermal alteration

Samples of lava collected from the abandoned gold workings located in the headwaters of the Mangakara Stream showed varying degrees of hydrothermal alteration (samples MSE011, MSE012 and MSE014; locality 9, Figure 3.6). The least altered sample was MSE011 which was collected from a tributary stream

outcrop approximately 5 m from the mine entrance and consisted of weathered hornblende dacite (Figure 4.8A). The most intense alteration and leaching was observed in sample MSE014. In situ fluid-assisted brecciation has fragmented the host lava creating a mosaic-like texture of angular clasts, 1 to 4 cm in size which have a relict porphyritic texture (Figure 4.8). Larger clasts show little rotation and fit together in a jigsaw-like fashion. The alteration matrix of the breccia consists of a fine-grained crystalline quartz-rich medium and penetrates throughout the sample.

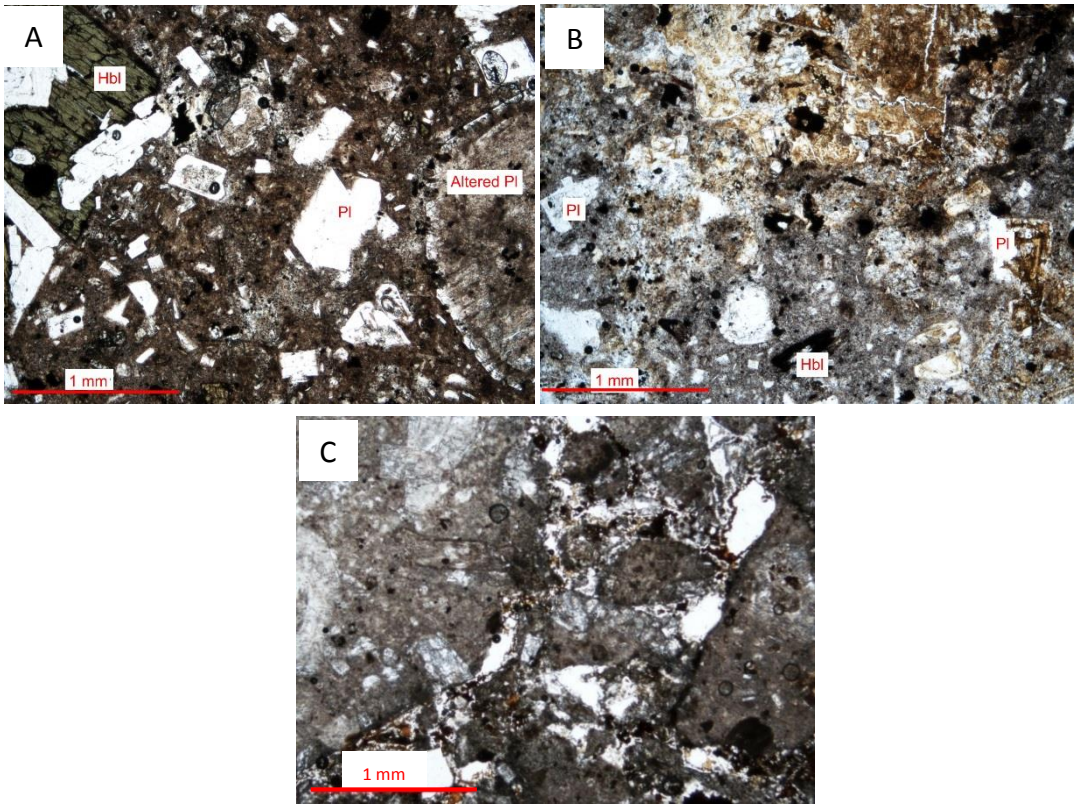

Figure 4.8. Photomicrographs of samples of varying hydrothermal alteration in ppl. A) Weathered hornblende dacite host rock (sample MSE011). B) Moderately altered dacite (sample MSE012A). C) Intense alteration of sample MSE014 showing clasts with relict porphyritic texture. Small clasts within veins are comprised of fragments of the host rock situated within a fine-grained quartz-rich medium.

4.4 X-ray Powder Diffraction (XRD)

Six weathered and hydrothermally altered samples (GF005, MSE011, MSE012, MSE014, MSE062 and MSE063) were analysed using X-ray powder diffraction (XRD). This method was used to help identify primary and secondary mineralogy that was inconclusive petrographically in samples obtained from Garland farm

(sample GF005; locality 3, Figure 3.6) and the gold workings (samples MSE011, MSE012 and MSE014) and to explain the cause of physical differences between samples of similar minerology (i.e. MSE062 and MSE063).

Peak matching was undertaken by comparing the resultant diffraction patterns to the 2016 Powder Diffraction File (PDF-4) database using the indexing software Highscore Plus. The presence of each mineral phase was then confirmed manually by identifying peaks for the three strongest lines, d_1, d_2 and d_3 respectively (Appendix II) (Cullity & Stock, 2001). The resulting diffraction patterns are shown in Figure 4.9.

All samples, except for MSE011, showed strong peaks at 4.04 Å, 2.48 Å and 2.84 Å which characterises the presence of the silica polymorph cristobalite which occurs either on its own or in association with tridymite, quartz and opal. Identification of the exact mineral phase present is often complicated by the overlap of key high intensity peaks of the polymorphs and with other minerals such as albite. In sample MSE011, cristobalite is also likely present with peaks at 4.04 Å and 2.84 Å representing lines d_1 and d_3, although a peak representing d_2 is notably absent.

The sample from Garland's farm (sample GF005) displays peaks for both cristobalite and opal in combination with K-feldspar which displays a peak at 3.77 Å which typically characterises the presence of adularia.

The goldmine samples MSE011, MSE012 and MSE014 show varying intensities of hydrothermal alteration. The most intensely altered sample (MSE014) contains three silica polymorphs (quartz, cristobalite, tridymite) along with alunite and kaolinite. Single bulk sample XRD analyses, however, are often not diagnostic for clay minerals and the presence of kaolinite is taken as indicative only. The diffraction pattern for sample MSE012 indicates cristobalite and tridymite in combination with K-feldspars, which like sample GF005, includes the peak indicating the presence of adularia. A sample of the host rock (sample MSE011), while weathered, displays minimal hydrothermal alteration in hand specimen and in this sample, the alkali feldspar, albite, features prominently in conjunction with cristobalite.

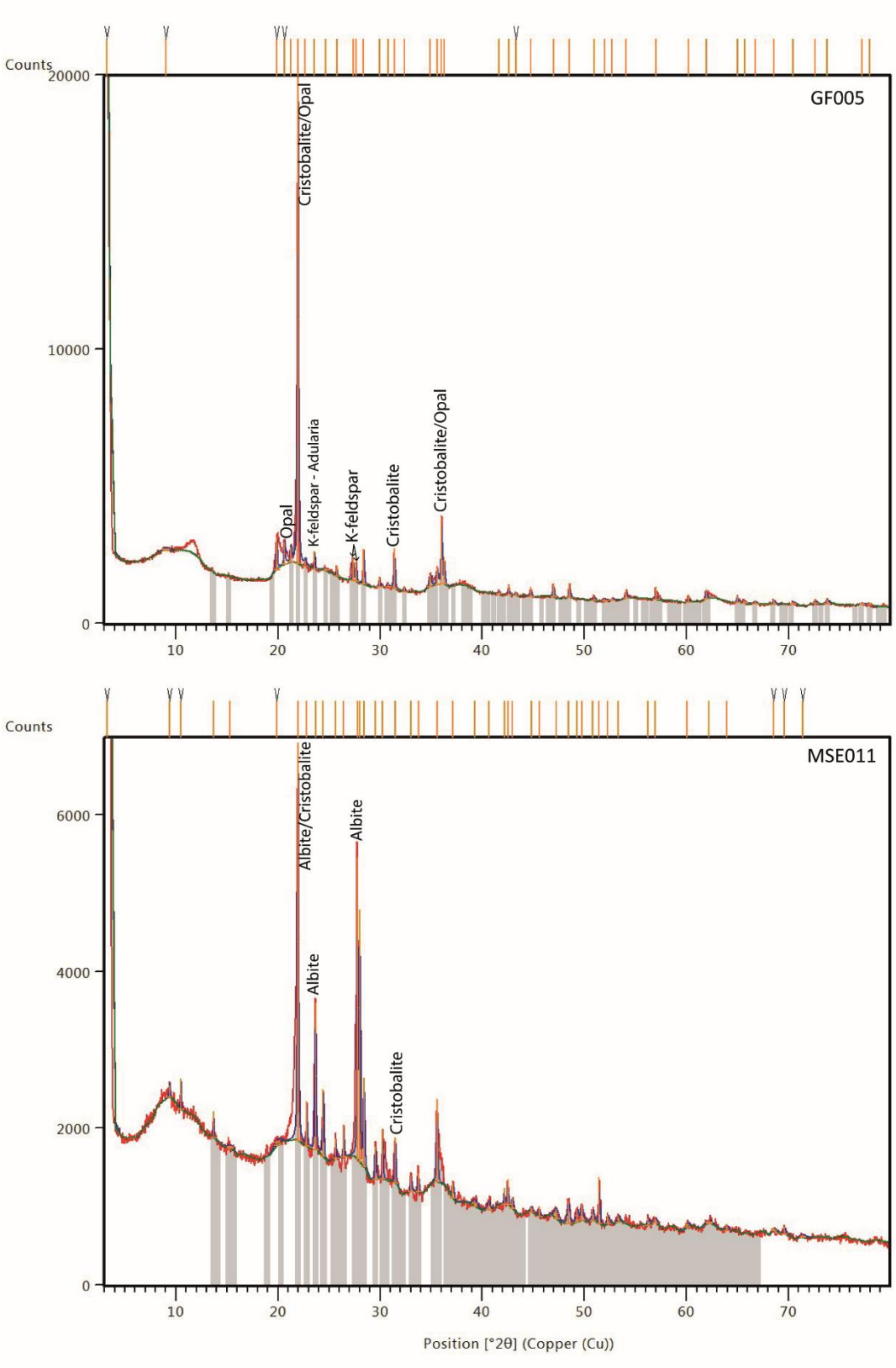

Figure 4.9. X-ray diffraction patterns for samples GF005, MSE011, MSE012, MSE014, MSE062 and MSE063.

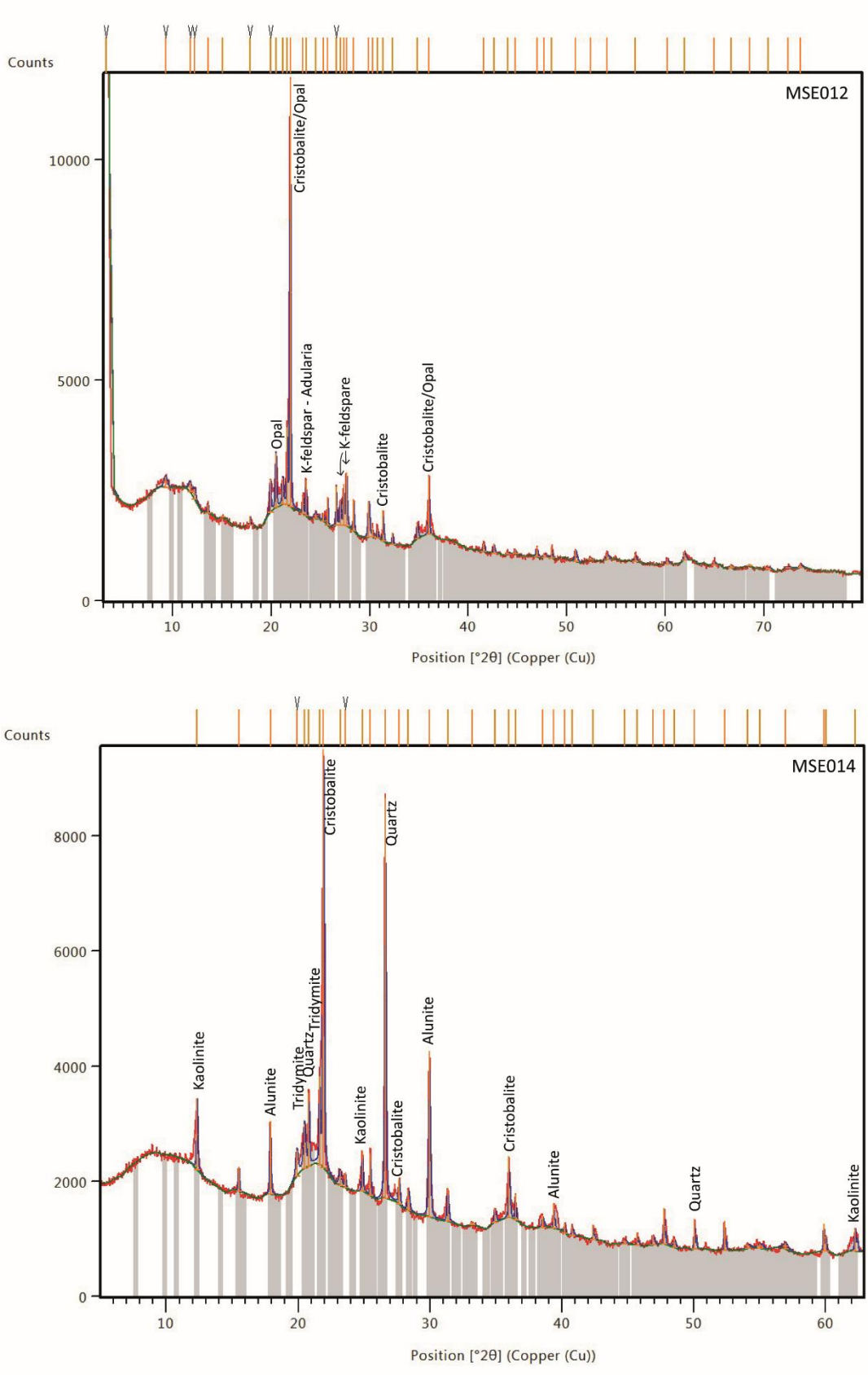

Figure 4.9 (continued). X-ray diffraction patterns for samples GF005, MSE011, MSE012, MSE014, MSE062 and MSE063.

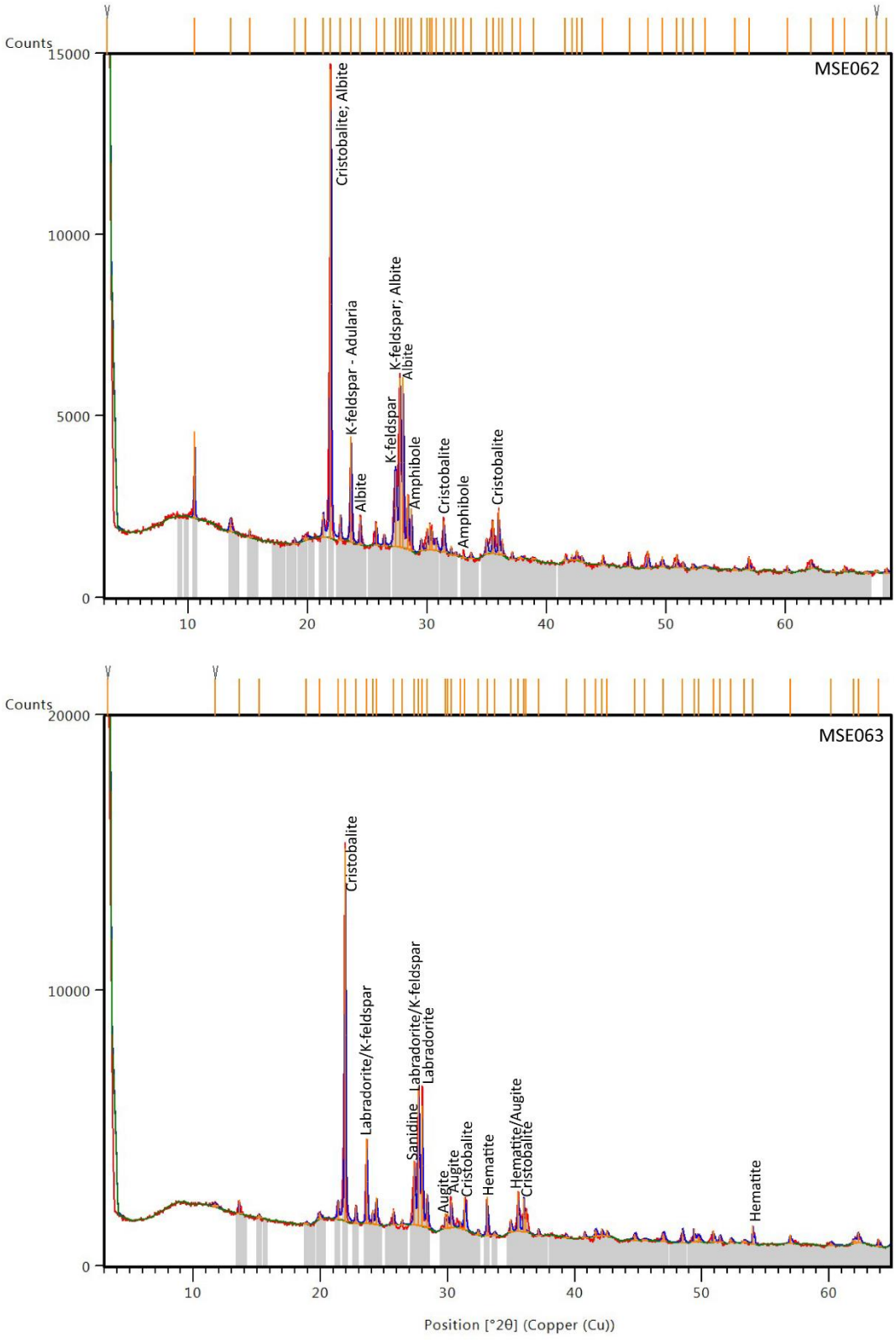

Figure 4.9 (continued). X-ray diffraction patterns for samples GF005, MSE011, MSE012, MSE014, MSE062 and MSE063.

MSE062 and MSE063 are samples of hornblende andesites collected from the trig (locality 39, Figure 3.6) during excavations of foundations for the installation of a radio tower. Petrographically these rocks are similar except in MSE063 almost complete dehydration and alteration of hornblende had occurred and it was red in colour. The diffraction patterns of these samples are also similar, strongly indicating the presence of cristobalite, albite, K-feldspars along with plagioclase (labradorite) and augite in sample MSE063. Peak matching identified amphibole in sample MSE062 which was confirmed petrographically by the presence of abundant unaltered hornblende crystals. Amphibole peaks were absent in MSE063, replaced instead with those for the iron oxide hematite, consistent with petrographic observations.

4.5 Major, trace and rare earth element geochemistry

Whole rock geochemical analyses, for major (normalised to 100 %, volatile free) and trace elements are presented in Table 4.2 and Table 4.3.

Fresh rocks were taken to be those in which LOI was less than 2.5 %. The water content of the various mineral phases of amphiboles are not enough to cause LOI to be above 2 %, so higher values (between 2.5-5 %) have been attributed to clay alteration of feldspars which is consistent with petrographic observations. Samples with LOIs above 5 % were excluded from further geochemical analyses and data interpretation. A few samples with LOIs between 2.5 and 5 % were included despite displaying weathering and alteration to gain the greatest number of analyses from as many locations as possible across the mountain.

The quality of data presented in this study is expressed in terms of accuracy and precision. In lieu of replicate and standard data for XRF analyses, data confidence is taken from the results of the University of Waikato XRF laboratory's participation in the international GeoPT round robin access on a twice-yearly basis. For GeoPT Rounds 39 and 40, the University of Waikato XRF reported SiO_2 values to within 1% relative difference (e.g. <0.5% absolute difference) of the assigned values for the distributed reference materials.

Table 4.2. Whole rock geochemical analyses by X-ray fluorescence spectrometry (XRF) of exposed Maungatautari lavas.

Sample Name	**KSC001**	**KSC002**	**GF006**	**GF007**	**MSE010**	**MSE017**	**MSE018**
Major elements (XRF, wt.%)							
(Normalized to 100% on LOI, volatile free; LOI and Total are original values; all Fe expressed as Fe_2O_3)							
SiO_2	49.65	49.70	60.68	60.47	63.61	59.39	63.58
Al_2O_3	14.61	14.46	16.54	16.57	17.58	16.37	17.71
TiO_2	1.50	1.50	0.67	0.66	0.58	0.77	0.47
MnO	0.17	0.16	0.11	0.12	0.09	0.14	0.09
Fe_2O_3	10.88	10.79	7.22	6.87	6.16	7.63	6.12
Na_2O	2.91	2.90	3.30	3.45	3.33	3.33	3.42
MgO	8.55	8.54	3.32	3.31	1.53	3.65	1.88
K_2O	1.36	1.33	2.04	2.03	2.14	2.00	2.19
CaO	10.00	10.27	5.90	6.31	4.84	6.50	4.32
P_2O_5	0.36	0.35	0.22	0.22	0.14	0.22	0.22
LOI (%)	0.62	0.69	1.72	0.92	3.60	1.48	3.35
Total (%)	99.40	99.68	100.06	100.50	100.50	100.46	100.52
Trace elements (XRF, ppm)							
F	221	308	96	115	350	166	86
S	-	12	-	-	262	-	81
Cl	290	292	197	217	1065	211	176
Sc	22	22	16	15	16	15	10
V	243	245	135	132	112	154	80
Cr	450	475	42	42	18	62	8
Co	48	49	22	22	28	26	14
Ni	147	150	18	21	15	27	10
Cu	47	47	112	53	33	44	24
Zn	83	86	58	56	61	62	49
Ga	20	19	20	18	19	19	21
As	-	-	-	-	-	-	-
Rb	35	33	76	71	56	70	76
Sr	524	530	436	468	402	456	372
Y	24	30	39	34	16	20	16
Nb	24	23	10	9	8	10	9
Cs	12	12	7	7	6	7	6
Ba	453	488	634	688	650	611	772
La	26	37	53	43	16	24	12
Ce	62	48	66	56	46	52	43
Nd	25	27	47	30	22	23	18
Pb	-	-	-	-	7	-	7
Th	6	6	10	9	10	9	10
U	-	-	-	-	-	-	-

Table 4.3. Continued.

Sample Name	MSE019	MRd20	MRd22	ORE039B	ORE040	HF043	HF044
Major elements (XRF, wt.%)							
(Normalized to 100% on LOI, volatile free; LOI and Total are original values; all Fe expressed as Fe_2O_3)							
SiO_2	63.28	61.84	58.27	63.68	58.75	58.46	58.40
Al_2O_3	17.00	17.37	17.52	18.15	17.52	16.97	17.75
TiO_2	0.48	0.65	0.68	0.59	0.70	0.68	0.68
MnO	0.11	0.11	0.12	0.15	0.13	0.20	0.16
Fe_2O_3	5.88	5.93	7.94	6.59	7.92	7.89	8.08
Na_2O	3.65	3.70	3.25	3.42	3.19	3.15	2.91
MgO	2.04	2.55	3.40	0.67	3.48	3.70	3.82
K_2O	2.12	1.99	1.91	2.42	1.96	1.95	1.95
CaO	5.20	5.64	6.68	4.09	6.11	6.81	6.03
P_2O_5	0.22	0.23	0.23	0.26	0.22	0.21	0.22
LOI (%)	1.72	1.31	1.63	2.84	2.03	1.58	3.18
Total (%)	100.43	100.78	100.65	100.82	100.51	100.72	100.88
Trace elements (XRF, ppm)							
F	63	254	115	92	117	12	70
S	-	-	-	865	276	-	-
Cl	224	224	230	1018	569	295	441
Sc	11	12	15	12	16	18	16
V	86	131	153	119	160	161	162
Cr	8	4	23	6	17	37	117
Co	18	25	27	34	25	42	27
Ni	8	10	12	11	14	19	27
Cu	24	25	30	25	40	41	44
Zn	50	66	62	65	71	69	64
Ga	19	19	20	20	20	18	20
As	-	-	-	-	-	-	-
Rb	74	67	69	86	69	70	70
Sr	437	421	454	414	368	399	363
Y	18	21	22	24	93	74	166
Nb	9	8	8	9	8	8	8
Cs	6	6	7	-	7	6	9
Ba	737	644	561	713	798	726	709
La	19	19	18	29	41	62	160
Ce	47	56	48	55	43	65	71
Nd	28	23	22	26	53	65	130
Pb	-	-	-	6	-	-	-
Th	9	7	7	11	8	7	8
U	-	-	-	-	-	-	-

Table 4.3. Continued.

Sample Name	MSE045	MSE053	MSE054	MSE056	MSE057	SF060	MSE062
Major elements (XRF, wt.%)							
(Normalized to 100% on LOI, volatile free; LOI and Total are original values; all Fe expressed as Fe_2O_3)							
SiO_2	60.39	57.34	58.83	63.88	66.45	59.53	62.07
Al_2O_3	18.63	17.66	17.57	18.05	16.85	18.49	18.47
TiO_2	0.69	0.69	0.76	0.52	0.52	0.67	0.57
MnO	0.10	0.13	0.11	0.09	0.05	0.16	0.13
Fe_2O_3	7.28	8.34	7.15	6.01	5.13	7.92	7.12
Na2O	2.97	3.17	3.27	3.23	3.42	2.98	3.19
MgO	2.92	3.69	3.34	1.97	1.10	3.09	1.79
K_2O	2.15	1.88	1.95	2.37	2.77	2.06	2.29
CaO	4.67	6.86	6.79	3.69	3.54	4.87	4.13
P_2O_5	0.22	0.24	0.24	0.19	0.16	0.23	0.24
LOI (%)	5.11	1.64	1.73	4.05	3.75	4.15	4.09
Total (%)	100.86	101.00	100.85	100.03	99.88	100.99	100.88
Trace elements (XRF, ppm)							
F	124	100	165	107	242	11	-
S	56	-	-	-	-	-	-
Cl	267	240	157	110	211	174	227
Sc	14	16	17	12	9	16	12
V	150	162	173	91	83	151	130
Cr	30	15	16	4	9	31	5
Co	24	25	25	14	17	23	23
Ni	7	16	13	8	9	11	12
Cu	21	45	31	28	26	31	15
Zn	67	66	68	57	61	63	61
Ga	19	20	20	19	18	20	19
As	-	-	-	-	-	-	-
Rb	72	66	65	84	103	68	80
Sr	305	468	459	322	358	326	400
Y	21	20	19	21	20	17	17
Nb	8	7	7	8	11	8	8
Cs	6	7	7	5	5	6	-
Ba	734	556	564	722	845	651	716
La	18	15	21	26	33	12	19
Ce	44	48	41	50	58	47	42
Nd	21	19	23	29	29	15	18
Pb	-	6	-	6	7	5	-
Th	8	8	7	10	14	10	10
U	-	-	-	-	-	-	-

Table 4.3. Whole rock trace element geochemical analyses by laser ablation inductively coupled plasma mass spectrometry (LA-ICP-MS) of exposed Maungatautari lavas

Sample Name	KSC001	KSC002	GF006	GF007	MSE010	MSE017*	MSE018*
Trace elements (LA-ICP-MS, ppm)							
Sc	25.20	24.50	13.86	13.08	12.09	15.83	9.94
V	244.40	239.10	171.90	173.00	135.40	185.80	133.95
Rb	21.10	21.00	52.90	49.00	37.60	47.80	53.00
Sr	421.00	417.10	346.40	384.50	326.20	365.90	301.35
Y	17.55	21.27	27.40	25.70	11.70	14.65	12.14
Zr	113.60	108.40	118.20	120.10	113.00	117.55	122.85
Nb	18.90	17.96	7.41	7.17	7.21	7.66	7.91
Cs	0.46	0.32	1.87	1.75	1.53	1.16	1.83
Ba	320.20	327.20	512.00	515.00	512.00	479.00	556.00
La	23.00	28.50	41.90	35.20	18.90	20.50	19.20
Ce	40.90	37.40	45.30	41.50	35.70	37.60	35.15
Pr	4.93	5.06	8.56	6.20	3.55	4.40	4.01
Nd	25.70	25.70	38.00	27.60	19.20	21.60	21.25
Sm	4.00	4.80	6.40	3.78	2.39	3.50	2.97
Eu	1.19	1.47	1.99	1.44	0.95	1.22	0.87
Gd	3.54	3.98	6.20	4.90	2.04	3.28	2.48
Dy	2.90	4.20	4.94	3.91	2.04	2.98	2.08
Ho	0.71	0.69	0.92	0.77	0.39	0.56	0.44
Er	1.94	2.20	2.88	1.45	1.70	1.37	1.33
Yb	2.03	1.33	2.93	2.29	0.98	2.04	1.24
Lu	0.19	0.29	0.42	0.38	0.20	0.21	0.17
Pb	1.92	2.85	3.29	4.60	3.39	3.31	4.60
Th	3.36	3.37	6.94	7.08	7.36	6.85	6.90
U	0.98	0.93	1.42	1.73	1.43	1.53	1.87

* Results presented are an average of two spot analyses on the same sample

Table 4.4. Continued.

Sample Name	MSE019*	MRd20	MRd22	ORE039B*	ORE040	HF043	HF044
Trace elements (LA-ICP-MS, ppm)							
Sc	10.72	11.60	15.75	9.97	16.30	19.10	17.90
V	134.95	151.40	197.20	151.60	205.60	214.50	207.80
Rb	52.95	48.40	49.60	63.00	48.10	50.80	48.90
Sr	365.80	353.90	382.10	347.10	304.60	330.40	303.10
Y	15.20	15.90	16.90	19.00	74.60	57.80	131.60
Zr	121.30	118.10	111.70	141.90	107.40	112.90	109.60
Nb	7.92	7.37	6.98	8.78	6.84	6.02	6.30
Cs	1.26	0.79	1.47	1.09	1.63	1.56	1.34
Ba	604.50	519.00	481.00	600.00	488.00	567.00	531.00
La	23.75	22.90	21.50	29.00	34.10	48.00	116.30
Ce	41.30	43.70	39.30	48.30	37.60	50.40	54.00
Pr	5.26	4.44	4.09	6.43	9.73	12.80	27.10
Nd	25.70	24.30	23.10	28.50	42.10	49.80	97.90
Sm	4.70	2.86	4.90	4.96	10.20	12.10	21.60
Eu	1.12	1.16	0.99	1.07	3.07	2.74	6.50
Gd	2.97	3.40	4.20	3.47	12.30	10.30	23.20
Dy	2.61	2.68	2.50	3.32	12.70	8.40	21.10
Ho	0.48	0.47	0.55	0.76	2.44	1.97	4.36
Er	1.57	1.05	1.26	2.00	6.40	6.20	12.60
Yb	1.54	2.12	1.67	2.26	6.40	5.40	10.70
Lu	0.19	0.33	0.20	0.35	1.12	0.84	1.63
Pb	3.84	2.45	4.99	6.00	4.32	4.83	3.84
Th	7.35	6.92	5.92	9.14	5.99	6.31	6.50
U	1.70	1.59	1.53	2.03	1.54	1.39	1.36

***** Results presented are an average of two spot analyses on the same sample

Abundances of SiO_2 from XRF analyses were used to in addition to NIST 612 to calibrate LA-ICP-MS results. Three international MPI-Ding standards StHs6/80-G, ML3B-G and GOR128 were used to ensure data quality. StHs6/80-G and ML3B-G are of andesitic and basaltic composition respectively, which are similar to the rock types found at Maungatautari.

Accuracy indicates the relative proximity of measured results to the certified values for the international standards. Precision refers to how close each analysed value is with respect to the mean of within-run replicates. Accuracy and precision of the LA-ICP-MS data were evaluated using percent difference (%diff) (Eq. 1) and relative standard deviation (%RSD) (Eq. 2), respectively.

$$\%\, diff = \frac{x_{av} - x_{std}}{x_{std}} \times 100 \qquad \text{(Eq. 1)}$$

$$\%\, RSD = \frac{\sigma}{x_{av}} \times 100 \qquad \text{(Eq. 2)}$$

where x_{av} is the average value of the repeated LA-ICP-MS measurements, and x_{std} is the published value of the certified standard. Elemental %diff and %RSD and regression analysis graphs for each standard are presented in Appendix IV.

The %diff of the LA-ICP-MS data for Al, Ti, V, Rb, Sr, Y, Zr, Nb, Ba, La, Ce, Pr, Sm, Eu, Gd, Dy, Ho and U was less than 10 % and generally less than 20 % for K, Sc, Cs, Nd, Er, Yb, Lu, Pb and Th across the three standards used. The analyses of Sn showed poor accuracy with a %diff of greater than 50 % which typically occurs when concentrations approach detection limits. The %RSD for most elements was generally better than 3%, and between 3 and 10 % for Y, Cs, Pr, Eu, Yb, Lu and Th for the standards NIST 612, StHs6/80-G and ML3B-G. For the standard GOR128, most elements gave %RSD values better than 11 %, however, U showed poor precision with 35 % variance.

The elements Si, Al, K, Ti, Sc, V, Rb, Sr, Y, Zr, La, Ce, Nd, Pb and Th were analysed using both XRF and LA-ICP-MS. The major elements Al, K and Ti, analysed using

LA-ICP-MS demonstrate a wide variability in accuracy and as such, data obtained via XRF was used for the TAS diagram, K-type classification and Harker variation diagrams presented below. In contrast, LA-ICP-MS trace element data has been demonstrated to be both precise and accurate and is therefore used in favour over the XRF data for the above elements where applicable and used exclusively to produce the multi-element spider diagrams.

4.5.1 Rock classification

Maungatautari lavas have been classified using a total alkali versus silica (TAS) diagram (Figure 4.10). Samples range in composition from basalt (at Kairangi) to andesite and dacites across all samples from the main edifice. The division between rock units follows Le Maitre *et al.* (2002) where: basalts contain 45-52 wt. % SiO_2; basaltic andesite, 52-57 wt. % SiO_2; andesite, 57-63 wt. % SiO_2 and dacite, 63-77 wt. % SiO_2. No samples of basaltic andesite composition were located.

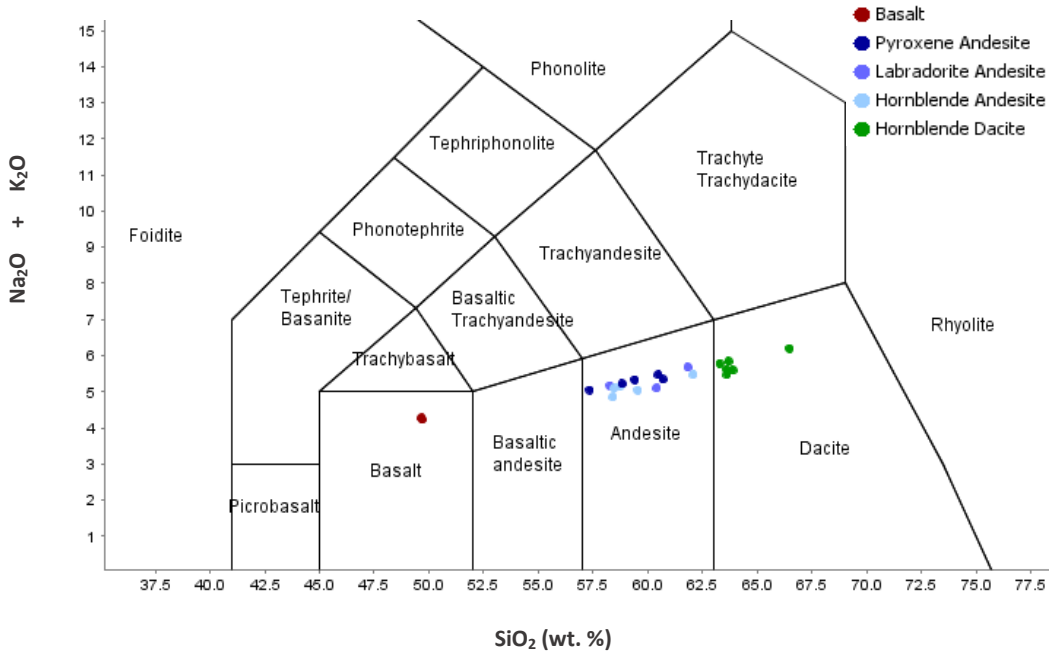

Figure 4.10. Chemical classification of volcanic rocks using total alkalis versus silica (TAS) diagram of (Le Maitre et al., 2002).

Andesites and dacites were further classified into low-K, medium-K and high-K (Figure 4.11). These rocks show a generally smooth trend on the K_2O-SiO_2 diagram which projects within the medium-K field but close to the high-K boundary.

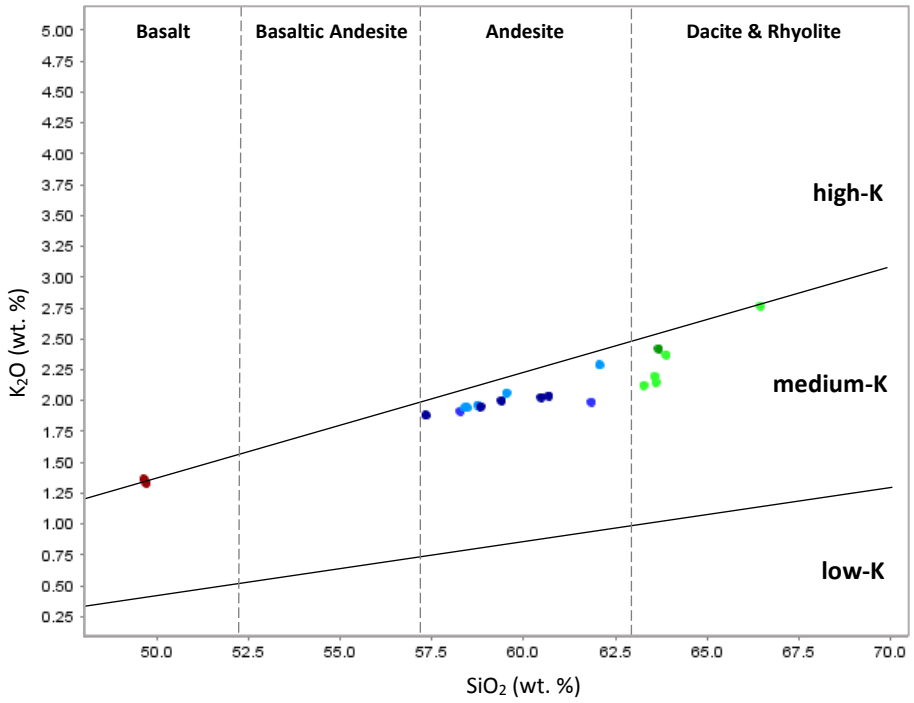

Figure 4.11. Division of basalt-rhyolite series into low-K, medium-K and high-K types. Dashed lines indicate rock type boundaries as in the TAS diagram of Figure 4.10 (Le Maitre et al., 2002).

An alternative to the TAS diagram is the Nb/Y classification diagram of Winchester and Floyd (1977) which uses selected minor and trace elements to classify the differentiation products of volcanic rocks in a similar manner to methods using normative or major-element indices. Figure 4.12 uses the ratio Zr/TiO_2 as a differentiation index for common volcanic rocks and the Nb/Y ratio as an alkalinity index, which is useful as these elements are usually unaffected by hydrothermal alteration processes. On this diagram, most samples from the main edifice plot within the andesite and dacite fields consistent with the TAS diagram, however, three samples of hornblende andesite sit outside the main cluster to the left of the diagram. The olivine basalt is also recognised to belong to the alkaline, rather than subalkaline magma series.

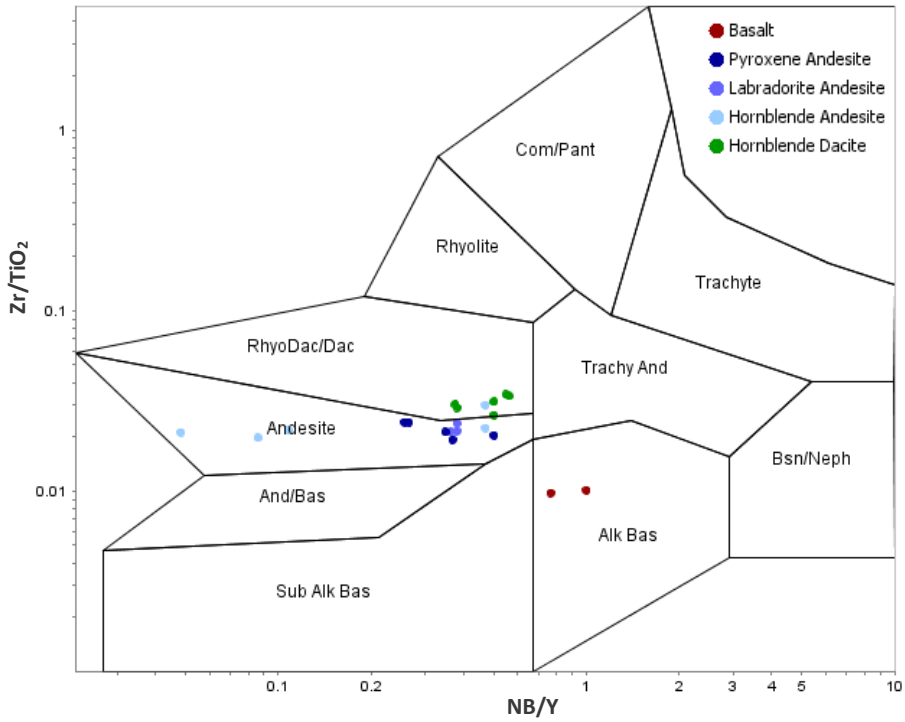

Figure 4.12. Volcanic rock classification diagram using trace elements after Winchester and Floyd (1977).

4.5.2 Major Element Geochemistry

Major element compositions are listed in Table 4.2 and Harker variation diagrams for Fe_2O_3, CaO, MgO, TiO_2, Na_2O, K_2O and Al_2O_3 verses SiO_2 are shown in Figure 4.13 where all Fe is expressed as Fe_2O_3.

SiO_2 abundances range from 49.65 to 66.45 wt. % (normalised to 100% volatile free). With increasing SiO_2 content, there is a progressive decline in abundance of Fe_2O_3, CaO, MgO and TiO_2, whereas Na_2O and K_2O progressively increase. The well-defined trends within these major elements strongly imply that the rocks are related via fractionation and are consistent with the primary rock classifications of Figure 4.10. Al_2O_3 values show significant spread, and as such no definite trend is distinguishable.

The olivine basalts contain higher concentrations of the mafic oxides of Fe_2O_3, MgO, CaO and TiO_2 and plot distinctly separate, generally above the main trend line for the andesites and dacites.

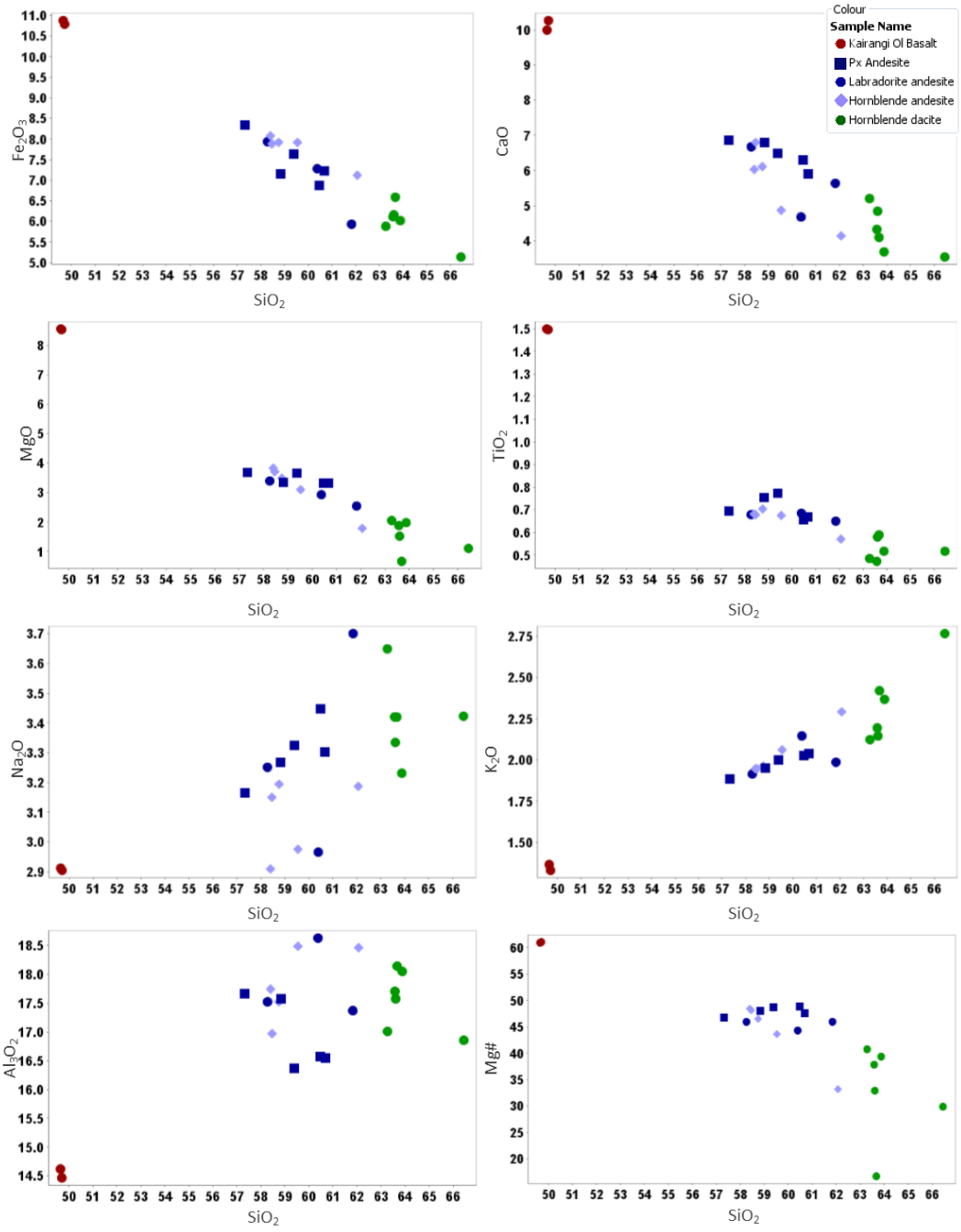

Figure 4.13. Harker variation diagrams for major elements and Mg# for 21 analysed samples from Maungatautari. All Fe is expressed as Fe_2O_3.

Across the main edifice, the analysed whole rock lavas have abundances of Fe_2O_3 between 5.13 and 8.34 wt. %. CaO abundances vary from 6.86 to 3.54 wt. % while MgO ranges between 3.82 to 0.67 wt. %. TiO_2 had recorded values of 0.77 to 0.47 wt. %. For the incompatible elements Na_2O and K_2O, abundances were between

2.91 wt. % and 3.70 wt. % and 2.77 wt. % to 1.88 wt. % respectively. Al_2O_3 concentrations show little variation with values of 18.63 wt. % and 16.37 wt. %.

The eruption of high magnesium number (Mg#) lavas has occurred at numerous North Island volcanoes (Booden *et al.*, 2010; Cole & Teoh, 1975; Froude & Cole, 1985). According to the definition of Kelemen *et al.* (2013), high-Mg# andesites are rocks of >54 wt. % SiO_2 and Mg# >50. The Mg# of Maungatautari lavas varies between 30 and 49 (Figure 4.13) and therefore cannot be classified as high-Mg andesites.

4.5.3 Trace Element Geochemistry

Trace element compositions are listed in Table 4.2 and Table 4.3. Harker variation diagrams for nickel (Ni), chromium (Cr), scandium (Sc), niobium (Nb), strontium (Sr), yttrium (Y), vanadium (V) and barium (Ba) are shown in Figure 4.14 with elements showing a mixture of compatible, incompatible and flat trends.

Compatible trace elements consist of scandium, strontium and vanadium. While scandium and vanadium show well-defined decreasing trends in concentration with increasing silica, strontium shows significant scatter with samples of lowest concentrations being a mixture of andesite and dacite rock compositions. In contrast, niobium and barium show distinct incompatibility, increasing in concentration along with silica. Nickel, chromium and yttrium have essentially flat profiles with no discernible trend. The concentration of nickel and chromium are low except within the basalts, yet the concentration of yttrium for all samples is below 30 ppm, except for the three hornblende andesites ORE040, HF043 and HF044 which have concentrations ranging from 60 to 130 ppm.

As observed within the major elements, the olivine basalt from Kairangi sits significantly separate from the andesites and dacites of the main edifice. In these rocks, concentrations of Ni, Cr, Sc and Nb are significantly higher at 147-150 ppm, 450-475 ppm, 24.5-25.2 ppm and 17.96-18.09 ppm respectively. With concentrations of 417.1-421.0 ppm for Sr and 17.55-21.27 ppm for Y, these

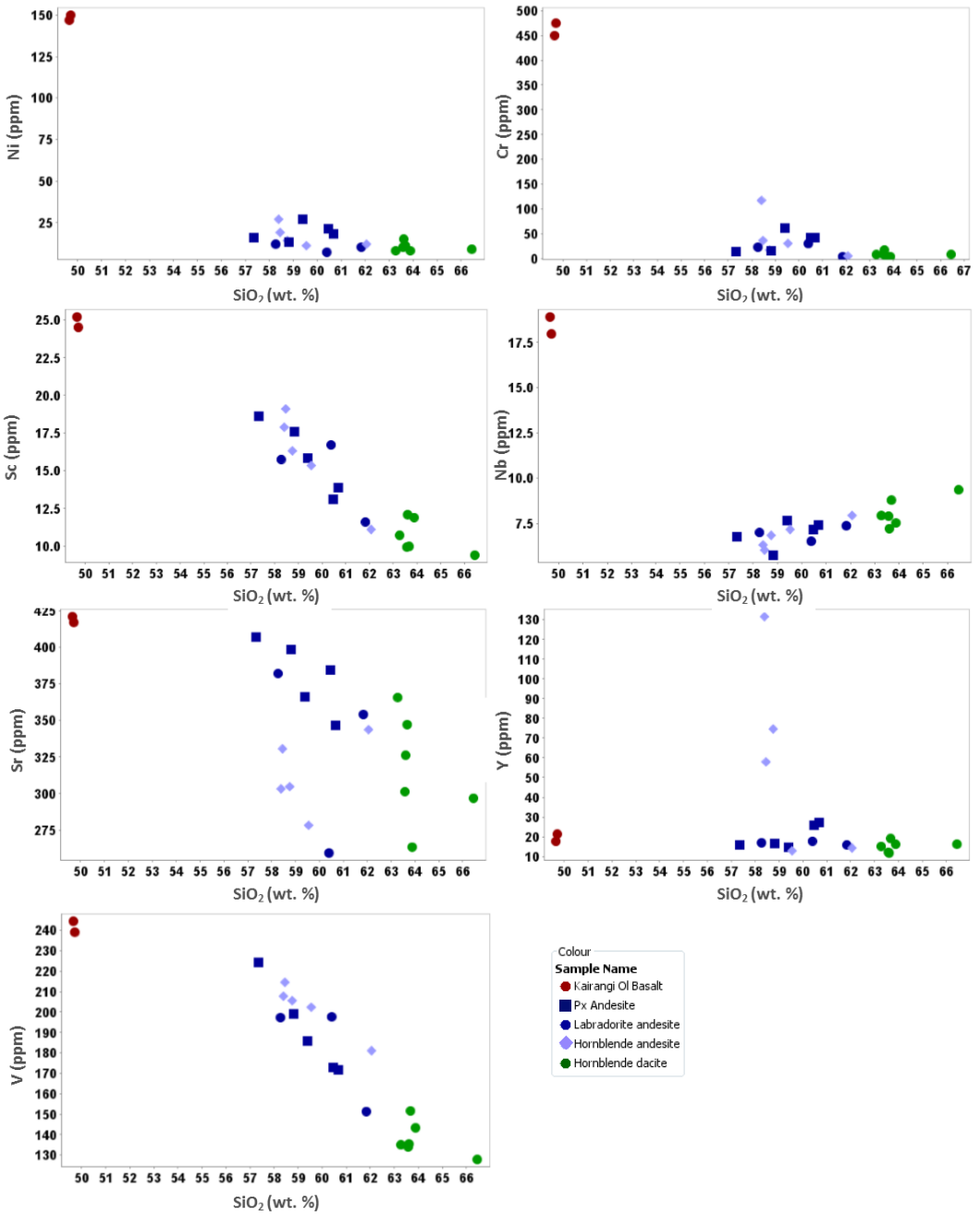

Figure 4.14. Harker variation diagrams for trace elements nickel (Ni), chromium (Cr), scandium (Sc), niobium (Nb), strontium (Sr) and yttrium (Y) for 21 analysed samples from Maungatautari.

elements have more similar values to the averages for Maungatautari andesites and dacites of 335 ppm and 17.0 ppm for Sr and Y respectively.

Figure 4.15 is a rare Earth element (REE) plot normalised to normal mid-ocean ridge basalt (N-MORB). Most samples show a similar trend with a moderate negative slope across the light REE which then flattens out across the heavy REE.

A negative Ce anomaly is observed along with a slight negative Eu anomaly amongst the hornblende andesites and dacites. Concentrations of the heavy REE also sit below the N-MORB reference line at 1. The REE pattern for the hornblende andesites, however, differs from the other samples. These rocks are more enriched in both the light and heavy REE and have a La/Y slope which is much flatter with stronger negative Ce and Eu anomalies. Heavy REE compositions sit above the N-MORB reference line.

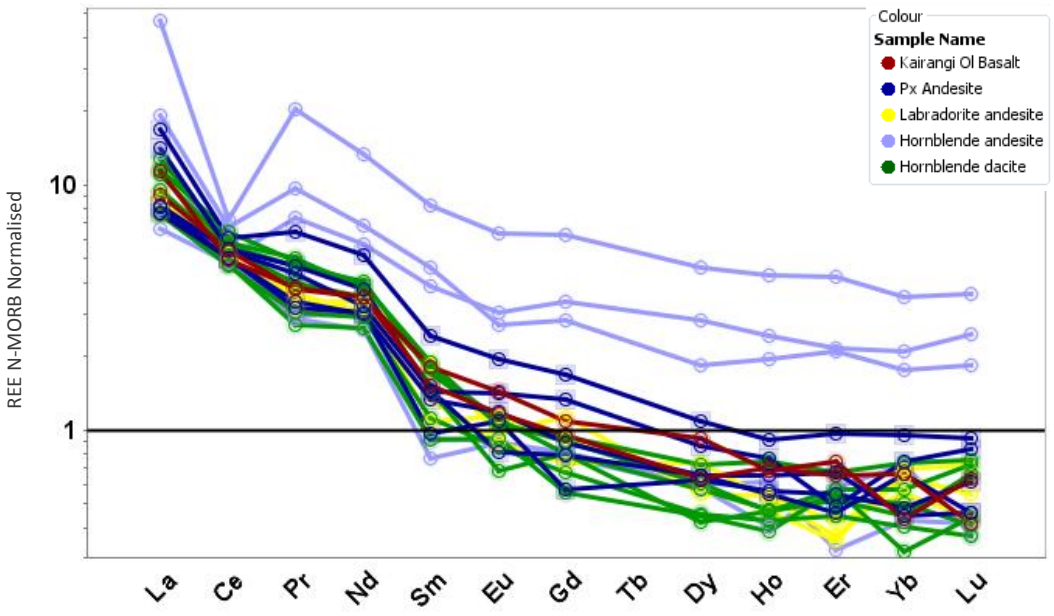

Figure 4.15. N-MORB normalised REE diagram for Maungatautari lavas (after Sun and McDonough (1989)).

A primordial mantle-normalised multielement diagram is shown in Figure 4.16. There is a distinct decoupling between the patterns of the large ion lithophile (LIL) elements K, Rb, Cs and high field strength (HFS) elements Zr, Nb, Hf, Th, U, Ta and rare Earth elements. This demonstrates the enrichment of LIL elements and Th which are separated from other elements in the diagram by a strong negative Nb anomaly. The general pattern for Maungatautari lavas is very clear, however, two distinct variations are also evident. The Kairangi olivine basalts are less enriched in LIL elements with a less pronounced negative Nb anomaly. While the hornblende andesites have LIL element concentrations consistent with other

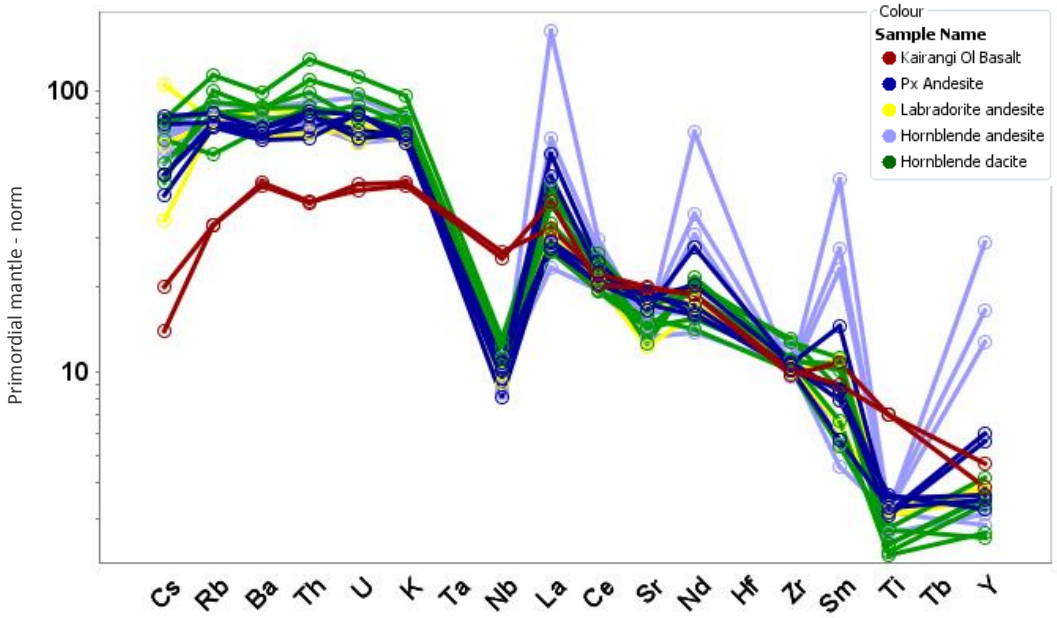

Figure 4.16. Trace element distribution diagram normalized relative to primordial mantle composition of McDonough et al. (1992) for Maungatautari lavas.

samples from the main Maungatautari edifice, three samples, ORE040, HF043 and HF044 are more enriched in La, Nd, Sm and Y and display strongly negative Ce anomalies.

4.5.4 Comparison to North Island volcanic centres

This section compares Maungatautari geochemical data to averaged published data on the Coromandel Volcanic Zone (Booden *et al.*, 2012), Kiwitahi (Booden *et al.*, 2010), Ruapehu (Price *et al.*, 2012), Alexandra (Briggs, 1986a; Briggs & Goles, 1984) and Taranaki (Price *et al.*, 1999) volcanic centres and the Okete intra-plate volcanics of the western North Island (Briggs & McDonough, 1990).

Figure 4.17 is a rare earth element (REE) plot normalised to normal mid-ocean ridge basalt (N-MORB), which is accompanied by a primordial mantle-normalised multielement diagram (Figure 4.18). Figure 4.17 shows three distinct groupings. The first group includes the recognised subduction-related magmas of the Coromandel Volcanic Zone and Ruapehu which display trends starting with a moderate negative slope across the light REEs, then flattening out across the heavy REEs to below the MORB reference line with slight negative Eu anomalies.

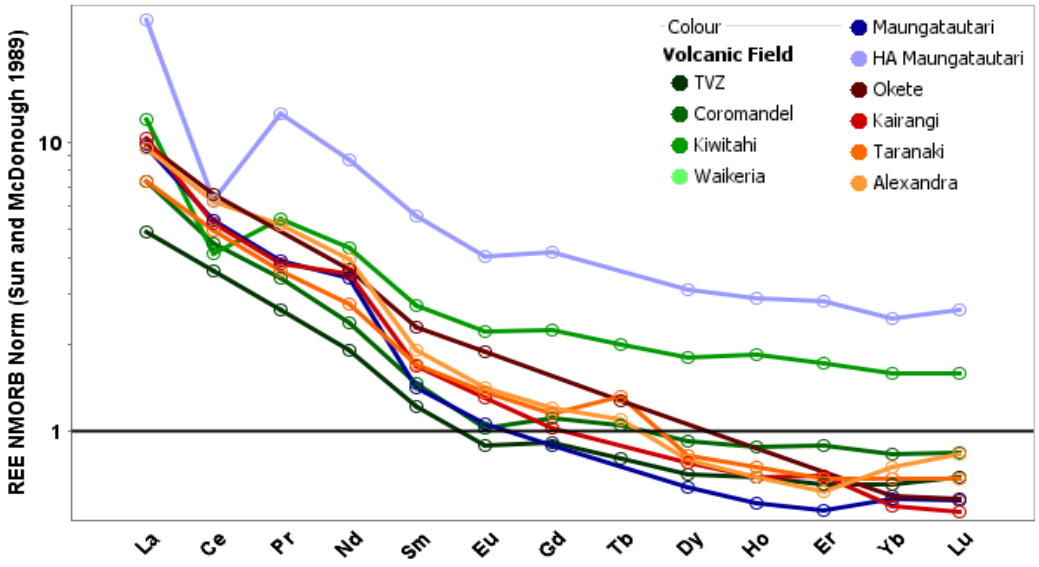

Figure 4.17. N-MORB normalised REE diagram after Sun and McDonough (1989) for averaged geochemical data from the Coromandel Volcanic Zone (Booden et al., 2012), Kiwitahi (Booden et al., 2010), Ruapehu (Price et al., 2012), Alexandra (Briggs, 1986a; Briggs & Goles, 1984) and Taranaki (Price et al., 1999) volcanic centres and the Okete intra-plate volcanics of the western North Island (Briggs & McDonough, 1990). Due to the unavailability of REE data for Waikeria, it is absent from this plot.

The second group includes the intraplate magmas of the Okete field which have a flatter and smoother La/Y slope and the third belongs to the Kiwitahi volcanics which have an overall trend similar to that of Ruapehu and Coromandel magmas, but are more enriched in both the light and heavy REEs with strong negative Ce and Eu anomalies.

The above trends are also evident with the Maungatautari lavas. The Kairangi olivine basalt is most consistent with average magmas from the Okete Volcanics, although with differences in element compositions. The bulk of the samples from Maungatautari reflect the REE patterns of Coromandel, Ruapehu and Taranaki except that the REE profile for Maungatautari displays a small positive spike for Nd, no discernible negative Eu anomaly and is more depleted in HREE. Finally, the hornblende andesite samples of ORE040, HF043 and HF044 display enrichment of both light and heavy REE with strong negative Ce and Eu anomalies and as such best reflect the average magma for Kiwitahi Volcanics, not the main Maungatautari edifice.

The same groupings are apparent within the primordial mantle-normalised multielement diagram (Figure 4.18). The Okete and Kairangi basalts show a generally smooth trend with little to no negative Nb anomaly. All other fields show

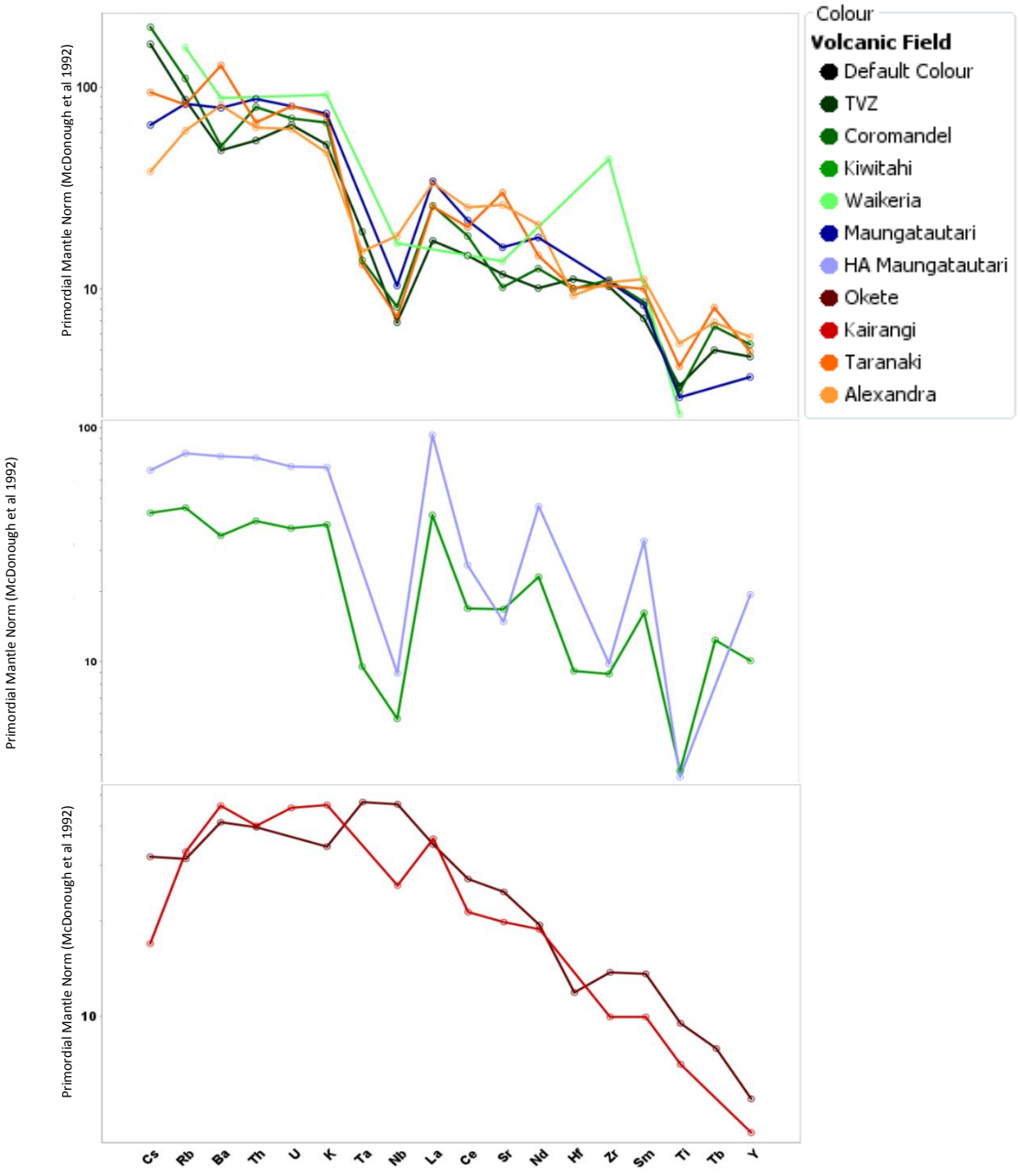

Figure 4.18. Trace element distribution diagrams normalized relative to primordial mantle composition of McDonough et al. (1992) for averaged geochemical data from the Coromandel Volcanic Zone (Booden et al., 2012), Kiwitahi (Booden et al., 2010), Ruapehu (Price et al., 2012), Alexandra (Briggs, 1986a; Briggs & Goles, 1984) and Taranaki (Price et al., 1999) volcanic centres and the Okete intra-plate volcanics of the western North Island (Briggs & McDonough, 1990).

a distinct decoupling between the LIL and HFS elements separated by strongly negative Nb anomalies. Maungatautari hornblende andesites and the Kiwitahi Volcanics particularly demonstrate enrichment in rare Earth and HFS elements of La, Nd, Sm and Y. In addition to the above groupings, magmas from the Taranaki and Alexandra volcanic centres begin to diverge from those from the Coromandel, Ruapehu and Maungatautari characterised by positive (rather than negative) Ba and Sr anomalies.

4.5.5 Sr and Nd Isotope Geochemistry

Strontium and neodymium isotope data for representative Maungatautari lavas are listed in Table 4.4 and isotopic variation for these elements is illustrated in Figure 4.19 where the data is compared with that available for Ruapehu andesites and basalts, Coromandel Volcanic Zone, Mt Taranaki, Alexandra Volcanics and the Okete Volcanic Group (Briggs & Goles, 1984; Briggs & McDonough, 1990; Huang *et al.*, 2000; Price *et al.*, 2012; Price *et al.*, 1999). Also shown on Figure 4.19, are average compositions for the Waipapa meta-sedimentary basement terrane (Price *et al.*, 2015) and MORB (Ito *et al.*, 1987). For comparative purposes, the Nd ratio values from (Briggs & Goles, 1984; Briggs & McDonough, 1990) were normalised to those of similar rock type measured at the same time as those in this study (O. Mcleod, personal communication, March, 2017).

Isotopic ratios for samples from across the main edifice (GF006, MRd020, ORE039b and ORE040), show little spread (Figure 4.19) and plot in a similar field to those of the Coromandel Volcanic Zone. The hornblende andesite and dacite (samples ORE040 and ORE039b respectively) have lower Nd and higher Sr ratios than the pyroxene and labradorite andesites and are displaced towards typical compositions of the Waipapa terrane metasedimentary basement rocks.

Table 4.4. Sr and Nd isotope geochemical data of representative samples collected using extraction chromatography and isotope ratio determinations by thermal ionization mass spectrometry (TIMS) at Victoria University, Wellington. PA = pyroxene andesite, LA = labradorite andesite, HA = hornblende andesite, HD = hornblende dacite and OB = olivine basalt.

Sample	**GF006**	**KSC001**	**MRD020**	**ORE039b**	**ORE040**
Rock type	*PA*	*OB*	*LA*	*HD*	*HA*
$^{87}Sr/^{86}Sr$	0.704478	0.703850	0.704555	0.704784	0.704645
2se	0.0000038	0.0000037	0.0000037	0.0000039	0.0000038
$^{143}Nd/^{144}Nd$	0.512810	0.512849	0.512807	0.512771	0.512775
2se	0.0000039	0.0000060	0.0000106	0.0000035	0.0000039

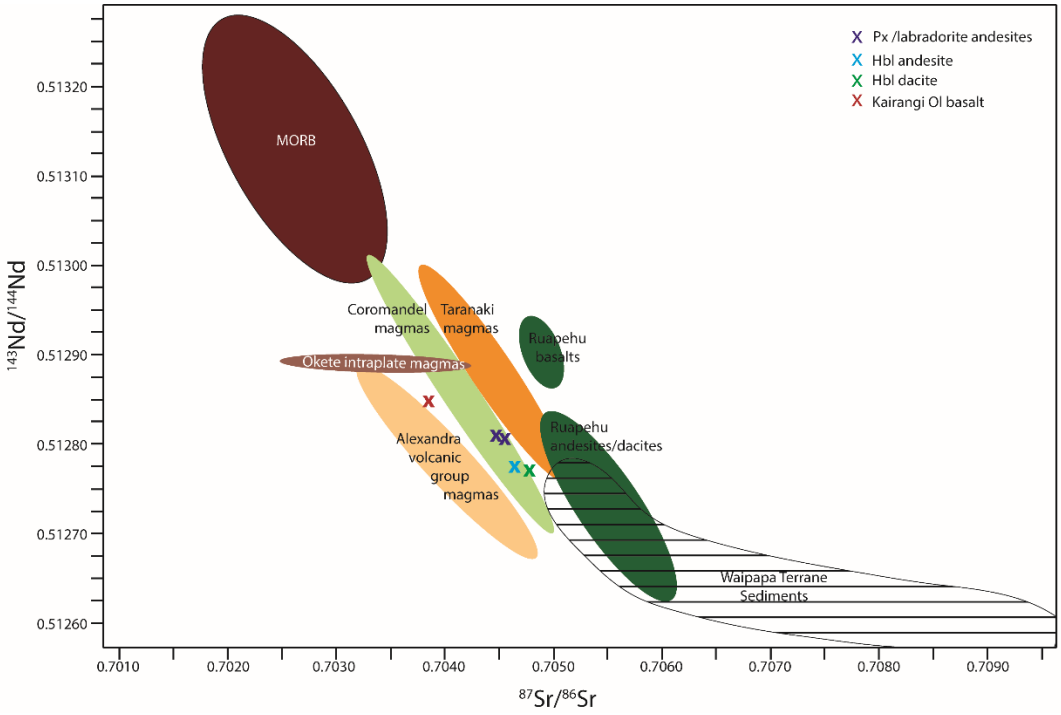

Figure 4.19. $^{143}Nd/^{144}Nd$ versus $^{87}Sr/^{86}Sr$ for Maungatautari lavas with comparisons with data from Ruapehu andesites and basalts (Price et al., 2012), Coromandel Volcanic Zone (Huang et al., 2000), Mt Taranaki (Price et al., 1999), Alexandra Volcanics (Briggs & McDonough, 1990) and the Okete Volcanic Group (Briggs & Goles, 1984). Data for the regional basement terrane (Price et al., 2015) and MORB lavas (Ito et al., 1987) are also included for reference. Sample numbers relating to the rock types analysed are stated in Table 4.4.

The olivine basalt from Kairangi plots apart from the other samples with significantly higher $^{143}Nd/^{144}Nd$ and lower $^{87}Sr/^{86}Sr$ at 0.512849 and 0.703850 respectively. These ratios overlap with samples from the Alexandra Volcanic Group and approach the intraplate magmas of the Okete field.

4.6 Discussion

This section discusses petrographic observations and petrogenesis of the lavas erupted within the field area, with emphasis on linking observations with processes which may have occurred prior to or during eruption, and interpretation of geochemical data. The regional context of Maungatautari is explored through comparison to averaged published data on the Coromandel Volcanic Zone, Kiwitahi, Ruapehu, Alexandra and Taranaki volcanic centres and the Okete intra-plate volcanics of the western North Island.

4.6.1 Petrography

The mineral composition of lavas from Maungatautari consists of plagioclase, two pyroxenes, hornblende and opaque minerals. All minerals occurring as phenocrysts were present within the groundmass, with the exception of hornblende and the addition of quartz in sample MSE056. Petrographic observations made during this study are consistent with those made by Briggs (1986b), who demonstrated that while the fractionation of these mineral phases from an olivine basalt parent (Kairangi) was not possible, some of the hornblende dacites may have resulted via fractionation of labradorite andesite.

Many samples display oscillatory zoning and sieve textures within larger plagioclase crystals indicating disequilibrium conditions during crystallisation. Oscillatory zoning reflects abrupt changes in magma composition and is most commonly explained by the periodic injection and mixing of more primitive melt within the magma chamber during the crystallisation of plagioclase (Haase *et al.*, 1980). This leads to the formation of concentric bands with varying brightness under cross-polarized light, each of which reflects small variations in chemical composition. Electron microprobe analyses by Briggs (1986b), highlighted the commonality of normal zoning in addition to oscillatory zoning, demonstrating that between injections of primitive melt, the magma chamber experienced periods of relative stability where plagioclase crystals were in equilibrium with the

melt that progressively became more Na-rich through time. The origin of sieve textures has been attributed to partial dissolution driven by chemical and thermal disequilibrium and/or dissolution driven by decompression (de Silva *et al.*, 2008; Maro & Caffe, 2016). At Maungatautari, sieve textures occur throughout an entire crystal or are concentrated within the centre of crystals surrounded by a non-sieved rim (Figure 4.2). Maro and Caffe (2016) attribute the diversity in resorption textures to variations in ascent rates and crystallisation depths where the earliest plagioclase phenocrysts formed at depth undergo partial dissolution due to re-equilibration after depressurization during ascent. Following this, plagioclase continues to crystalize forming an outer ring of non-sieved texture. Fully sieved crystals were likely erupted before equilibrium could re-establish, preserving pockets of glass within phenocrysts.

Hydrous mineral phases, such as hornblende, only occur as phenocrysts in evolved melts whose solidus temperatures are low enough to allow their formation at depth. As the melt ascends during eruptions, depressurisation reduces pH_2O preventing the formation of these mineral phases from occurring within the groundmass (Gill, 2010). The presence of hornblende in some andesites and the dacite lavas at Maungatautari is an indication of their hydrous nature. Decompression related dehydration is evidenced by rims of Fe-oxide and/or pyroxene or the complete replacement of the original crystal by tiny Fe-oxide, pyroxene and feldspar grains.

Xenoliths were common in some lavas. Those with mineral assemblages similar to the phenocrysts of the host lava were interpreted by Briggs (1986b) to be cognate xenoliths incorporated into the lavas as a result of disruption of cumulate layers at the bottom and sides of the magma chamber. While the igneous xenoliths observed within this study were consistent with Briggs (1986b) description of cognate xenoliths, some may in fact be accessory xenoliths incorporated from the sides of subsurface conduits along with fragments of crust during magma ascent to the surface.

4.6.2 Alteration Mineralogy

The presence of hydrothermally altered rocks located within in the headwaters of the Mangakara Stream (Locality 9, Figure 3.6) indicates that there was once an active hydrothermal system occurring around the summit region of Maungatautari. Large volcanic-hydrothermal systems are common on the flanks of active volcanoes such as White Island (Hedenquist, 1995) and Tongariro (Simpson & Bignall, 2016). Those located on the steep upper flanks at the vicinity of the summit are typically characterised by highly acidic fumaroles and/or hotsprings (Simmons *et al.*, 2005). Volatiles degassing from deep underlying boiling magmatic fluids, ascend and condense into the meteoric waters of the water table, creating acidic waters which cause severe leaching and advanced argillic alteration. This style of low-sulfidation hydrothermal alteration has a characteristic mineral assemblage of cristobalite, alunite and kaolinite comparable to that identified in the XRD diffraction pattern for sample MSE014 (Figure 4.9) (Hedenquist, 1995; Simmons *et al.*, 2005). The intense degree of leaching and brecciation of sample MSE014 strongly suggests fluid flow (Figure 4.8) and implies that the system in this area of Maungatautari included hot springs (Figure 4.20) similar to the Ketetahi hot springs on the upper flanks of Mt Tongariro. Typically away from the core, intense argillic alteration passes outwards into an outer zone of propylitic alteration as the acidic water is progressively neutralised by the host rock (White & Hedenquist, 1995). Albite is a common mineral associated with this alteration style and explains the uncharacteristic presence of albite in sample MSE011, located approximately 5-10 m away. This alteration typically occurs at the depth of the water table which suggests that current topography of this area has experienced considerably less erosion than originally thought. This location is also on the southern side of ridge E1 (Figure 3.2) which is thought to represent the scarp of a failed large rock avalanche event in which the hydrothermal alteration of rocks to clay minerals of low yield strength is a primary factor relating to flank instability.

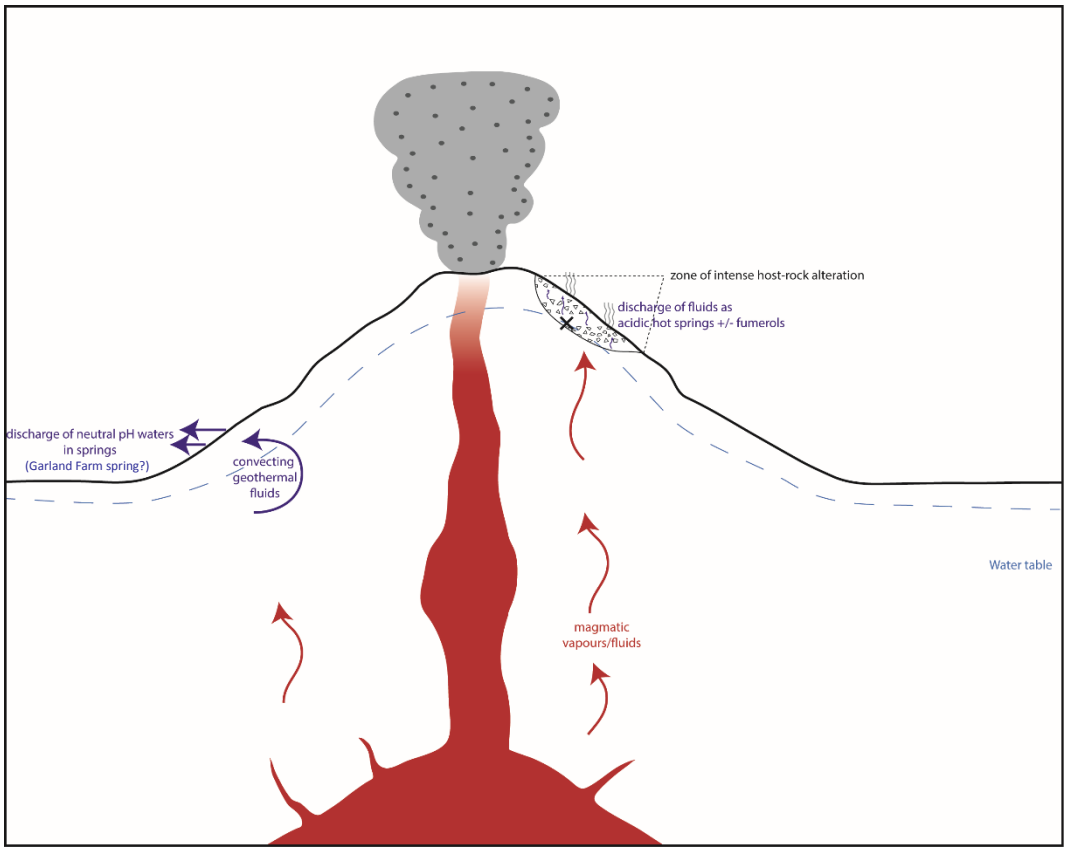

*Figure 4.20. Schematic diagram of possible hydrothermal system at Maungatautari. Magmatic vapours rise through the edifice and condense in the meteoric waters of the water table producing acidic hot springs and/or fumaroles where the host andesites undergo advanced argillic alteration like those observed at the gold workings site (marked by **X**). Neutral pH fluids may have been discharged at the base of the volcano (Garland farm spring) due to strong hydraulic gradients.*

In contrast to the intense acidic alteration which occurs on the upper slopes of volcanoes, the strong hydraulic gradients associated with stratovolcanoes cause pH neutral fluids to be discharged in areas of lower relief, potentially far from the active volcanic vents (Simmons *et al.*, 2005). Such a spring may have been located in what is now a tributary to the Mangapiko Stream (sample GF005; Locality 3, Figure 3.6). The presence of opal and adularia in the diffraction patterns of sample GF005 are typical minerals which characterise the discharge of such fluids and the localised presence of sinter, although this is currently speculative and requires further investigation beyond the scope of this study to confirm this.

The indicative minerology from the diffraction patterns from samples from the trig (MSE062 and MSE063) were consistent with petrographic observations. The presence of cristobalite may reflect the devitrification of volcanic glass or mild

hydrothermal alteration indicated by hand specimen textures and the associated presence of albite, however, with the lack of in situ outcrop, specific processes which occurred at this site remain uncertain.

4.6.3 Geochemistry

Lava composition at Maungatautari ranges from basalt (at Kairangi) to med-high K andesites and dacites (Figure 4.10 and Figure 4.11). The smooth trend of Figure 4.10 along with progressive increases in Na_2O and K_2O, and concomitant decreases in MgO, Fe_2O_3, CaO, TiO_2 with increasing SiO_2 (Figure 4.13) implies, at least qualitatively, that the evolution of Maungatautari lavas was dominated by the fractional crystallisation of a parent magma. Compatible trends within the trace elements Sc and Sr relate to the crystallisation of pyroxenes and the substitution for Ca in plagioclase respectively. Low concentrations of Ni (5-25 ppm) are also consistent with andesites derived via fractional crystallisation (Winter, 2014). However, fractionation modelling by Briggs (1986b) highlights that magma petrogenesis at Maungatautari and its subsequent evolution is likely to be complex and excluded the possibility of the Kairangi olivine basalt from being the primary magma for Maungatautari. In Figure 4.10, the basalts sit above the general trend and plot as alkali basalts using the Nb/Y classification diagram of Winchester and Floyd (1977) (Figure 4.12). Three low-SiO2 hornblende andesites also sit outside the main cluster to the left of the diagram in Figure 4.12, suggesting that these rock types are not petrogenetically related to the fractionating andesite and dacites of the main system.

Primitive magmas are considered to have Mg# of >60 and while primitive basalts are found in a variety of plate tectonic settings, primitive andesites are only rarely found outside of continental arcs (Kelemen *et al.*, 2013). With Mg numbers of between 30 and 49, Maungatautari lavas are not primitive, nor can they be classified as high-Mg# andesites and as such are considered here to be evolved magmas following Kelemen *et al.* (2013), who uses the assumption that crystallization processes always produce a lower Mg# in derivative liquids, when

compared with parental liquids. No basalts have been found at Maungatautari so the basaltic composition of any potential basaltic parental melt remains unknown, however the possibility that lavas are derived from a primitive andesite has not been excluded either as these magmas are more commonly emplaced as plutonic rocks in the middle and upper crust and may never be erupted at the surface (Kelemen, 1995). Eleven samples have Mg# of between >46-49 and these are considered to represent least evolved magmas which consist of pyroxene andesites and three samples of hornblende andesite. The hypothesis that these pyroxene andesites represent least evolved magmas is supported by the fractionation models of Briggs (1986b) which produced acceptable fits for the fractionation of a labradorite andesite from a pyroxene andesite parent melt. The high Mg# of these rocks may therefore reflect the lack of olivine crystallisation from a primitive andesitic melt, or simply be the product of abundant phenocrysts of clinopyroxene (Kelemen *et al.*, 2013). As neither clinopyroxene or olivine were present within the hornblende andesites, these mineral phases are not contributing to the high Mg# of these samples in any way.

Rare Earth and trace element geochemistry

The decoupled LIL/HFS pattern and Ta-Nb trough in the mantle-normalised multielement diagram (Figure 4.16), is a distinctive feature of subduction zone magmas. This decoupling between the two elemental groups and LIL enrichment reflects the participation of water-rich fluids in the genesis of subduction zone magmas (Winter, 2014). The origin of Ta-Nb depletion relative to the other incompatible elements has been attributed to numerous processes (Bodinier *et al.*, 1996; Kelemen *et al.*, 1993; Plank, 2005). Kelemen *et al.* (2013) suggests that the most likely cause is the fractionation of Ta and Nb from other highly incompatible elements via the partial melting of subducting eclogite and/or sediment with residual rutile. A slight negative Eu anomaly amongst the hornblende and labradorite andesites and dacites reflects plagioclase fractionation and is consistent with the concept that pyroxene andesites are representative of least evolved melts at Maungatautari from which such an

anomaly it is absent. The presence of a deep (> 70 km) garnet-bearing source rock is suggested by the depletion of HREE and Y (Figure 4.15) in which they are strongly compatible and retained at the expense of the melt (Gill, 2010; Winter, 2014).

Within the general trace element patterns for Maungatautari, two distinct variations are evident. Kairangi olivine basalts are less enriched in LIL elements and a less pronounced negative Nb anomaly which produces a smoother pattern more reflective of intraplate over subduction-related melts (Winter, 2014). The negative slope of the REEs in Figure 4.15 results from LREE enrichment and represents an enriched mantle source for this melt. The low-SiO_2 hornblende andesites have LIL element concentrations consistent with other samples from the main Maungatautari edifice, but are more enriched in the heavy REE and particularly Y which is also highly evident in Figure 4.15 and reflective of a relatively shallow, non-garnet bearing source rock. Negative Ce anomalies have been attributed to the recycling of sediments and seawater-altered basalts into the upper mantle (Neal & Taylor, 1989).

The above interpretation therefore suggests that Maungatautari lavas are derived from at least three distinct mantle-melt sources which are summarised in Figure 4.21. Most Maungatautari andesites and dacites are petrogenetically related and are associated with dominant fractionation of andesites to dacites from subduction-related, deep, garnet-bearing, depleted mantle source rock. The low SiO_2 hornblende andesites, however, are derived from a shallower upper mantle (garnet-free) source rock while the Kairangi olivine basalt is an intraplate magma similar to those of the nearby Okete Field which originates from an area of enriched mantle.

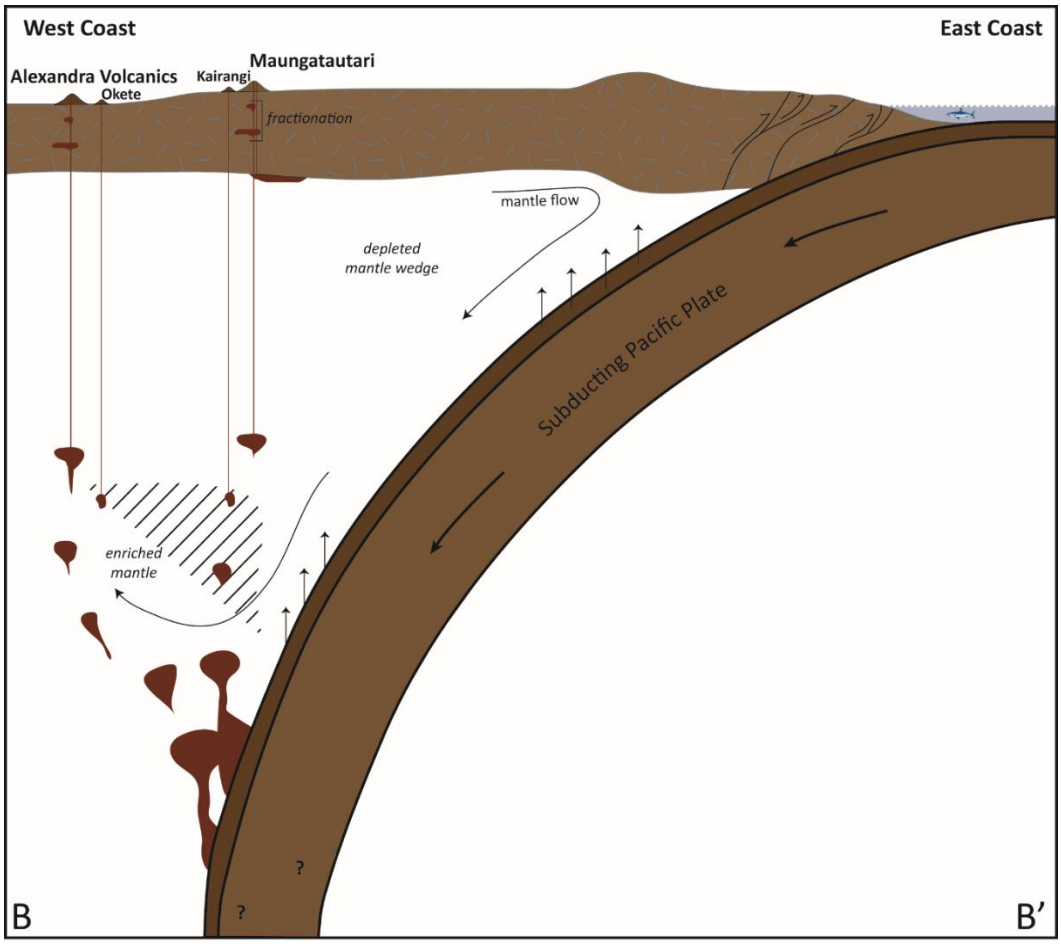

Figure 4.21. Schematic cross section demonstrating the petrogenesis of magmas at Maungatautari, adapted from (Briggs et al., 2013). Location of cross section line is shown in Figure 4.22.

Sr and Nd isotope geochemistry

As isotopes do not fractionate during partial melting or fractional crystallization processes they have come to be viewed as useful indicators of source variations (Winter, 2014). However, it is becoming increasing clear that magmas of continental arcs typically have complex histories involving periodic storage in multiple magma chambers at various depths, magma mixing and crustal contamination which all occur simultaneously with ongoing fractional crystallisation processes. As such, multi-element isotopic data is required to determine how the various components of the subduction system, e.g. slab, fluids, sediments and mantle wedge, interact with parental magmas prior to ascent and subsequent interaction with the lithosphere (Waight *et al.*, 2017).

This study presents the first Sr and Nd isotope data for Maungatautari lavas. While the dataset is limited, it identifies source variations between the different rock types analysed. Three samples (GF006, MRd020 and ORE039b) plot on Figure 4.19 in a way which is consistent with major and trace element geochemical data of a fractionating system with a consistent petrogenetic relationship. The more radiogenic Sr values of the hornblende dacite from Oreipunga Cone (ORE039b) is likely reflective of the assimilation of crustal material during storage and ascent (Winter, 2014). The isotopic ratios of the hornblende andesite (sample ORE040) are also indicative of crustal assimilation, however, the less evolved (low-SiO_2, relatively high Mg#, Figure 4.13) nature of this magma implies a significant lithospheric contribution towards it genesis. The Sr and Nd isotope data presented here does not discriminate between crustal assimilation from the overriding plate and source addition derived from the sediments added to the mantle wedge via the subducting slab (Waight *et al.*, 2017).

The olivine basalt from Kairangi (KSC001) plots apart from the other samples with significantly higher radiogenic Nd and relatively non-radiogenic Sr (Table 4.4; Figure 4.19) which overlaps with samples from the Alexandra Volcanic Group and approaches the intraplate magmas of the Okete field. The limited dataset for the Okete field form a very tight group which fall within the broader isotopic composition ($^{87}Sr/^{86}Sr$ 0.7027-0.7050; $^{143}Nd/^{144}Nd$ 0.5128-0.5131) of intraplate volcanic rocks from throughout Zealandia (Timm *et al.*, 2010). The isotopic ratios of 0.512849 and 0.703850 for Nd and Sr, respectively, are therefore consistent with Figure 4.15 which indicates a relatively deep, yet enriched magma source within the mantle wedge reflective of intraplate rather than a subduction-related melt and is therefore, with the exception of geographical location, not related to magmatism at the Maungatautari edifice.

New perspectives on Maungatautari Volcanism

Currently, Maungatautari is considered as a subduction-related volcano situated behind the volcanic front active approximately 1.8 Ma (Briggs, 1986b). However,

the trace and rare earth element geochemical data presented in this study have provided new insight into the relationship between Maungatautari and the other volcanic centres active c. 2 Ma.

The main fractionating system that produced magmas at Maungatautari have multi-element and REE patterns that bear a striking resemblance to those from the Coromandel Volcanic Zone and Ruapehu (Figure 4.18). The same pattern is also seen within the Alexandra and Taranaki magmas with positive anomalies in Ba and Sr being attributed to crustal level processes influencing subduction magma genesis set behind the volcanic arc front (Price *et al.*, 2016). With negative Ba and Sr anomalies, Maungatautari multi-element and REE patterns best reflect those from Coromandel Volcanic Zone and Ruapehu and are therefore interpreted to represent volcanism associated with the main volcanic arc which extended south from Tauranga to Maungatautari into continental New Zealand during this time (Figure 4.22). This interpretation is consistent with Giba *et al.* (2010) and Seebeck *et al.* (2014) who include the North Taranaki Graben volcanoes as part of a single volcanic arc propagating through the North Island. Geochemical data for the dacitic magma intrusion found within a drill hole at Waikeria is limited, yet displays a clear subduction related signature with negative Ba and Sr anomalies consistent with other volcanoes forming the volcanic arc front (Figure 4.18). The strong positive Zr anomaly is assumed to relate to significant crustal assimilation and/or magma fractionation and as such, within this model, Waikeria is inferred to represent the southernmost expression of arc-related magmatism within the North Island of New Zealand at this time.

The near-by Alexandra Volcanics consisted of contemporaneous, behind-arc subduction-related volcanism, the nature of which was first proposed by (Briggs *et al.*, 2013) (Figure 4.22). The alkali olivine basalt at Kairangi displays a distinct intraplate signature and is therefore unrelated to magmatism at Maungatautari although the exact temporal relationship between the two magmatic series remains uncertain as the date range for Maungatautari volcanism remains poorly constrained. The coeval occurrence of intraplate alkali basalts alongside

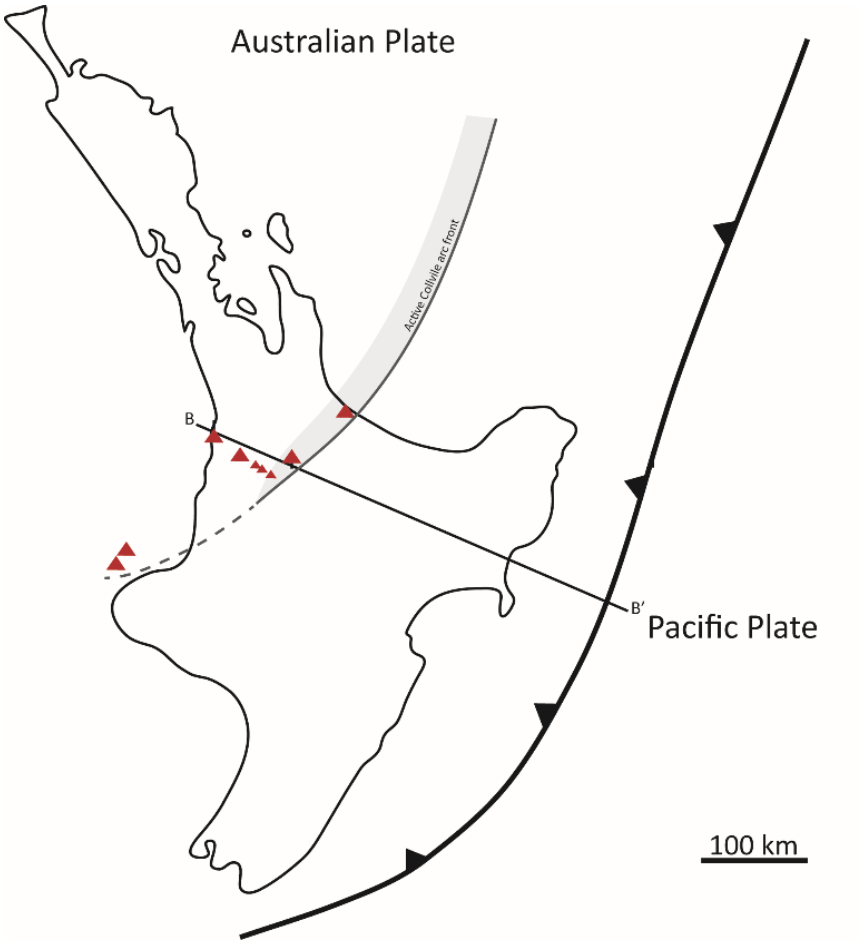

Figure 4.22. Schematic map showing the estimated position of the Colville volcanic arc at c. 2 Ma and its propagation through the western North Island to include Maungatautari and Waikeria. Active volcanic centres are shown by red triangles. The continuation of the arc to include the western Taranaki Graben Volcanoes (dashed line) remains speculative.

subduction-related magmas is well documented within the nearby Alexandra and Okete volcanic groups (Briggs *et al.*, 1989; Briggs & McDonough, 1990), although the mechanisms which result in the occurrence of two contrasting magma series within a clearly convergent tectonic setting remains uncertain.

Chapter Five:

Physical Volcanology of Two Pyroclastic Successions

5.1 Introduction

This chapter describes the location, field and facies characteristics, and componentry of Maungatautari pyroclastic deposits which are then interpreted to highlight some of the explosive eruption styles and eruptive processes associated with the volcano.

The construction of the 'over-the-mountain' public walking track has exposed outcrop in areas of the mountain which have never been studied, many of which include pyroclastic deposits. Excavations located at 3.4 km north of the southern end of this track and, further along, near the summit (Figure 5.1) have uncovered two successions referred to as Quarry #34 and the Summit Quarry respectively. The successions were divided into stratigraphical units each reflecting a distinct identifiable depositional layer with clear textural or compositional boundaries

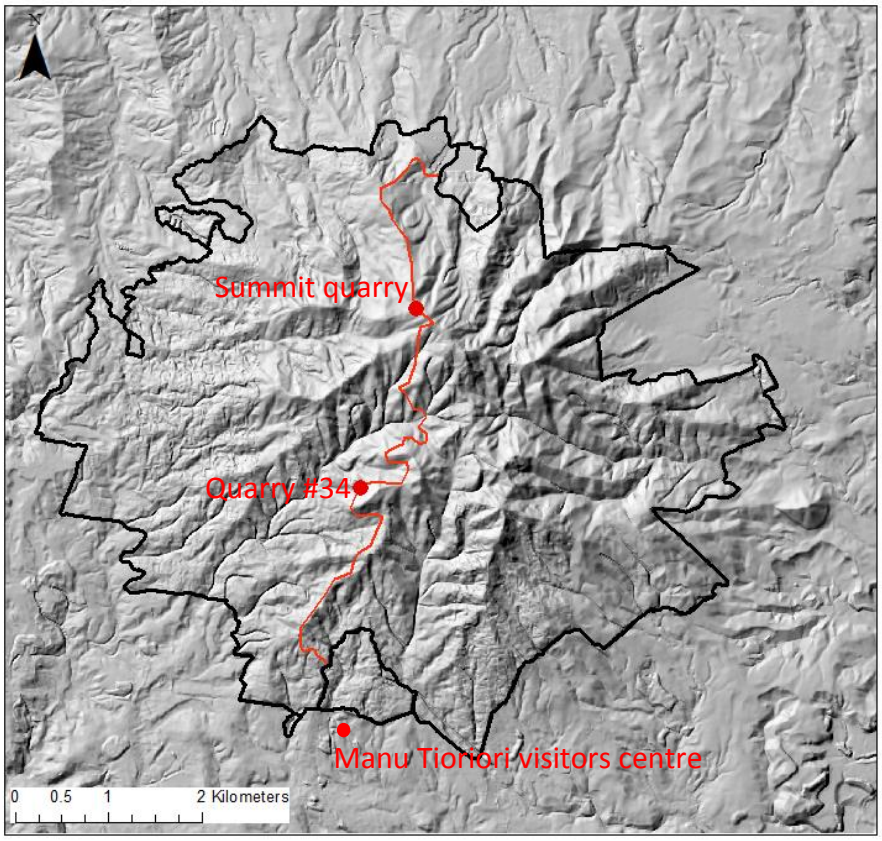

Figure 5.1. Map showing the location of the two pyroclastic successions described at Quarry #34 and Summit Quarry.

separating the top and bottom of the unit and grouped into facies. The description and interpretation of these facies along with the petrography of components form the basis of this chapter.

Numerous other deposits with relict volcaniclastic textures were also observed elsewhere along the track, however significant weathering and the regrowth of vegetation has significantly masked the details of these successions. Due to the limited number of outcrops and exposure, no stratigraphical relationships between any of the sites are inferred or suggested and each described section is treated as an individual window into volcanic activity which occurred during unspecified eruptive events.

5.2 Methods

Analysis of the pyroclastic successions was undertaken using a combination of field work and petrographical techniques.

Field work consisted of the construction of stratigraphic logs and descriptions of the geometry and lithology of individual units – including their componentry, texture, structures (if present) and the contact relationships. Samples were collected from each stratigraphical horizon and included both bulk samples and those of the various clast types.

Petrographical analysis involved optical microscopy of thin sections. Twenty-six samples representative of stratigraphical and facies changes throughout the succession were prepared as described in Section 4.2.1. These were examined using a petrographic microscope in both plane and cross polarised light to identify and describe the different minerals, components and textures.

5.3 Quarry #34 succession

The most detailed pyroclastic succession is exposed within a small quarry, 3.4 km along the walking track, north of the Manu Tioriori Visitor Centre located near the

entrance to the Southern Enclosure (Figure 5.1). The outcrop is at an elevation of 613 m above sea level with a north-west aspect, and is located on a steep slope which descends into the Mangaohoi Stream (Figure 3.6).

5.3.1 Site description

The excavation at quarry #34 measures approximately 6 m wide by 8 m high (locality 19, Figure 3.6; Figure 5.2). The pyroclastic succession exposed encompasses the entire width of the quarry and extends for at least 2 m to the left-hand side of Figure 5.2. The maximum vertical thickness of the exposed pyroclastic succession is 5.2 m which decreases in height to ground level across the face of the exposure (left to right in Figure 5.2) where it grades into the general slope at the level of the track. The succession is overlain by a further ~2.5 m of reworked colluvium and well-developed organic-rich soil to give a total stratigraphical thickness of ~8 m. The average dip of the individual stratigraphical units is 13^{o} to the west.

Figure 5.2. Outcrop at quarry #34 consisting of up to 5.2 m of pyroclastic deposits overlain by ~2.5 m of reworked colluvium and well-developed organic-rich soil. The total vertical thickness of the outcrop measures ~8 m.

5.3.2 Facies Characteristics and Stratigraphy

The stratigraphic variation throughout the pyroclastic succession at quarry #34 is shown in Figure 5.3. Nine stratigraphical units, QT1-QT9, were identified and three facies have been defined based on textural differences and general physical appearance which are described below.

FACIES A – Massive, moderately-poorly sorted, fine to coarse lapilli tuff

Facies A is characterised by massive, moderately to poorly sorted fine to coarse lapilli tuff (Figure 5.4) and comprises more than half of the stratigraphic thickness of the Quarry #34 succession and the entire thickness of units QT1, QT3, QT5 and QT8 (Figure 5.3). In Unit QT1, facies A was exposed from ground level to a height of 60 cm and consists of massive, moderately sorted, non-graded, speckled yellow-white and grey medium-coarse lapilli tuff. Within Unit QT3, this facies is 2.6 m thick and consists of coarse lapilli tuff and 3-5 % blocks which have an average maximum size of 136 mm. The unit then grades normally through the upper 1 m into medium lapilli tuff. Facies A also occurs in units QT5 and QT8, each 0.2 m thick, but finer-grained, consisting of medium and fine lapilli tuff.

Juvenile material consisted of vesicular and non-vesicular, hornblende-rich clasts which ranged in size from 2-3 cm to 20 cm in diameter. Lithics included angular fragments of greywacke and fresh and weathered and/or altered andesite-dacite lavas, many with small (> 1 cm) inclusions of clasts of a similar lithology and/or greywacke. The largest clasts occur in facies A within the lower half of unit QT3, 1-2 m above ground level.

FACIES B – Laminated-bedded crystal and lithic-rich coarse tuff and very-fine lapilli

Facies B consists of laminated (< 1 cm in thickness) to very-thinly bedded (1-2 cm), crystal- and lithic-rich coarse tuff and very-fine lapilli (Figure 5.4) which

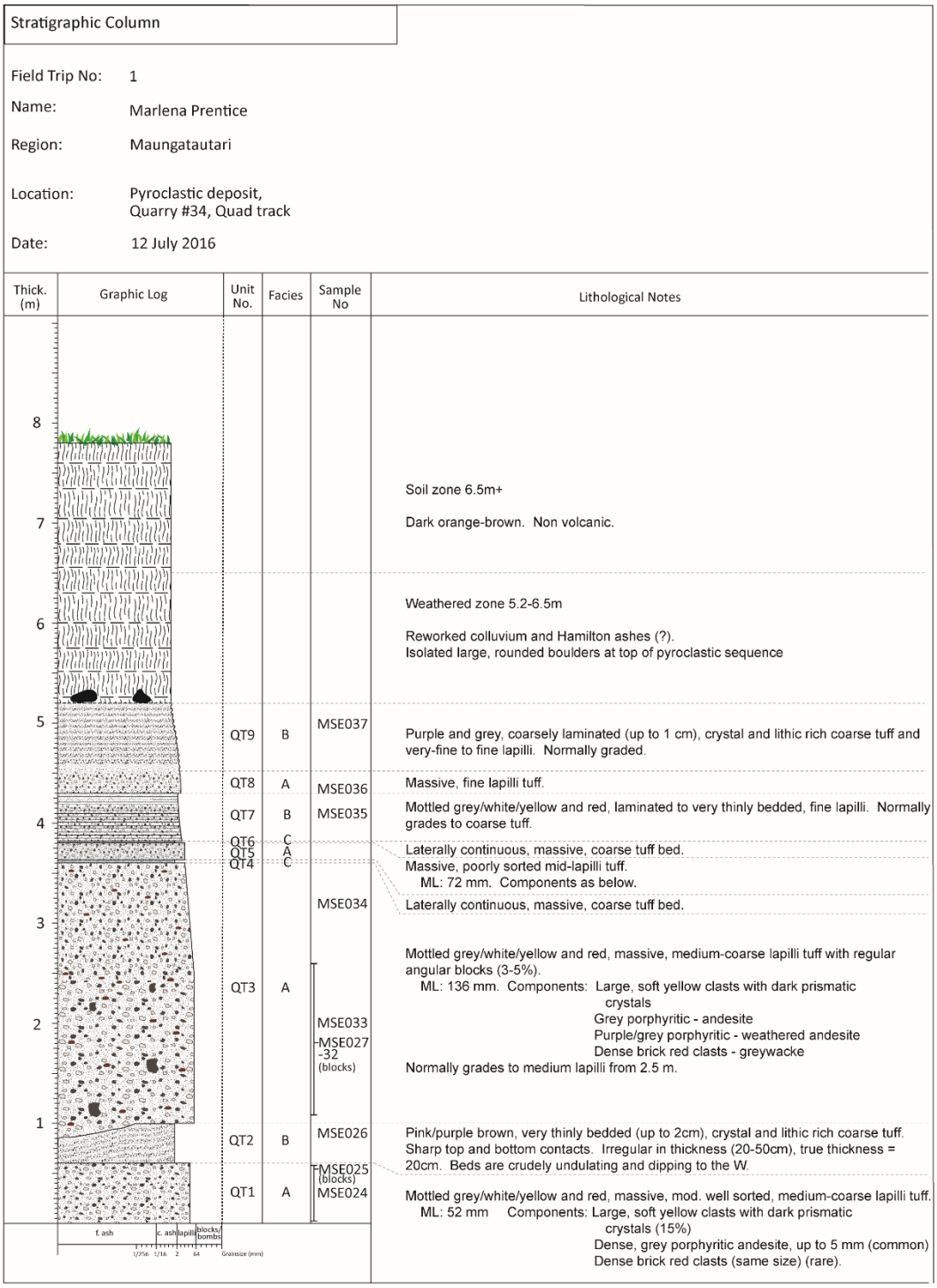

Figure 5.3. Facies and stratigraphy of the pyroclastic succession at quarry #34 (locality 19, Figure 3.6). Sample numbers MSE024, MSE026 and MSE034-037 represent bulk-rock samples are placed at the corresponding height they were obtained. Samples MSE025 and MSE027-033 are representative block-sized clasts collected over the thickness intervals shown by vertical bars. ML = maximum lithic size, and represents the average of the long axis length of 5 largest clasts. Percentages are visual field estimates.

Figure 5.4. Facies A, B and C in outcrop at quarry #34 where the massive lapilli tuff of facies A contrasts with the laminated-bedded crystal and lithic-rich coarse tuff and very-fine lapilli of facies B. The thin tuff beds of facies C form two thin and laterally continuous bands across the outcrop.

comprises three stratigraphic units: unit QT2, 0.4 m thick; unit QT7, 0.35 m thick; and unit QT9, 0.7 m thick.

Horizontal stratification of facies B within Unit QT2 formed very thin beds up to 2 cm thick. The maximum thickness of this unit was 0.4 m, however, the upper contact was undulating which caused the thickness of this unit to be irregular across the exposure ranging from 0.2 m to 0.4 m. The internal stratification of facies B within units QT7 and QT9 was thinner, forming alternating coarse laminations rather than thin beds of coarse tuff and fine lapilli and both units displayed normal grading.

FACIES C – Massive coarse tuff

The two very thin beds (units QT4 and QT6) of facies C, were characterised as laterally continuous, red-coloured, massive, well sorted coarse tuff and are the thinnest units within the succession (Figure 5.4). Unit QT4 occurred at 3.6 m above ground level with unit QT6 following at 3.8 m and are 0.03 m and 0.015 m thick, respectively.

Facies Architecture at Quarry #34

The pyroclastic succession at quarry #34 has been divided into nine stratigraphical units and grouped into three distinct facies (Figure 5.3). Unit QT1, is the lowest stratigraphical interval and is composed of facies A which is exposed from ground level to a height of 60 cm. Overlying this, is unit QT2 which is comprised of facies B. The upper and lower contacts of unit QT2 with units QT1 and QT3, respectively, were sharp and planar, however the upper contact was undulating causing the thickness of this unit to be irregular across the exposure ranging from 0.2 m to 0.4 m. Unit QT3 is the thickest unit of the succession and is comprised of facies A which is massive in the lower 1.5 m and normally graded over the upper 1 m to produce a thick bed with a total thickness of 2.6 m. Directly overlying this is a thin bed (0.03 m) of facies C (unit QT4), then a medium bed of facies A (0.2 m thick, unit QT5), then returning to a thinner bed of facies C (unit QT6). The upper part of the succession alternates between facies B (0.35 m thick, unit QT7), facies A (0.3 m thick, unit QT8), and facies B again (0.7 m thick, unit QT9). While contacts between the units are typically sharp and planar throughout the succession, the upper contact of unit QT8 is gradational. Isolated large rounded boulders along with numerous smaller sub-rounded to rounded andesitic clasts sit directly on top of unit QT9, however, no deformation of the bedding structures was observed and they lay contained within a weathered zone of reworked colluvium.

5.4 Summit Quarry Succession

The second pyroclastic succession was also located along the walking track, approximately 100 m north of stairs that lead up to the Maungatautari trig (locality #30, Figure 3.6; Figure 5.1). The outcrop has a westerly aspect and at an elevation of 774 m above sea level, it is the highest point along this track before descending along the main northern ridge to the track entrance by the northern enclosure.

5.4.1 Site description

The excavation at the summit quarry measures approximately 10 m wide by 3.6 m high (Figure 5.5). The pyroclastic succession exposed encompasses the entire width of the quarry, has a maximum vertical thickness of 2.8 m and is overlain by 0.3 m of clay-rich soil and 0.5 m of well-developed dark brown-black organic-rich soil. With an apparent dip to the northwest, this outcrop gradually decreases in height to ground level across the face of the exposure (left to right in Figure 5.5) grading into the general slope at track level.

Figure 5.5. Succession exposed at the summit quarry. The height of the tape measuring on the left is 3.6.m.

5.4.2 Facies Characteristics and Stratigraphy

The stratigraphic variation throughout the summit quarry succession is shown in Figure 5.6 which has been divided into three stratigraphical units (SQ1, SQ2 and SQ3) based on textural differences and general physical appearance. Facies types includes the massive, poorly sorted fine to coarse lapilli tuff of Facies A, along with two others (Facies D and E) which are described below in stratigraphic order (i.e. SQ1, Facies D; SQ2, Facies A; SQ3, Facies E).

FACIES D – Poorly sorted, non-welded massive lapilli tuff

The lower 0.5 m of the succession at the summit quarry (unit SQ1) consists of a red-coloured, matrix-supported, poorly sorted, non-welded massive lapilli tuff with 5-7% angular blocks up to 211 mm in size (Figure 5.7). This facies is distinguished from the massive lapilli tuff of facies A by a significantly higher proportion of ash matrix, estimated in the field to be 60-70%. The maximum thickness of this unit is unknown as the basal contact is not exposed. The upper contact with the overlying unit (SQ2) of Facies A is gradational and undulating across the outcrop.

Lithic clasts consist of angular, non-vesicular, hornblende-rich fragments of fresh and weathered and/or altered andesite-dacite lavas. Extensively weathered, sub-rounded clasts of similar composition to the juvenile material in quarry #34 were also observed. Lithics of sedimentary lithologies were not observed.

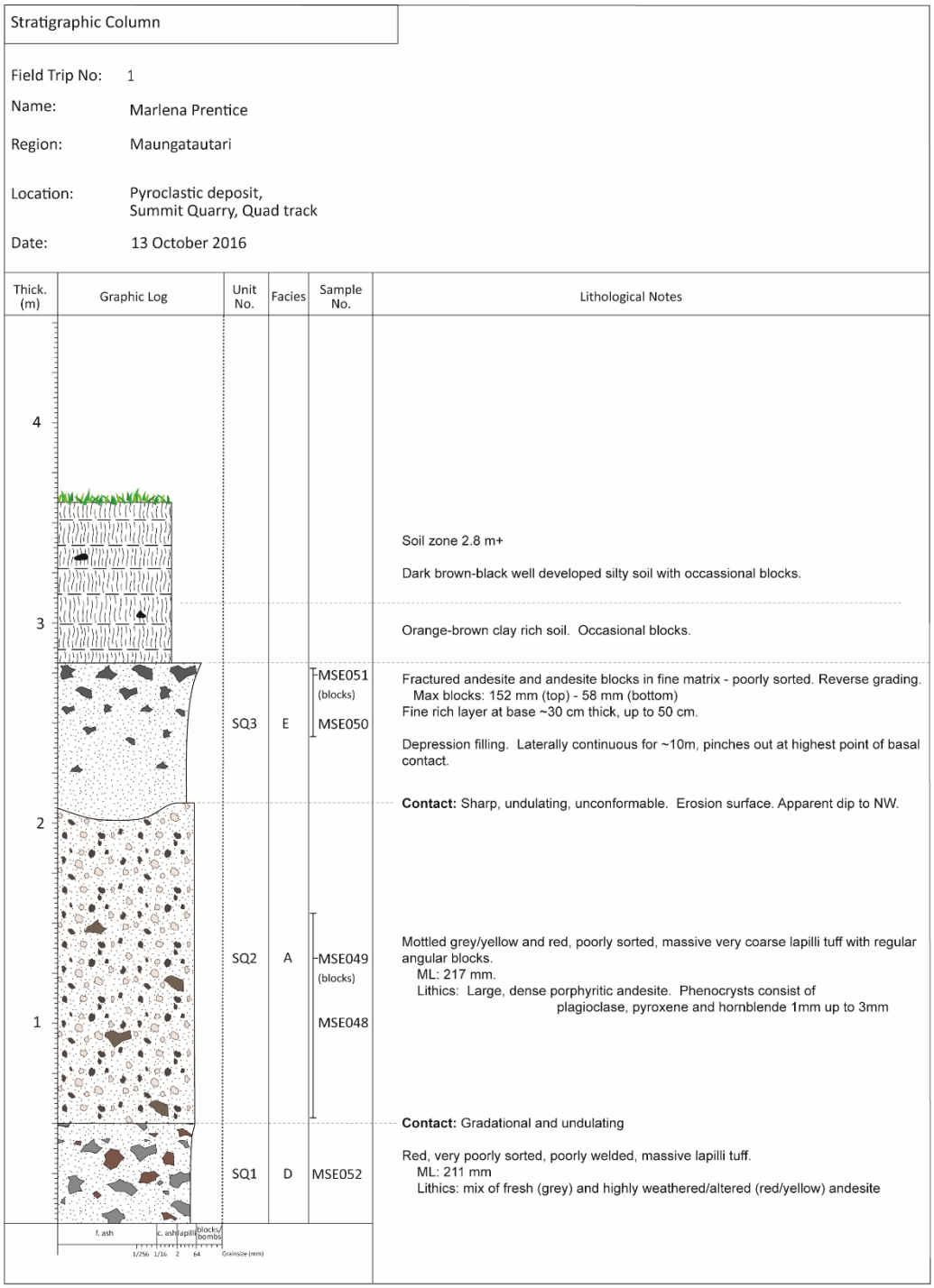

Figure 5.6. Facies and stratigraphy of the succession at the summit quarry (locality 30, Figure 3.6). Sample numbers MSE048, MSE050 and MSE052 represent bulk-rock samples and are placed at the corresponding height they were obtained. Samples MSE051 and MSE051 are representative block-sized clasts collected over the thickness intervals shown by vertical bars. ML and percentages as defined in Figure 5.3.

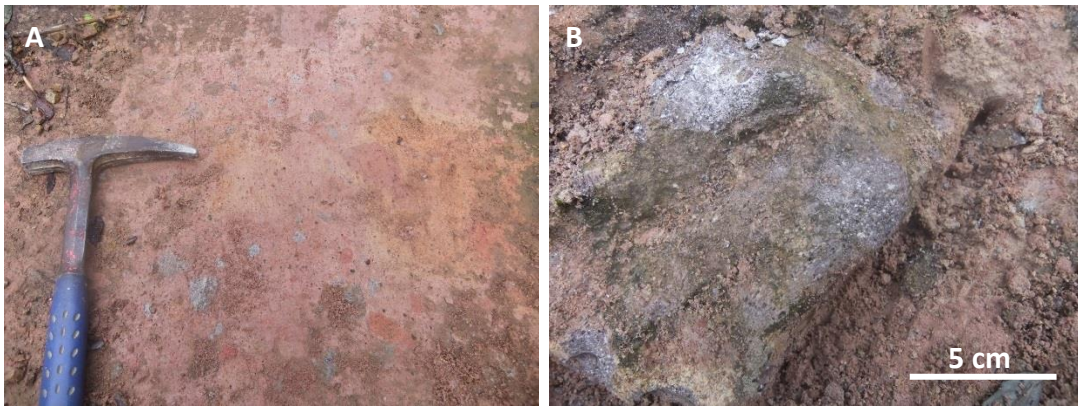

Figure 5.7. Facies D in outcrop at the summit quarry displaying: A) red-coloured, matrix-supported, poorly sorted, non-welded massive lapilli tuff, and B) an andesitic angular block.

FACIES A – Massive, moderately-poorly sorted, fine to coarse lapilli tuff

Unit SQ2 is ~1.5 m thick and is comprised entirely of facies A (Figure 5.8), which was described previously in section 5.3.2 for quarry #34 and encompasses the greatest thickness within the summit quarry pyroclastic succession (Figure 5.6). It consists of massive, mottled grey, red and yellow-coloured, poorly sorted coarse-grained lapilli tuff with an average clast size of 35 - 50 mm. Abundant angular blocks of dense porphyritic andesitic-dacitic lava with an average maximum size of 217 mm are distributed throughout.

Figure 5.8. Facies A within unit SQ2 at the summit quarry.

Juvenile material consisted of vesicular and non-vesicular, hornblende-rich clasts. Lithics included angular fragments of fresh and weathered and/or altered andesite-dacite lavas and no lithics of sedimentary lithologies were observed. The upper contact with the overlying unit of facies E is sharp and broadly undulating.

FACIES E – Reversely graded blocks within a massive and poorly sorted silt-sand-pebble matrix

The upper stratigraphic interval at the summit quarry (unit SQ3), consists of reversely graded blocks of non-vesicular, porphyritic hornblende-rich andesitic-dacitic lavas within a massive and poorly sorted (silt-pebble sized) matrix (Figure 5.9).

The lack of juvenile clasts, matrix texture and the distinct fines-rich base all distinguish this facies from those previously described. The lensoidal geometry of this unit is also apparent in Figure 5.5 where it is thickest (~1.5 m) within the centre of the outcrop and thins outwards.

Figure 5.9. Facies E of unit SQ3 within the summit quarry showing reverse grading of blocks and fines-rich basal layer marked near the base of the photo by the top of the scraper which is used for scale.

5.5 Petrography and componentry of lapilli- and block-sized clasts

The major components of the eruptive deposits described at quarry #34 and the summit quarry are characterized by lapilli to block sized pyroclasts containing a mixture of crystal-rich, vesicular and non-vesicular juvenile clasts, dense lithics of angular fresh, weathered and/or hydrothermally-altered andesite-dacite lava and within units QT1 and QT3 at quarry #34, sub-rounded fragments of poorly sorted fine-grained sandstones. Clasts are predominately contained within a non-welded, crystal- and lithic-rich coarse tuff matrix, except for facies E which is poorly sorted and coarser. Each clast type is described in turn below and based on representative samples of clasts extracted from facies A and D between 1 and 2 m at quarry #34 (Figure 5.3) and up to 2 m at the summit quarry (Figure 5.6).

5.5.1 Juvenile pyroclasts

Crystal-rich, vesicular (Figure 5.10) and non-vesicular (Figure 5.11) juvenile clasts ranging from 2-3 cm to 20 cm in diameter, were found within units of facies A at both study sites. In both types, the dominant phenocryst mineral phases consist

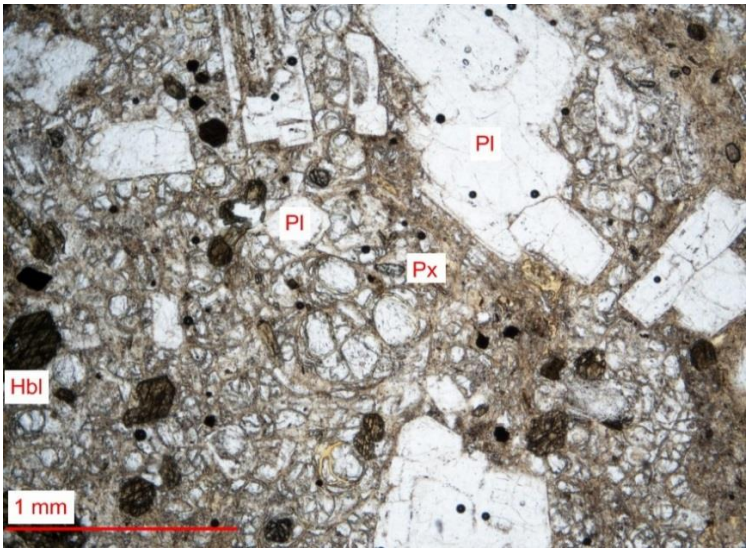

Figure 5.10. Photomicrograph of the finely vesicular crystal-rich juvenile clast of sample MSE027 (ppl). Pl = plagioclase, Px = pyroxene and Hbl = hornblende

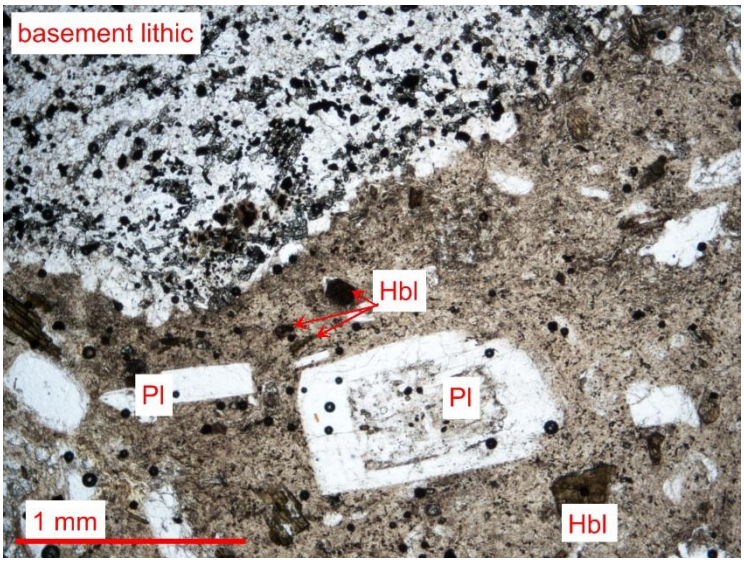

Figure 5.11. Photomicrograph under ppl of non-vesicular clast within the vesicular juvenile clast of sample MSE027. Note the large lithic of fine sandstone in the top left corner. Crystal abbreviations as per Figure 5.10.

of plagioclase, and hornblende with disseminated opaque minerals and rare pyroxenes.

Plagioclase crystals are predominately subhedral and range in size from < 1 mm up to ~2-2.5 mm. Many of the larger crystals exhibit sieve textures and oscillatory zoning and some clay alteration.

Hornblende crystals are subhedral to euhedral, range in size from ~0.5 mm up to 1.5 mm and are pleochroic in shades of green-brown or straw yellow to dark red-brown. In contrast to the hornblende crystals within intermediate lavas described in Chapter 4.3.1, individual hornblende crystals within juvenile pyroclasts show little to no dehydration and associated alteration to Fe-oxide and/or pyroxene. However, many of the larger phenocrysts of both hornblende and plagioclase are significantly fractured and deformed.

Opaque minerals are disseminated throughout the sample and are predominantly < 0.25 mm in size and anhedral. Pyroxene and quartz form rare mineral phases within the juvenile pyroclasts forming small (0.25-0.5 mm) anhedral crystals.

In sample MSE029A, the groundmass glass has become segregated into finely and coarsely vesicular bands, which gives the rock a banded appearance (Figure 5.12).

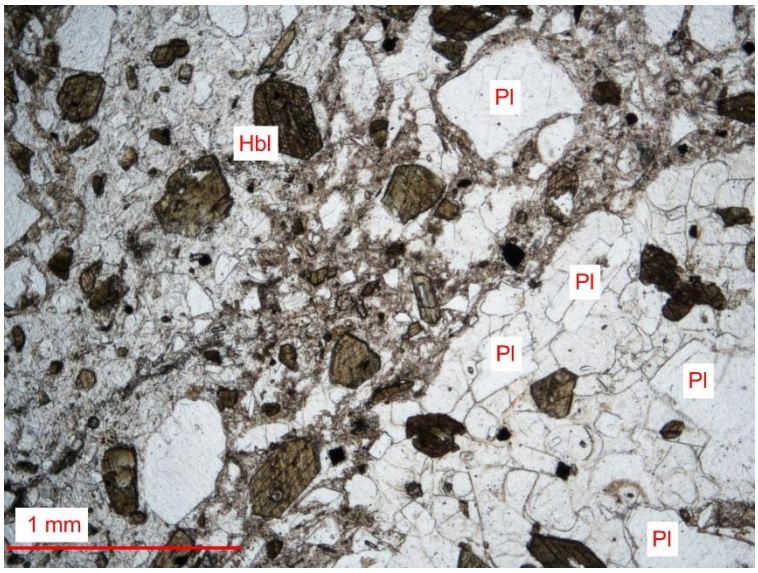

Figure 5.12. Photomicrograph under ppl of vesicular pumice pyroclast from sample MSE029A where the glass has become segregated into bands of fine and coarse vesicles. Crystal abbreviations as per Figure 5.10.

The light coloured coarsely vesicular bands consist of areas of foam-like, curved to blocky-shaped vesicles up to 0.5 mm in size which form around free crystals. The texture of the dark bands is predominately glass with fine crystallites and is finely vesicular. Vesicles are completely separated from each other and are generally less than 0.25 mm in size.

In addition to crystals, juvenile pyroclasts also contained lithics of poorly sorted, fine sandstones (Figure 5.11) and mudstones, and dense, porphyritic lavas (Figure 5.13). These accessory lithics are typically between ~0.75 mm to 2-3 mm in diameter, with the largest measuring 5 mm long by 2-3 mm wide.

The mineral assemblage of the lava lithics consists of phenocrysts of plagioclase and hornblende within a cryptocrystalline groundmass, which is similar to the host juvenile material.

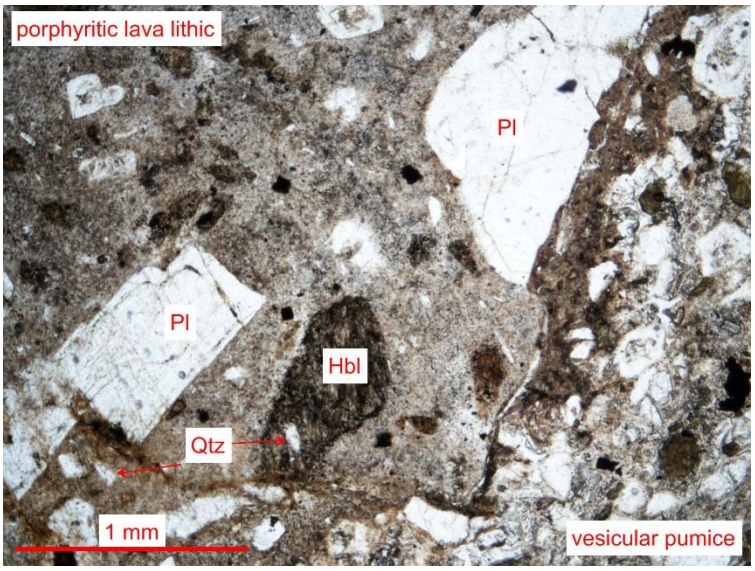

Figure 5.13. Photomicrograph of part of a lithic clast of dense porphyritic lava containing quartz (qtz) and hornblende (Hbl) within the vesicular juvenile clast of sample MSE029A.

5.5.2 Lithic clasts

Lithic clasts include angular blocks of poorly sorted, fine sandstones (Figure 5.14) and fragments of dense, porphyritic lavas (Figure 5.15) where individual clast sizes range from 1-2 cm to up to ~ 8 cm or 21 cm in diameter.

Small dark sub-rounded clasts of poorly sorted, fine sandstones were present within units QT1 and QT3 (facies A) at quarry #34. Individual clast sizes range from > 5 mm to 1-2 cm in diameter, with the largest sizes found in unit QT3 between 1-2 m (Figure 5.3). Thin sections show clasts to be dominated by quartz (Figure 5.14) and contain numerous mudstone rock fragments ranging from > 1 to 3 mm in diameter. Plagioclase and pyroxene were also identified to be rare mineral phases. No lithics of this lithology were observed within the deposit at the summit quarry.

Angular, fresh to weathered and/or altered andesite-dacite lavas are more abundant than the sandstones, but accurate estimates of their relative abundances throughout stratigraphic units at the two outcrops are difficult to determine in outcrop, however, within unit QT3 at quarry #34, the abundance of

Figure 5.14. Photomicrograph of a lithic clast comprised of a quartz-(Qtz) rich sandstone with mudstone (Mst) clasts under cross-polarized light (sample MSE028A).

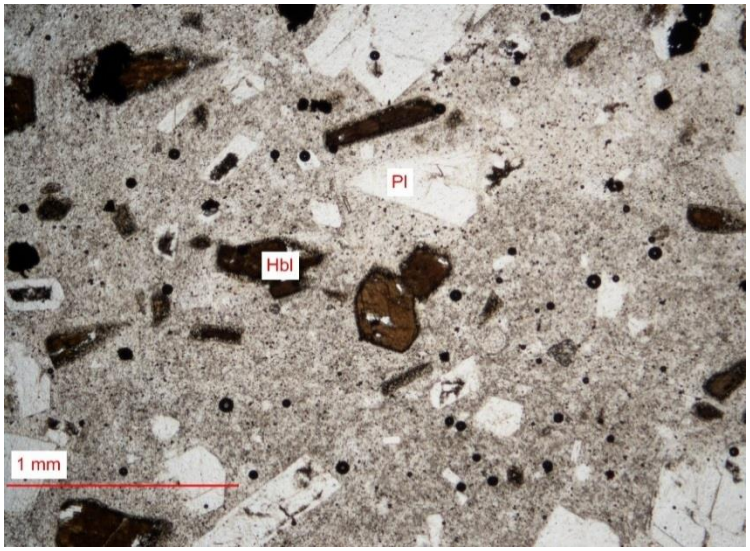

Figure 5.15. Photomicrograph of a non-vesicular, porphyritic, hornblende-rich lithic under ppl. Hornblende phenocrysts have well-developed FeO rims with many of the smaller crystals being almost completely altered. (sample MSE031)

block-sized clasts were estimated to be approximately 3-5%. Across all stratigraphic units, these clasts ranged from a few centimetres to ~8-10 cm in diameter, and are always larger than sandstone lithics when both lithologies are present. These lava lithics consist of phenocrysts of plagioclase and hornblende with disseminated opaque minerals and rare pyroxenes (Figure 5.15) within a cryptocrystalline groundmass which is identical to the juvenile pyroclasts within

the same deposits. These clasts have been distinguished from the juvenile pyroclasts by well-established dehydration rims and alteration of hornblende phenocrysts, and the widespread weathering and possible hydrothermal alteration. Hypidiomorphic-granular-textured accessory lithics of a similar mineral assemblage to the juvenile clasts were also present.

5.6 Discussion

This section interprets the origin of the various lithologies comprising the lapilli- and block-sized clasts described above and facies with respect to emplacement processes.

5.6.1 Origins of Componentry

Lithic clasts consisted of two distinct lithologies which included fragments of poorly sorted fine sandstones and fresh to weathered and/or hydrothermally altered andesitic-dacitic lava.

The poorly sorted fine sandstones within stratigraphic units QT1 and QT3 at quarry #34 are consistent with the compositionally immature, volcaniclastic sandstones which comprise the Late Jurassic Manaia Hill Group of the Waipapa Terrane which form the basement rocks within the Maungatautari field area (see Section 3.5.1). The abundance of basement lithics within units QT1 and QT3 suggests, at least during the eruption of these units, that they are fragments of country rock derived during magma fragmentation within the underlying basement rock. Basement lithics were found to be absent within deposits at the summit quarry.

The dominant lithology for lithics, however, was non-vesicular andesite-dacite lava, which occurred as lapilli- to block-sized clasts within stratigraphic units QT1, QT3, QT5, SQ1, SQ2 and SQ3 (Figure 5.3; Figure 5.6). The abundance of lithics with this lithology indicates that clasts likely originate from the fragmentation of solidified lava within or over the main conduit during vent clearing episodes.

Juvenile clasts are crystal-rich and finely vesicular to non-vesicular which suggests a relatively gas-poor magma. The dominant mineral phases consist of hornblende and plagioclase and along with the presence of minor quartz within the groundmass, this magma is considered to be dacitic in composition. The presence of tiny basement xenoliths contained within juvenile clasts may reflect country rock derived from the conduit walls during magma ascent or indicate the recycling of larger lithics within the vent area during the eruptive phase. Basement lithics within units QT1 and QT3 at quarry #34 suggests juvenile clasts were derived from fragmentation within the underlying basement rock. In contrast, the absence of this lithology in lithics within units at the summit quarry suggests fragmentation was occurring higher within the conduit, perhaps near the surface or an active lava dome.

5.6.2 Facies Interpretation and Emplacement Processes

Composite cones, such as Maungatautari, are typically constructed from intercalated small flows of viscous andesitic-dacitic lavas and pyroclastic deposits from explosive strombolian, vulcanian, sub-plinian and plinian eruption styles (Parfitt & Wilson, 2008).

The poorly sorted, compositionally varied, matrix-supported nature of the two pyroclastic successions found at Maungatautari are consistent with deposits resulting from pyroclastic density currents (PDCs) and therefore exclude pyroclastic fall as a possible emplacement mechanism (Cowlyn, 2016; Parfitt & Wilson, 2008). Pyroclastic density currents can be broadly separated into those that result directly from explosive volcanic eruptions (Cole *et al.*, 2002; Cowlyn, 2016) and those resulting from collapse of erupted material already present at the volcano's surface, where high elevations and steep topographic gradients provide multiple opportunities for gravitational collapse of erupted material (Cole *et al.*, 2002; Saucedo *et al.*, 2004). PDCs are further subdivided into having either a high or low particle concentration (pyroclastic flows and surges respectively), which form two end members of a continuum in particle concentration and flow

mechanisms that vary in time and space in response to changes in source conditions, deposition and irregular and laterally changing substrate (Brown & Andrews, 2015). The two main models for the deposition of PDCs are progressive aggradation or *en masse* freezing which may occur as a steady, discontinuous or stepwise process (Sulpizio & Dellino, 2008). As such, deposits of PDCs can demonstrate an extensive array of deposit textures and structures.

The lack of pyroclastic exposures across Maungatautari makes any correlation of the individual units between the two outcrops impossible. Each facies is therefore interpreted independently to access the volcanic processes which likely occurred during the deposition of the associated stratigraphical units.

Facies A

Facies A comprises over 60 % of the pyroclastic successions and predominately consists of massive, poorly sorted, fine to coarse lapilli tuff with regular angular blocks. Units of this facies are interpreted to reflect deposition from high particle concentration pyroclastic density currents (pyroclastic flows) resulting from vent-clearing, vulcanian- to sub-plinian-style eruptions.

Stratigraphic unit QT3 (Figure 5.3) is, at 2.5 m thick, the thickest bed attributed to this facies. Comprised of poorly sorted coarse lapilli tuff with angular blocks, the upper 1 m of this unit is normally graded. Such a graded deposit may represent deposition by progressive aggradation which describes how a PDC deposit accumulates incrementally and gradually from particles at the base of the flow. Vertical sections therefore reflect temporal variations at the base of a current as it passes a particular location (Dufek *et al.*, 2015; Sulpizio & Dellino, 2008). Other thick (> 0.6 m) units attributed to this facies include units QT1 (Figure 5.3) and SQ2 (Figure 5.6). These units are textually similar to unit QT3 but show no internal grading. As such, it is more difficult to attribute the deposition of these units to progressive aggradation and they were more likely deposited en masse, where the flow came to an abrupt halt over its entire depth (Sulpizio & Dellino, 2008).

The thinnest (< 0.5 m thick) stratigraphic units attributed to this facies include units QT5 and QT8 (Figure 5.3) which consist of massive, moderately sorted, fine-medium lapilli tuffs. Texturally, these units are also similar to units QT1, QT3 and SQ2 described above, except for slightly better sorting with a finer average grain size. While these units have been included in faces A, the attribution to high particle concentration PDCs is uncertain as low particle concentration PDCs are also able to produce massive deposits when the time between particle collisions is short relative to particle-fluid drag (Dufek *et al.*, 2015). In these flows, particle motion is mostly influenced by particle collisions resulting in massive deposits which are often interpreted to come from pyroclastic flows.

Facies B

The laminated (< 1 cm in thickness) to very-thinly bedded (1-2 cm) interbedded crystal and lithic-rich coarse tuff with very-fine lapilli of facies B is attributed to deposition from low particle concentration PDCs (pyroclastic surges). Clasts within a fully turbulent PDC segregate vertically into three partially overlapping levels within the current (traction, intermittent suspension and suspension) based on differing hydraulic properties (Sulpizio & Dellino, 2008). The coarser and denser particles occur in the lower portion of the flow where particles are intermittently suspended by turbulence (saltation) or in the case of the traction population, are transported in a sliding and rolling motion. The basal portion of the flow can move down-slope as a succession of pulses leading to the formation of sets of planar beds (Cas & Wright, 1987; Sulpizio & Dellino, 2008; Torres-Orozco *et al.*, 2017). The grainsize variation between individual laminae in this facies is consistent with the pulsating models described above where repeated deposition of fine lapilli was followed by coarse tuff. The stratigraphical units of this facies (QT2, QT7 and QT9), are generally found overlying those of facies A. The gradational lower contact between units QT8 and QT9 may reflect a transition from a high to low particle concentration within a single flow event (pyroclastic flow to surge). Overall normal grading of individual units reflects waning of discrete vulcanian-style explosive events.

Facies C

Facies C is comprised of two very thin beds (units QT4 and QT6) which consist of massive, well sorted coarse tuff. Both these beds directly overly those of PDC deposits belonging to facies A and have been interpreted to originate from the fallout of ash from a buoyant co-PDC plume during a pause in PDC activity (Brown & Andrews, 2015).

Facies D

Stratigraphic unit SQ1 at the summit quarry was the only unit attributed to facies D. It comprised the lower 0.5 m of the succession (Figure 5.6) and differed from the massive lapilli tuff of facies A by a significantly higher proportion of ash-sized matrix, estimated in the field to be ~60-70%. The maximum thickness of this unit is unknown as the basal contact is not exposed however, the unit grades into an overlying unit of facies A. Angular blocks consisted of hornblende-rich fresh, weathered and/or altered andesite-dacite lavas and there is a notable absence of sedimentary lithics. Facies D is therefore interpreted to reflect a block and ash flow. Such flows result from the gravitational collapse of highly unstable brittle outer margins of the dome which may occur both during and after growth (Calder *et al.*, 2015). Block and ash flows are composed of material that readily fragments (Cole *et al.*, 2002), generating large amounts of fine-grained material which comprises the matrix of this unit.

Facies E

Facies E also occurs only as a single stratigraphic interval (unit SQ3) within the summit quarry and consists of reversely graded blocks of non-vesicular, porphyritic hornblende-rich andesitic-dacitic lavas within a massive and poorly sorted (silt-pebble-sized) matrix. Based on the deposit geometry, block composition, poorly sorted matrix and the distinct fines-rich base, this unit is interpreted to have been deposited by a lahar. Lahar genesis requires an adequate supply of water, in addition to abundant unconsolidated debris, which could have been sourced from a crater lake (Keys & Green, 2008), melting of snow/ice

(Pierson *et al.*, 1990) or high rain-fall events (Capra *et al.*, 2010) and none of these possibilities were able to be excluded as a trigger for this particular event. The deposit is thickest in the centre of what appears to be a channel which has been eroded into the underlying pyroclastic unit (Figure 5.5) and thins considerably to form thin veneers at the outer margins. The deposit geometry suggests this unit was emplaced within an existing channel into the underlying pyroclastic unit SQ2 and therefore it is interpreted to represent a secondary, non-eruption related event, rather than primary (syneruptive) event (Vallance & Iverson, 2015).

5.6.3 Interpretation of the physical volcanology and evolution of two eruptive events

The pyroclastic successions at Maungatautari likely resulted from complex, multiple phase eruptions which included cycles of dome growth and collapse, and the repeated production of eruption columns from associated vulcanian to sub-plinian style activity which created numerous PDCs. This activity was likely centred at a now-eroded summit vent and occurred over a period of days, weeks or months.

Summit Quarry

The evolution of the succession at the summit quarry is summarised in Figure 5.16. Unit SQ1 is the lowest stratigraphical unit in this succession and only the upper 0.5 m of the deposit is exposed, representing a block and ash flow resulting from the partial collapse of a summit lava dome (Figure 5.16B). The collapse allowed depressurization of the conduit, triggering an explosive eruption. At some point, the erupted material formed into a PDC (Figure 5.16C) which may have originated as a directed blast towards the north, boiling-over (i.e. immediate collapse) of the eruption column or subsequent collapse of the eruption column as activity waned.

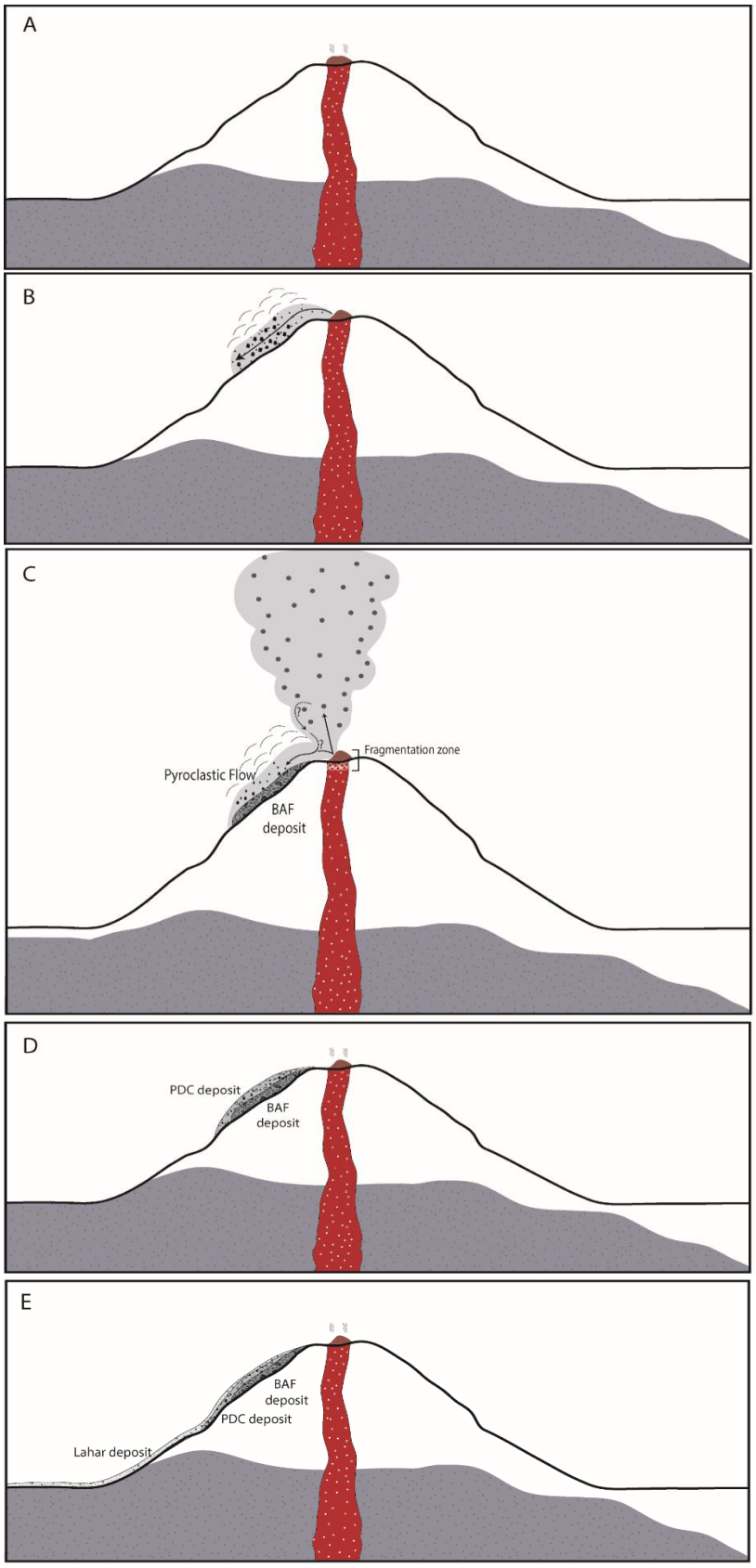

Figure 5.16. Schematic diagram depicting the evolution of the volcanic eruption leading to the deposition at the summit quarry. A) Passive effusion of summit lava dome. B) Partial collapse of lava dome resulting in deposition of block-and-ash flow deposit (unit SQ1). C) Depressurisation triggers pyroclastic flow generating eruption (Unit SQ2). D) Period of quiescence and erosion. E) Lahar of unknown genesis which flowed through eroded channel created in time D.

As such, the block and ash flow deposit grades into the pyroclastic flow deposit of unit SQ2. Following the PDC and deposition of unit SQ2, erosion created a channel that acted as a major pathway for the flow of a lahar (Figure 5.16E).

Quarry #34

Quarry #34 is comprised of 9 stratigraphical units, each one reflecting a distinct, stratigraphically identifiable depositional layer with clear textural lower and upper boundaries and interpreted to be the product of at least one distinct PDC. It is recognised that the field observations and descriptions of PDC units from this stratigraphic section may under-represent the total number of PDCs contributing to the overall package which may reflect deposition over one or more eruptive events.

The early eruptive activity which led to the deposition of the pyroclastic succession at quarry #34 is unknown. Thus, the eruptive history of this outcrop begins with a high particle concentration PDC (i.e. pyroclastic flow) which led to the deposition of unit QT1 (Figure 5.17). The sharp upper contact between unit QT1 and the overlying unit QT2, marks the abrupt change to that of a low-particle concentration PDC (i.e. pyroclastic surge) and reflects two distinct currents within the same eruptive event. The undulating, yet sharp, contact between units QT2 and QT3 may reflect a pause in the eruptive sequence and subsequent erosion, or more likely, the erosion of unit QT2 during the passing of the high particle concentration PDC which led to the deposition of unit QT3. At over 2.5 m thick, unit QT3 is the thickest single unit. The first 1.5 m is rich in juvenile and lithic clasts of both basement and volcanic origin and indicates a relatively moderate sized eruption of an open system where magmatic fragmentation occurred within the conduit, likely at a depth within the underlying basement. Above 1.5 m in Figure 5.17 the unit QT3 displays normal coarse-tail grading and is topped by a thin (30 mm) layer of well sorted, coarse tuff which reflects deposition from the fallout of ash from a buoyant co-PDC plume (unit QT4). This tuff layer suggests a short pause

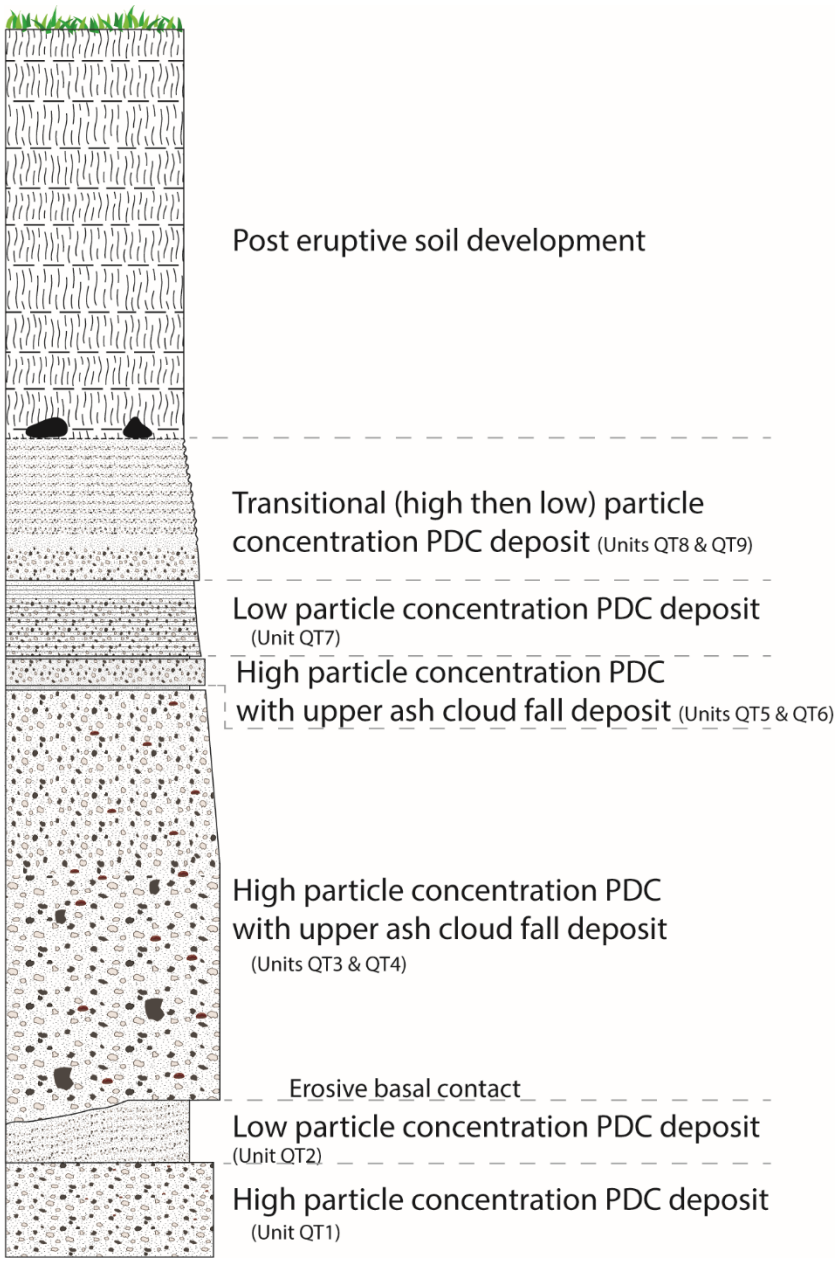

Figure 5.17. Graphic log summarizing eruptive mechanisms resulting in the deposition of units at quarry #34.

in PDC activity allowing time for particles within the buoyant ash cloud to settle. A similar origin of high particle concentration PDC followed by the fallout of ash is interpreted for the deposition of units QT5 and QT6 (Figure 5.17). These are overlain by the planar stratified, low particle concentration PDC deposits of unit QT7. Sets of laminae consisting of fine lapilli followed by coarse tuff are interpreted to reflect pulses within the overall surge current. Normal grading

within this unit represents a waning in activity. The upper units of the succession consist of a bed of fine lapilli which grades into planar stratified fine lapilli and coarse tuff of units QT8 and QT9 respectively. These units may reflect either two discrete PDCs or potentially one PDC where the deposit records the variation in flow dynamics from high to low particle concentration as it passes. These units are overlain by reworked colluvium which forms a paleosol, highlighted by the presence of rounded boulders that litter the surface. Subsequent volcaniclastic deposition and in situ soil formation comprises the remaining exposure.

Comparison of the two pyroclastic successions

The interpretation of the pyroclastic successions at quarry #34 and the summit quarry have contrasting eruptive histories. The summit quarry consists of a block and ash flow deposit (unit SQ1) resulting from the collapse of a lava dome, followed by an explosive eruption which generated a PDC (unit SQ2) and a lahar (SQ3). In contrast, the succession at quarry #34 depicts multiple PDC events (units QT1, QT2, QT3, QT5, QT7, QT8 and QT9) as a series of alternating pyroclastic flows and surges, some with upper co-PDC fall deposits (units QT4 and QT6). The presence of basement lithics within units QT1 and QT3 represents a deeper fragmentation depth within the underlying Jurassic strata for the eruption associated with quarry #34.

Chapter Six:

Chapter Summaries and Conclusions

6.1 Introduction

Composite cones are prominent landscape features of continental volcanic arcs globally (Graham *et al.*, 2008; Hildreth & Lanphere, 1994; Stern, 2004). The repeated eruption of lava and pyroclastic deposits from a central vent creates a broadly conical edifice which often belies the complex interplay between different volcanic and sedimentary processes which occur throughout the history of a single edifice. Maungatautari is a bush-covered, andesitic-dacitic composite cone situated 35 km southeast of Hamilton within the Waipa District, Waikato. While volcanism at Maungatautari was previously addressed in context of the broader volcanic geology of the Waikato region during the 70s and 80s, the only dedicated volcanic study of Maungatautari was conducted by Briggs (1986b) and provided insight into the chemical composition and origin of the magmas.

This study has applied modern volcanological techniques and concepts to provide an improved understanding of the volcanic history of the Maungatautari and how it may relate to volcanism elsewhere in the Waikato Region around 2 Ma. This was achieved by:

- re-assessment and mapping of the major geological and geomorphological components of Maungatautari and immediate surrounds using field observation and GIS software (Chapter 3),
- petrographic and whole rock elemental and isotopic characterisation of the Maungatautari lavas (Chapter 4), and
- assessment of the physical volcanology of two Maungatautari pyroclastic successions (Chapter 5).

6.2 Geology and geomorphology

The general geology and geomorphology of Maungatautari is described in Chapter 3. Maungatautari overlies Jurassic Manaia Hill group rocks of the Waipapa Terrane and abuts a range of the same rocks immediately to the west (Leonard *et al.*, 2010). Surrounding Maungatautari to the north, east and south is a thick (>100

m) ignimbrite plateau which overlies the lowermost flanks of the mountain and is comprised of deposits of the Pakaumanu Group, which includes the Rocky Hill and Kidnappers (Raepahu Formation) and the Ahuroa (Mangaokewa Formation) ignimbrites which originate from the Mangakino caldera to the southeast (Leonard *et al.*, 2010; Olissoff, 1981). The geological map produced for this study is mostly consistent with that of Leonard *et al.* (2010), except for the extended ring plain of lahar deposits mapped to the north and encircling the mountain (see Healy *et al.* (1964) and Leonard *et al.* (2010)), has been replaced in Figure 3.6 with undifferentiated Pakaumanu Group Ignimbrites. This variation from previous geological maps reflects field evidence of lahar deposits being highly channelised within the stream valleys and often below the uppermost surface level and stratigraphic logs of water bores from Waikato Regional Council (n.d.). The mountain displays extreme relief with sharply convex ridgelines with steep (>25^{o}) slopes in the upper portions of the mountain that are deeply incised by gullies. Native forest extensively covers the upper slopes resulting in poor outcrop exposure, with the majority being found around the main peaks, along the sides of very steep gullies and in cuttings along the length of publicly accessible walking tracks. Outside the perimeter fence lower slopes are more rounded with moderate to gentle (6-25^{o}) slopes and are covered in pasture.

The three major volcanic vents of Kairangi, Oreipunga and an inferred eroded summit vent centred near Maungatautari Trig display a distinct northwest alignment mirrored within the nearby Alexandra Volcanic Group. A variety of volcanic deposits were observed, and consisted of lavas, dikes, volcanic and hydrothermal breccias, and lapilli tuffs. The combination of inherently weak rocks and rapid growth, predispose volcanoes to large scale slope or flank failures and have become increasingly well-recognised at composite cones around New Zealand and worldwide (Gaylord & Neall, 2012; Glicken, 1990; Goles *et al.*, 1996; Zernack *et al.*, 2009), with many demonstrating complex histories of collapse and regrowth (Thouret, 1999; Zernack *et al.*, 2009). Maungatautari highlights that such catastrophic mass-wasting is an ongoing process, even after the end of volcanism. A 0.28 km^{3} rock avalanche failure of the northeastern flank is

characterised by a horse-shoe-shaped, steep-sided break-away scarp and large hummocks which cover a depositional area approximately 1.6 km^2 in size. The geomorphology of the southern half of the mountain is also suggestive of edifice spreading, however, this hypothesis remains speculative and further studies into the stability of the mountain are required to confirm this. In addition to the rock avalanche on the northeast flank, the deposits of rock falls, slides and debris flows were also commonly observed and demonstrate the numerous mass-wasting processes which have occurred in the past, and continue to shape the mountain through time.

6.3 Petrology of lavas

The petrology of Maungatautari and Kairangi lavas are investigated in Chapter 4. Rock types consist of non-vesicular olivine basalt, labradorite, pyroxene and hornblende andesites and hornblende dacites. Seriate porphyritic textures and glomerocrysts are common. Phenocrysts include plagioclase, orthopyroxene, clinopyroxene, hornblende, opaque Fe-Ti oxides and olivine within intergranular, intersertal, trachytic and hyalopilitic groundmass.

Lava samples from across Maungatautari are defined as med-high K andesites and dacites. Progressive increases in Na_2O and K_2O, and concomitant decreases in MgO, Fe_2O_3, CaO, TiO_2 with increasing SiO_2 imply that the evolution of Maungatautari lavas was dominated by the fractional crystallisation of a parent magma. Trace element classification and multielement diagrams, however, reveal two distinct variations which are geochemically and isotopically distinct. Firstly, the low-silica hornblende andesites are characterised by enrichment in the heavy REE and more radiogenic Sr values and lower LIL element concentrations while the Kairangi basalt has significantly higher radiogenic Nd and relatively non-radiogenic Sr values. This suggests that the lavas from Maungatautari and Kairangi are derived from at least three distinct mantle-melt sources where most of the andesites and dacites at Maungatautari are petrogenetically related and associated with the fractionation of andesites to dacites from subduction-related,

deep, garnet-bearing, depleted mantle. The low SiO_2 hornblende andesites, however, are derived from a shallower upper mantle (garnet-free) source rock and the Kairangi olivine basalt displays a geochemical signature similar to lavas of the nearby Okete Field and originates from an area of enriched mantle.

Multi-element and REE patterns for Maungatautari lavas are interpreted to represent volcanism associated with the main volcanic arc which extended south from Tauranga to Maungatautari into continental New Zealand c. 2 Ma. In contrast, the near-by Alexandra Volcanics are considered to be contemporaneous, behind-arc subduction-related volcanism and this view is consistent with those of Briggs *et al.* (2013). With a less pronounced negative Nb anomaly and an overall smoother pattern, the alkali olivine basalt at Kairangi is more reflective of intraplate over subduction-related melts and confirms Briggs (1986a) view that the Kairangi olivine basalt is petrogenetically unrelated to the magmas at Maungatautari.

Gold prospecting at Maungatautari occurred between 1880 and 1910 (Gold discovery at Maungatautari, 1887). A gold workings site was located within in the headwaters of the Mangakara Stream, an area previously noted for the presence of hydrothermally altered rocks (Briggs, 1986b). This area is interpreted to reflect a zone of low-sulfidation hydrothermal alteration where intense acidic alteration of the host rock is characterised by a mineral assemblage of cristobalite, alunite and kaolinite. This passed outwards into an outer zone of propylitic alteration as the acidic water was progressively neutralised by the host. Such alteration styles suggest a surficial hydrothermal zone including highly acidic fumaroles and hot springs was once present at this site. In contrast, a spring discharging pH neutral fluids may have been located in what is now a tributary to the Mangapiko Stream.

6.4 Physical volcanology of pyroclastic successions

Chapter 5 described the location, field and facies characteristics and lapilli and block componentry of Maungatautari eruptive events located along the main walking track at quarry #34 and near the summit. This study is the first to

document any record of explosive volcanism at Maungatautari (cf. Briggs (1986b); Olson (1950) who focussed on lavas only).

The stratigraphical units of each succession were grouped into five facies. The massive, moderately-poorly sorted, lapilli tuffs of facies A and the laminated-bedded coarse tuff and very-fine lapilli of facies B, represent deposition from high and low particle concentration pyroclastic density currents respectively (Figure 5.3). Units QT3 and QT5 at quarry #34 were overlain by a thin bed of massive coarse tuff (facies C), which originates from the fallout of ash from a buoyant co-PDC plume. Only one stratigraphical unit was attributed to facies D (unit SQ1) and facies E (unit SQ3) which were located within the succession from the summit quarry (Figure 5.6). The poorly sorted, non-welded massive lapilli tuff of facies D is interpreted to reflect a block and ash flow generated by the gravitational collapse of the highly unstable brittle outer margins of a summit lava dome. The upper unit of this succession is attribute to facies E which is considered epiclastic rather than pyroclastic in origin. It consists of reversely graded blocks of non-vesicular, porphyritic hornblende-rich andesitic-dacitic lavas within a massive and poorly sorted (silt-pebble sized) matrix, reflective of a lahar.

Lapilli and blocks were comprised of crystal-rich, vesicular and non-vesicular juvenile clasts and lithic clasts of two distinct lithologies - fragments of poorly sorted fine sandstones of the Late Jurassic Manaia Hill Group basement rocks and fresh to weathered and/or altered andesitic-dacitic lava derived from pre-existing solidified lava within or over the main conduit that was fragmented during vent clearing episodes. While juvenile and lava derived lithic clasts were found at both sites, no lithics of basement lithology were observed within the deposits at the summit quarry. Despite the similarities in clast componentry, quarry #34 and the summit quarry have contrasting eruptive histories. The summit quarry consists of a block-and-ash flow deposit resulting from the collapse of a lava dome, followed by an explosive eruption which generated a pyroclastic density current and a lahar. In contrast, the succession at quarry #34 depicts multiple pyroclastic density current pulses (units QT1, QT2, QT3, QT5, QT7, QT8 and QT9) as a series of alternating pyroclastic flows and surges. This activity was likely centred around a

now-eroded summit vent and occurred over a period of days, weeks or months. The presence of basement lithics within units 1 and 3 at quarry #34 represents a fragmentation depth within the underlying Jurassic strata, at least during the eruption of these units, and confirms that the Maungatautari edifice lies directly above Manaia Hill Group basement rocks.

6.5 Geologic and volcanic evolution of Maungatautari

Age data for Maungatautari is limited and as such, the volcanic evolution of Maungatautari area is based on the stratigraphic relationships between the basement-Maungatautari-ignimbrite succession and mass wasting events described in Chapter 3.

Volcanism within the Maungatautari area began with the eruption of alkali olivine basalt 2.62 Ma (Briggs *et al.*, 1989), to produce the small basalt cone of Kairangi which sits on uplifted and eroded Jurassic Manaia Hill group rocks of the Waipapa Terrane. The centre of volcanism then shifted 7 km southeast where, over time, the repeated eruption of intercalated small flows of viscous andesitic-dacitic lavas and pyroclastic deposits from explosive strombolian, vulcanian and possibly sub-plinian eruption styles. This activity led to the creation of the roughly circular edifice of Maungatautari which is dated at c. 1.8 Ma (Robertson, 1983), although the total period of activity remains unknown. An eruption of dacitic magma on the eastern flank led to the development of Oreipunga Cone. Thermal energy and vapours provided by the underlying magmatic system interacted with meteoric water to produce acidic fumaroles and hot springs on the upper slopes of the mountain in what is now the headwaters of the Mangakara Stream. Eventually, volcanism at Maungatautari ceased as activity shifted east to the newly formed Taupo Volcanic Zone. The eruption of ignimbrites from the Mangakino caldera, located to the southeast, resulted in the deposition of a thick ignimbrite plateau which now surrounds Maungatautari. The timing of the rock avalanche event in the northeast corner is poorly constrained, but the lack of edifice reconstruction and absence of ignimbrites over or between hummocks suggests it occurred

within the last one million years after both the volcanic activity at Maungatautari had ceased and the ignimbrite plateau had been emplaced. The ongoing erosion of Maungatautari continues to shape the remains of the edifice present today.

6.6 Implication of findings and synthesis with modern analogues

Dated at c. 1.8 Ma (Robertson, 1983), activity at Maungatautari is contemporaneous with the beginning of volcanism in the Taupo Volcanic Zone (Cole & Teoh, 1975; Froude & Cole, 1985), and that occurring towards the end of activity at nearby Karioi and Pirongia (Briggs *et al.*, 1989). During this time, the Maungatautari and southern Waikato landscape would have been comparable to Mount Taranaki and the currently-active central plateau volcanoes of Tongariro and Ruapehu. Many features which are prevalent on these modern-day analogues are also evident at Maungatautari and include: upper flank intense acidic hydrothermal alteration which manifest as hot springs and acidic fumaroles (Simpson & Bignall, 2016), multiple vents (Hobden *et al.*, 1996); a flank cone (Downey *et al.*, 1994) and catastrophic flank collapse (Gaylord & Neall, 2012; Tost *et al.*, 2014).

Geographically related and sometimes intercalated alkali intraplate and subduction related melts is also a well-documented feature of some continental volcanic arcs (Briggs & McDonough, 1990; Stern, 2004). This is represented at Maungatautari by the small basaltic cone at Kairangi where the eruption of alkali olivine basalt occurred 7 km northwest of the main edifice. Dated at 2.62 Ma (Briggs *et al.*, 1989), volcanism at Kairangi appears to predate that at Maungatautari and may represent the inception of volcanism within the area, however, their exact temporal relationship remains uncertain.

To date, no lava of basaltic or basaltic andesite composition has been found at Maungatautari. The composition of any potential basaltic parental melt remains unknown and the possibility that Maungatautari lavas are instead derived from a

primitive andesite, has not been excluded. Primitive andesites are typically a feature of continental volcanic arcs (Kelemen *et al.*, 2013). These magmas are commonly emplaced as plutonic rocks in the middle and upper crust, potentially never erupting at the surface where delamination of the lower crust eventually recycles them back into the mantle.

This study considers Maungatautari to reflect andesitic volcanism occurring along the edge of the continental tip of the Colville volcanic arc c. 2 Ma (Figure 4.2). This interpretation deviates from the earlier interpretation by Briggs (1986b) where it was considered to be a subduction-related volcano situated behind the volcanic front. The proximity of Maungatautari to the subduction-related back-arc volcanoes of the Alexandra volcanic group (Briggs *et al.*, 2013) suggests that volcanism here may have occurred along the margin of a magmatic system which migrated eastward through time. This is also supported by the close age association between Maungatautari and Titiraupenga and Pureora which lie 55-60 km respectively to the southeast and the Tauranga volcanic centres ~60 km to the northeast. Maungatautari, like all the other volcanics within the western Waikato region, occur along the margins of basement highs. While there are no recognised volcanic landforms within the basin, the extent of volcanism of similar age beneath the younger Hamilton Basin is unknown.

6.7 Conclusions

The overall conclusions of this study are outlined below:

- Maungatautari is an andesitic-dacitic composite cone which overlies Jurassic Manaia Hill group rocks of the Waipapa Terrane and abuts a range of the same rocks immediately to the west. It is surrounded to the north, east and south by a thick ignimbrite plateau which overlies the lowermost flanks of the mountain and is comprised of deposits of the Pakaumanu Group, which includes the Rocky Hill and Kidnappers (Raepahu Formation) and the Ahuroa (Mangaokewa Formation) ignimbrites which originate from the Mangakino caldera to the southeast.

- Catastrophic failure of the northeastern flank produced a 0.28 km^3 rock avalanche event which is defined by a horse-shoe-shaped, steep-sided break-away scarp and large hummocks which cover a depositional area approximately 1.6 km^2 in size. Geomorphic evidence suggests other failure events may have occurred throughout the history of the volcano.

- Lavas at Maungatautari are derived from at least three distinct mantle-melt sources with most andesites and dacites being petrogenetically related and associated with the fractionation of subduction-related, deep, garnet-bearing, depleted mantle source rock. In contrast, the low SiO_2 hornblende andesites and Kairangi olivine basalt are derived from a shallower upper mantle (garnet-free) source rock and an area of deeper enriched mantle, respectively.

- Volcanism at Maungatautari is a part of the Colville volcanic arc which extended south from Tauranga to Maungatautari into continental New Zealand c. 2 Ma with the near-by Alexandra Volcanics being contemporaneous, behind-arc subduction-related volcanoes. The alkali olivine basalt at Kairangi is more reflective of intraplate over subduction-related melts and is unrelated to magmatism at Maungatautari.

- Eruption styles at Maungatautari included: the effusion of lava resulting in the generation of lava flows and domes, and vulcanian to sub-plinian explosive eruptions which produced numerous PDCs.

6.8 Future work

This thesis improves our understanding on the volcanic history of Maungatautari and how it relates to volcanism elsewhere in the Waikato Region which occurred c. 2 Ma. However, the single date of 1.8 Ma by Robertson (1983) provides poor age control and future work should aim to obtain a more comprehensive set of

ages to better constrain the age range for volcanic activity across the Maungatautari edifice. This could be combined with more extensive local and regional mapping to determine the presence and possible extent of a ring plain beneath the ignimbrite sheet. Investigations into the stability of the edifice is also advised to determine the possibility of future flank collapse. On a more regional scale, comparative studies with the nearby volcanoes of Pureora and Titiraupenga may also shed light on similarities and/or differences between Maungatautari and the early andesitic volcanism of the TVZ.

Future track development will continue to expose new outcrops across the mountain and continued collaboration between the scientific community and the Maungatautari Ecological Island Trust is essential to enable cataloguing of such sites.

Each year, thousands of people of all ages visit Sanctuary Mountain Maungatautari to learn about the native flora and fauna which makes it unique. It is hoped the findings of this study will be used to add to the visitor experience by highlighting the volcanic origins of the mountain and help increase public awareness of the local landscape and natural history of this unique and treasured environment.

References

Adams, C. J., Graham, I. J., Seward, D., Skinner, D. N. B., Adams, C. J., Skinner, D. N. B., & Moore, P. R. (1994). Geochronological and geochemical evolution of late cenozoic volcanism in the Coromandel Peninsula, New Zealand. *New Zealand Journal of Geology and Geophysics, 37*(3), 359-379.

Andrade, S. D., & van Wyk de Vries, B. (2010). Structural analysis of the early stages of catastrophic stratovolcano flank-collapse using analogue models. *Bulletin of Volcanology, 72*(7), 771-789.

Bache, F., Sutherland, R., Stagpoole, V., Herzer, R., Collot, J., & Rouillard, P. (2012). Stratigraphy of the southern Norfolk Ridge and the Reinga Basin: A record of initiation of Tonga–Kermadec–Northland subduction in the southwest Pacific. *Earth and Planetary Science Letters, 321–322*, 41-53.

Ballance, P. F. (1976). Evolution of the upper cenozoic magmatic arc and plate boundary in northern New Zealand. *Earth and Planetary Science Letters, 28*(3), 356-370.

Black, P. M., Briggs, R. M., Itaya, T., Dewes, E. R., Dunbar, H. M., Kawasaki, K., Kuschel, E., & Smith, I. E. M. (1992). K-Ar age data and geochemistry of the Kiwitahi Volcanics, western Hauraki Rift, North Island, New Zealand. *New Zealand Journal of Geology and Geophysics, 35*(4), 403-413.

Bodinier, J. I., Merlet, C., Bedini, R. M., Simien, F., Remaidi, M., & Garrido, C. J. (1996). Distribution of niobium, tantalum, and other highly incompatible trace elements in the lithospheric mantle: The spinel paradox. *Geochimica et Cosmochimica Acta, 60*(3), 545-550.

Booden, M. A., Smith, I. E. M., Mauk, J. L., & Black, P. M. (2010). Evolving volcanism at the tip of a propagating arc: The earliest high-Mg andesites in northern New Zealand. *Journal of Volcanology and Geothermal Research, 195*(2–4), 83-96.

Booden, M. A., Smith, I. E. M., Mauk, J. L., & Black, P. M. (2012). Geochemical and isotopic development of the Coromandel Volcanic Zone, northern New Zealand, since 18 Ma. *Journal of Volcanology and Geothermal Research, 219–220*, 15-32.

Briggs, R. (1986a). Volcanic rocks of the Waikato Region, western North Island, and some possible petrologic and tectonic constraints on their origin. In I. E. M. Smith (Ed.), *Late cenozoic volcanism in New Zealand* (pp. 76-91). Wellington, New Zealand: The Royal Society of New Zealand Bulletin 23.

Briggs, R. M. (1983). Distribution, form, and structural control of the Alexandra Volcanic group, North Island, New Zealand. *New Zealand Journal of Geology and Geophysics, 26*(1), 47-55.

Briggs, R. M. (1986b). Petrology and geochemistry of Maungatautari, a medium-k andesite-dacite volcano. *New Zealand Journal of Geology and Geophysics, 29*(3), 273-289.

Briggs, R. M., Gifford, M. G., Moyle, A. R., Taylor, S. R., Norman, M. D., Houghton, B. F., & Wilson, C. J. N. (1993). Geochemical zoning and eruptive mixing in ignimbrites from Mangakino volcano, Taupo Volcanic Zone, New Zealand. *Journal of Volcanology and Geothermal Research, 56*(3), 175-203.

Briggs, R. M., & Goles, G. G. (1984). Petrological and trace element geochemical features of the Okete Volcanics, western North Island, New Zealand. *Contributions to mineralogy and petrology, 86*(1), 77-88.

Briggs, R. M., Goles, G. G., & Maas, R. (2013) Karioi volcano, western North Island, New Zealand: a behind arc polygenetic intraplate-convergent margin volcanic complex. *Poster presented at the IAVCEI Scientific Assembly*. Kagoshima, Japan.

Briggs, R. M., Houghton, B. F., McWilliams, M., & Wilson, C. J. N. (2005). 40Ar/39Ar ages of silicic volcanic rocks in the Tauranga-Kaimai area, New Zealand: Dating the transition between volcanism in the Coromandel Arc and the Taupo Volcanic Zone. *New Zealand Journal of Geology and Geophysics, 48*(3), 459-469.

Briggs, R. M., Itaya, T., Lowe, D. J., & Keane, A. J. (1989). Ages of the Pliocene-Pleistocene Alexandra and Ngatutura Volcanics, western North Island, New Zealand, and some geological implications.

Briggs, R. M., & McDonough, W. F. (1990). Contemporaneous convergent margin and intraplate magmatism, North Island, New Zealand. *Journal of Petrology, 31*(4), 813-851.

Briggs, R. M., Okada, T., Itaya, T., Shibuya, H., & Smith, I. E. M. (1994). K-Ar ages, paleomagnetism, and geochemistry of the South Auckland Volcanic Field, North Island, New Zealand. *New Zealand Journal of Geology and Geophysics, 37*(2), 143-153.

Brown, R. J., & Andrews, G. (2015). Chapter 36 - Deposits of pyroclastic density currents. In H. Sigurdsson (Ed.), *The Encyclopedia of Volcanoes (Second Edition)* (pp. 631-648). Amsterdam: Academic Press.

Calder, E. S., Lavallée, Y., Kendrick, J. E., & Bernstein, M. (2015). Chapter 18 - Lava dome eruptions. In H. Sigurdsson (Ed.), *The Encyclopedia of Volcanoes (Second Edition)* (pp. 343-362). Amsterdam: Academic Press.

Campbell, H., Mortimer, N., & Science, G. N. S. (2014). *Zealandia: our continent revealed*. Auckland, New Zealand: Penguin Books.

Capra, L., Borselli, L., Varley, N., Gavilanes-Ruiz, J. C., Norini, G., Sarocchi, D., Caballero, L., & Cortes, A. (2010). Rainfall-triggered lahars at Volcán de Colima, Mexico: Surface hydro-repellency as initiation process. *Journal of Volcanology and Geothermal Research, 189*(1), 105-117.

Cas, R., & Wright, J. (Compiler) (1987). *Volcanic successions, modern and ancient: A geological approach to processes, products and successions*: Allen and Unwin, St Leonards, NSW, Australia.

Clavero, J., Sparks, R., Huppert, H., & Dade, W. (2002). Geological constraints on the emplacement mechanism of the Parinacota debris avalanche, northern Chile. *Bulletin of Volcanology, 64*(1), 40-54.

Cole, J., Briggs, R. M., & Smith, I. (2008). Progression. In I. J. Graham (Ed.), *A continent on the move: New Zealand geoscience into the 21st century* (pp. 154-157). Wellington, New Zealand: Geological Society of New Zealand in association with GNS Science.

Cole, J., & Teoh, L. (1975). Petrography, mineralogy, and chemistry of Pureora andesite volcano, North Island, New Zealand. *New Zealand journal of geology and geophysics, 18*(2), 259-272.

Cole, J. W. (1978). Distribution, petrography, and chemistry of Kiwitahi and Maungatautari volcanics, North Island, New Zealand. *New Zealand Journal of Geology and Geophysics, 21*(2), 143-153.

Cole, J. W. (1986). Distribution and tectonic setting of late cenozoic volcanism in New Zealand. In I. E. M. Smith (Ed.), *Late cenozoic volcanism in New Zealand* (pp. 7-20). Wellington, New Zealand: Royal Society of New Zealand Bulletin 23.

Cole, P., Calder, E., Sparks, R., Clarke, A., Druitt, T., Young, S., Herd, R., Harford, C., & Norton, G. (2002). Deposits from dome-collapse and fountain-collapse pyroclastic flows at Soufrière Hills Volcano, Montserrat. *Geological Society, London, Memoirs, 21*(1), 231-262.

Cook, C., Briggs, R. M., Smith, I. E. M., & Maas, R. (2005). Petrology and geochemistry of intraplate basalts in the South Auckland Volcanic Field, New Zealand: evidence for two coeval magma suites from distinct sources. *Journal of Petrology, 46*(3), 473-503.

Cowlyn, J. D. (2016). *Pyroclastic density currents at Ruapehu volcano; New Zealand.* Thesis, University of Canterbury, Christchurch, New Zealand.

Cullity, B. D., & Stock, S. (2001). *Elements of X-ray diffraction*. (3rd ed.). Upper Saddle River, N.J.: Prentice Hall.

de Silva, S., Salas, G., & Schubring, S. (2008). Triggering explosive eruptions—The case for silicic magma recharge at Huaynaputina, southern Peru. *Geology, 36*(5), 387-390.

De Vries, B. V. W., & Francis, P. (1997). Catastrophic collapse at stratovolcanoes induced by gradual volcano spreading. *Nature, 387*(6631), 387.

Downey, W. S., Kellett, R. J., Smith, I. E. M., Price, R. C., & Stewart, R. B. (1994). New palaeomagnetic evidence for the recent eruptive activity of Mt. Taranaki, New Zealand. *Journal of Volcanology and Geothermal Research, 60*(1), 15-27.

Dufek, J., Esposti Ongaro, T., & Roche, O. (2015). Chapter 35 - Pyroclastic Density Currents: Processes and Models A2 - Sigurdsson, Haraldur. In *The Encyclopedia of Volcanoes (Second Edition)* (pp. 617-629). Amsterdam: Academic Press.

Edbrooke, S. W. (2001). *Geology of the Auckland area. 1:250,000 Geological Map, 3.* Lower Hutt, New Zealand: Institute of Geological and Nucear Sciences.

Eggins, S. M. (2003). Laser ablation ICP-MS analysis of geological materials prepared as lithium borate glasses. *Geostandards and Geoanalytical Research, 27*(2), 147-162.

Froude, D., & Cole, J. (1985). Petrography, mineralogy and chemistry of Titiraupenga volcano, North Island, New Zealand. *New Zealand journal of geology and geophysics, 28*(3), 487-496.

Furlong, K. P., & Kamp, P. J. J. (2009). The lithospheric geodynamics of plate boundary transpression in New Zealand: Initiating and emplacing subduction along the Hikurangi margin, and the tectonic evolution of the Alpine Fault system. *Tectonophysics, 474*(3-4), 449-462.

Gaylord, D. R., & Neall, V. E. (2012). Subedifice collapse of an andesitic stratovolcano: The Maitahi Formation, Taranaki Peninsula, New Zealand. *Geological Society of America Bulletin, 124*(1-2), 181-199.

Giba, M., Nicol, A., & Walsh, J. J. (2010). Evolution of faulting and volcanism in a back-arc basin and its implications for subduction processes. *Tectonics, 29*(4), n/a-n/a.

Giba, M., Walsh, J. J., Nicol, A., Mouslopoulou, V., & Seebeck, H. (2013). Investigation of the spatio-temporal relationship between normal faulting and arc volcanism on million-year time scales. *Journal of the Geological Society, 170*(6), 951-962.

Gill, J. B. (1981). *Orogenic andesites and plate tectonics*. Berlin ; New York: Berlin; New York : Springer-Verlag.

Gill, R. (2010). *Igneous rocks and processes : a practical guide*. Chichester, West Sussex, UK: Wiley-Blackwell.

Glicken, H. (1990). The rockslide-debris avalanche of the May 18, 1980, eruption of Mount St. Helens — 10th Anniversary Perspectives. *1990*.

Gold discovery at Maungatautari. (1887, September 24th). *The Aroha and Ohinemuri News,* p. 5.

Goles, G. G., Briggs, R. M., & Rosenberg, M. D. (1996). Late Pliocene stratigraphic succession and volcanic evolution of Karioi volcano, western North Island, New Zealand. *New Zealand Journal of Geology and Geophysics, 39*(2), 283-294.

Graham, I. J., Science, G. N. S., & Geological Society of New, Z. (2008). *A continent on the move: New Zealand geoscience into the 21st century*. (Vol. no. 124.). Wellington, NZ: Geological Society of New Zealand in association with GNS Science.

Haase, C., Chadam, J., Feinn, D., & Ortoleva, P. (1980). Oscillatory zoning in plagioclase feldspar. *Science, 209*(4453), 272-274.

Hayward, B. W., Black, P. M., Smith, I. E. M., Ballance, P. F., Itaya, T., Doi, M., Takagi, M., Bergman, S., Adams, C. J., Herzer, R. H., & Robertson, D. J. (2001). K-Ar ages of early miocene arc-type volcanoes in northern New Zealand. *New Zealand Journal of Geology and Geophysics, 44*(2), 285-311.

Healy, J., Schofield, J., & Thompson, B. (1964). *Sheet 5 Rotorua*. Geological Map of New Zealand 1:250 000. Wellington: Department of Scientific and Industrial Research.

Hedenquist, J. W. (1995). The ascent of magmatic fluid: discharge versus mineralization. *Magmas, Fluids and Ore Deposits: Mineralogical Association of Canada Short Course Series, 23*, 263-289.

Heming, R. F. (1980). Patterns of quaternary basaltic volcanism in the northern North Island, New Zealand. *New Zealand Journal of Geology and Geophysics, 23*(3), 335-344.

Herzer, R. H. (1995). Seismic stratigraphy of a buried volcanic arc, Northland, New Zealand and implications for neogene subduction. *Marine and Petroleum Geology, 12*(5), 511-531.

Herzer, R. H., Barker, D. H. N., Roest, W. R., & Mortimer, N. (2011). Oligocene-miocene spreading history of the northern South Fiji Basin and implications for the evolution of the New Zealand plate boundary. *Geochemistry, Geophysics, Geosystems, 12*(2), n/a-n/a.

Herzer, R. H., Davy, B. W., Mortimer, N., Quilty, P. G., Chaproniere, G. C. H., Jones, C. M., Crawford, A. J., & Hollis, C. J. (2009). Seismic stratigraphy and structure of the Northland Plateau and the development of the Vening Meinesz transform margin, SW Pacific Ocean. *Marine Geophysical Researches, 30*(1), 21-60.

Herzer, R. H., & Mascle, J. (1996). Anatomy of a continent-backarc transform — the Vening Meinesz Fracture Zone northwest of New Zealand. *Marine Geophysical Researches, 18*(2), 401-427.

Hildreth, W., & Lanphere, M. A. (1994). Potassium-argon geochronology of a basalt-andesite-dacite arc system: The Mount Adams volcanic field, Cascade Range of southern Washington. *Geological Society of America Bulletin, 106*(11), 1413-1429.

Hobden, B., Houghton, B., Lanphere, M., & Nairn, I. (1996). Growth of the Tongariro volcanic complex: new evidence from K-Ar age determinations.

Huang, Y., Hawkesworth, C., Smith, I., van Calsteren, P., & Black, P. (2000). Geochemistry of late cenozoic basaltic volcanism in Northland and Coromandel, New Zealand: implications for mantle enrichment processes. *Chemical Geology, 164*(3), 219-238.

Ito, E., White, W. M., & Göpel, C. (1987). The O, Sr, Nd and Pb isotope geochemistry of MORB. *Chemical Geology, 62*(3-4), 157-176.

Jochum, K. P., Nohl, U., Herwig, K., Lammel, E., Stoll, B., & Hofmann, A. W. (2005). GeoReM: A new geochemical database for reference materials and isotopic standards. *Geostandards and Geoanalytical Research, 29*(3), 333-338.

Kear, D. (1964). Volcanic alignments north and west of New Zealand's Central Volcanic Region. *New Zealand Journal of Geology and Geophysics, 7*(1), 24-44.

Kear, D. (1994). A “least complex” dynamic model for late cenozoic volcanism in the North Island, New Zealand. *New Zealand journal of geology and geophysics, 37*(2), 223-236.

Kelemen, P. B. (1995). Genesis of high Mg# andesites and the continental crust. *Contributions to Mineralogy and Petrology, 120*(1), 1-19.

Kelemen, P. B., Hanghøj, K., & Greene, A. R. (2013). Chapter 4.21 - One view of the geochemistry of subduction-related magmatic arcs, with an emphasis on primitive andesite and lower crust. In K. K. Turekian (Ed.), *Treatise on Geochemistry (Second Edition)* (pp. 749-806). Oxford: Elsevier.

Kelemen, P. B., Shimizu, N., & Dunn, T. (1993). Relative depletion of niobium in some arc magmas and the continental crust: partitioning of K, Nb, La and

Ce during melt/rock reaction in the upper mantle. *Earth and Planetary Science Letters, 120*(3), 111-134.

Keys, H. J., & Green, P. M. (2008). Ruapehu lahar New Zealand 18 March 2007: lessons for hazard assessment and risk mitigation 1995–2007. *Journal of Disaster Research, 3*(4), 284-296.

King, P. R. (2000). Tectonic reconstructions of New Zealand: 40 Ma to the present. *New Zealand Journal of Geology and Geophysics, 43*(4), 611-638.

King, P. R., & Thrasher, G. P. (1996). *Cretaceous-Cenozoic geology and petroleum systems of the Taranaki Basin, New Zealand*. Lower Hutt, N.Z.: Lower Hutt, N.Z. : Institute of Geological & Nuclear Sciences Limited.

Krippner, S. J. P., Briggs, R. M., Wilson, C. J. N., & Cole, J. W. (1998). Petrography and geochemistry of lithic fragments in ignimbrites from the Mangakino Volcanic Centre: Implications for the composition of the subvolcanic crust in western Taupo Volcanic Zone, New Zealand. *New Zealand Journal of Geology and Geophysics, 41*(2), 187-199.

Land Information New Zealand. (n.d.). *LINZ Data Service*. Retrieved May, 2017, from https://data.linz.govt.nz/.

Le Maitre, R. W., Streckeisen, A., Zanettin, B., Le Bas, M., Bonin, B., & Bateman, P. (2002). *Igneous rocks: a classification and glossary of terms: recommendations of the International Union of Geological Sciences Subcommission on the Systematics of Igneous Rocks*. Cambridge University Press.

Leonard, G. S., Begg, J. G., & Wilson, C. J. N. (2010). *Geology of the Rotorua area. Institute of Geological and Nuclear Sciences 1:250 000 geological map 5. 1 sheet + 102 p.* Lower Hutt, New Zeland: GNS Science.

Lindsay, J., Worthington, T., Smith, I. M., & Black, P. (1999). Geology, petrology, and petrogenesis of Little Barrier Island, Hauraki Gulf, New Zealand. *New Zealand Journal of Geology and Geophysics, 42*(2), 155-168.

Maro, G., & Caffe, P. J. (2016). The Cerro Bitiche andesitic field: petrological diversity and implications for magmatic evolution of mafic volcanic centers from the northern Puna. *Bulletin of Volcanology, 78*(7), 51.

Maungatautari Ecological Island Trust. (2010). *Welcome*. Retrieved April 8, 2016, from http://www.maungatrust.org/Index.cfm.

McDonough, W. F., Sun, S. S., Ringwood, A. E., Jagoutz, E., & Hofmann, A. W. (1992). Potassium, rubidium, and cesium in the Earth and Moon and the evolution of the mantle of the Earth. *Geochimica et Cosmochimica Acta, 56*(3), 1001-1012.

Mortimer, N. (2008). Remnants of a distant past. In I. J. Graham (Ed.), *A continent on the move: New Zealand geosciences into the 21st century* (pp. 75-79). Wellington, New Zealand: Geological Society of New Zealand in association with GNS Science.

Mortimer, N., Herzer, R. H., Gans, P. B., Laporte-Magoni, C., Calvert, A. T., & Bosch, D. (2007). Oligocene–miocene tectonic evolution of the South Fiji Basin and Northland Plateau, SW Pacific Ocean: Evidence from petrology and dating of dredged rocks. *Marine Geology, 237*(1–2), 1-24.

Neal, C. R., & Taylor, L. A. (1989). A negative Ce anomaly in a peridotite xenolith: evidence for crustal recycling into the mantle or mantle metasomatism? *Geochimica et Cosmochimica Acta, 53*(5), 1035-1040.

Olissoff, E. S. (1981). *Quaternary stratigraphy and ignimbrites of the Karapiro-Arapuni region.* thesis, Thesis (M. Sc. Earth Sciences) -- University of Waikato, 1981.

Olson, O. P. (1950). *Geology of the Maungatautari area, south-east of Cambridge.* thesis, University of Auckland, Auckland, New Zealand.

Paguican, E. M. R., van Wyk de Vries, B., & Lagmay, A. M. F. (2014). Hummocks: how they form and how they evolve in rockslide-debris avalanches. *Landslides, 11*(1), 67-80.

Parfitt, L., & Wilson, L. (2008). *Fundamentals of Physical Volcanology*. Hoboken, GB: Wiley-Blackwell.

Pierson, T. C., Janda, R. J., Thouret, J.-C., & Borrero, C. A. (1990). Perturbation and melting of snow and ice by the 13 November 1985 eruption of Nevado del Ruiz, Colombia, and consequent mobilization, flow and deposition of lahars. *Journal of Volcanology and Geothermal Research, 41*(1), 17-66.

Pin, C., Gannoun, A., & Dupont, A. (2014). Rapid, simultaneous separation of Sr, Pb, and Nd by extraction chromatography prior to isotope ratios determination by TIMS and MC-ICP-MS. *Journal of Analytical Atomic Spectrometry, 29*(10), 1858-1870.

Plank, T. (2005). Constraints from thorium/lanthanum on sediment recycling at subduction zones and the evolution of the continents. *Journal of Petrology, 46*(5), 921-944.

Price, R., Mortimer, N., Smith, I., & Maas, R. (2015). Whole-rock geochemical reference data for Torlesse and Waipapa terranes, North Island, New Zealand. *New Zealand Journal of Geology and Geophysics, 58*(3), 213-228.

Price, R. C., Gamble, J. A., Smith, I. E., Maas, R., Waight, T., Stewart, R. B., & Woodhead, J. (2012). The anatomy of an andesite volcano: a time–

stratigraphic study of andesite petrogenesis and crustal evolution at Ruapehu Volcano, New Zealand. *Journal of Petrology, 53*(10), 2139-2189.

Price, R. C., Smith, I. E., Stewart, R. B., Gamble, J. A., Gruender, K., & Maas, R. (2016). High-K andesite petrogenesis and crustal evolution: Evidence from mafic and ultramafic xenoliths, Egmont Volcano (Mt. Taranaki) and comparisons with Ruapehu Volcano, North Island, New Zealand. *Geochimica et Cosmochimica Acta, 185*, 328-357.

Price, R. C., Stewart, R. B., Woodhead, J. D., & Smith, I. E. M. (1999). Petrogenesis of high-K arc magmas: Evidence from Egmont Volcano, North Island, New Zealand. *Journal of Petrology, 40*(1), 167-197.

Rafferty, W. J. (1977). *The volcanic geology and petrology of South Auckland.* thesis, University of Auckland, Auckland.

Rafferty, W. J., & Heming, R. F. (1979). Quaternary alkalic and sub-alkalic volcanism in South Auckland, New Zealand. *Contributions to Mineralogy and Petrology, 71*(2), 139-150.

Robertson, D. J. (1983). *Paleomagnetism and geochronology of volcanics in the northern North Island.* thesis, University of Auckland, Auckland, New Zealand.

Rowland, J., & Sibson, R. (2004). Structural controls on hydrothermal flow in a segmented rift system, Taupo Volcanic Zone, New Zealand. *Geofluids, 4*(4), 259-283.

Saucedo, R., Macías, J., & Bursik, M. (2004). Pyroclastic flow deposits of the 1991 eruption of Volcán de Colima, Mexico. *Bulletin of Volcanology, 66*(4), 291-306.

Seebeck, H., Nicol, A., Villamor, P., Ristau, J., & Pettinga, J. (2014). Structure and kinematics of the Taupo Rift, New Zealand. *Tectonics, 33*(6), 1178-1199.

Selby, M. J. (1993). *Hillslope materials and processes*. (2nd ed.. ed.). Oxford, England: Oxford, England : Oxford University Press.

Shea, T., de Vries, B. v. W., & Pilato, M. (2008). Emplacement mechanisms of contrasting debris avalanches at Volcán Mombacho (Nicaragua), provided by structural and facies analysis. *Bulletin of Volcanology, 70*(8), 899.

Siebert, L. (2002). Landslides resulting from structural failure of volcanoes. In S. G. Evans & J. V. DeGraff (Eds.), *Catastrophic landslides: Effects, occurrence, and mechanisms* (Vol. XV, pp. 209-235). Boulder, Colarado: Geological Society of America Reviews in Engineering Geology.

Simmons, S. F., White, N. C., & John, D. A. (2005). Geological characteristics of epithermal precious and base metal deposits. *Economic Geology 100th anniversary volume, 29*, 485-522.

Simpson, M. P., & Bignall, G. (2016). Undeveloped high-enthalpy geothermal fields of the Taupo Volcanic Zone, New Zealand. *Geothermics, 59*, 325-346.

Smith, I., & Briggs, R. (2008). Hot spots in the north. In I. J. Graham (Ed.), *A continent on the move* (pp. 158-161). Wellington, New Zealand: Geological Society of New Zealand in association with GNS Science.

Stern, C. R. (2004). Active Andean volcanism: its geologic and tectonic setting. *Revista geológica de Chile, 31*(2), 161-206.

Sulpizio, R., & Dellino, P. (2008). Sedimentology, depositional mechanisms and pulsating behaviour of pyroclastic density currents. *Developments in Volcanology, 10*, 57-96.

Sun, S.-S., & McDonough, W.-s. (1989). Chemical and isotopic systematics of oceanic basalts: implications for mantle composition and processes. *Geological Society, London, Special Publications, 42*(1), 313-345.

Thouret, J. C. (1999). Volcanic geomorphology—an overview. *Earth-Science Reviews, 47*(1–2), 95-131.

Timm, C., Hoernle, K., Werner, R., Hauff, F., den Bogaard, P. v., White, J., Mortimer, N., & Garbe-Schönberg, D. (2010). Temporal and geochemical evolution of the cenozoic intraplate volcanism of Zealandia. *Earth-Science Reviews, 98*(1–2), 38-64.

Torres-Orozco, R., Cronin, S. J., Pardo, N., & Palmer, A. S. (2017). New insights into holocene eruption episodes from proximal deposit sequences at Mt. Taranaki (Egmont), New Zealand. *Bulletin of Volcanology, 79*(1), 3.

Tost, M., Cronin, S., & Procter, J. (2014). Transport and emplacement mechanisms of channelised long-runout debris avalanches, Ruapehu volcano, New Zealand. *Bulletin of Volcanology, 76*(12), 881.

Vallance, J. W., & Iverson, R. M. (2015). Chapter 37 - Lahars and their deposits. In H. Sigurdsson (Ed.), *The Encyclopedia of Volcanoes (Second Edition)* (pp. 649-664). Amsterdam: Academic Press.

Vidal, N., & Merle, O. (2000). Reactivation of basement faults beneath volcanoes: a new model of flank collapse. *Journal of Volcanology and Geothermal Research, 99*(1), 9-26.

Waight, T. E., Troll, V. R., Gamble, J. A., Price, R. C., & Chadwick, J. P. (2017). Hf isotope evidence for variable slab input and crustal addition in basalts

and andesites of the Taupo Volcanic Zone, New Zealand. *Lithos, 284*, 222-236.

Waikato Regional Council. (n.d.). *Data Catalogue*. Retrieved May, 2017, from https://www.waikatoregion.govt.nz/services/data-catalogue/.

Weaver, S. D., & Smith, I. E. M. (1989). New Zealand intraplate volcanism. In R. W. Johnson (Ed.), *Intraplate volcanism* (pp. 157-187). Cambridge: Cambridge University Press.

White, N. C., & Hedenquist, J. W. (1995). Epithermal gold deposits: styles, characteristics and exploration. *SEG newsletter, 23*(1), 9-13.

Wilson, C. J. N., Charlier, B. L. A., Fagan, C. J., Spinks, K. D., Gravley, D. M., Simmons, S. F., & Browne, P. R. L. (2008). U–Pb dating of zircon in hydrothermally altered rocks as a correlation tool: Application to the Mangakino geothermal field, New Zealand. *Journal of Volcanology and Geothermal Research, 176*(2), 191-198.

Wilson, C. J. N., Houghton, B. F., McWilliams, M. O., Lanphere, M. A., Weaver, S. D., & Briggs, R. M. (1995). Volcanic and structural evolution of Taupo Volcanic Zone, New Zealand: a review. *Journal of Volcanology and Geothermal Research, 68*(1), 1-28.

Wilson, C. J. N., & Rowland, J. V. (2016). The volcanic, magmatic and tectonic setting of the Taupo Volcanic Zone, New Zealand, reviewed from a geothermal perspective. *Geothermics, 59, Part B*, 168-187.

Winchester, J. A., & Floyd, P. A. (1977). Geochemical discrimination of different magma series and their differentiation products using immobile elements. *Chemical Geology, 20*, 325-343.

Winter, J. D. (2014). *Principles of igneous and metamorphic petrology*. (2nd. ed. Pearson new international edition.. ed.). Harlow: Harlow : Pearson.

Zernack, A. V., Procter, J. N., & Cronin, S. J. (2009). Sedimentary signatures of cyclic growth and destruction of stratovolcanoes: A case study from Mt. Taranaki, New Zealand. *Sedimentary Geology, 220*(3), 288-305.

Appendix I:

Locality and Sample Catalogue

Sample ID	Waikato #	Locality #	Site description	Easting (NZTM)	Northing (NZTM)	Elevation (m)	Rock/Sample type	Analyses Undertaken					
								TS	PC	XRF	XRD	LA-ICP-MS	Sr/Nd Isotopes
KSC001	W161051	1	Kairangi Scoria Cone	1820519	5791745	158	Olivine basalt	√	√	√	x	√	√
KSC002	W161052	1	Kairangi Scoria Cone	1820520	5791750	220	Olivine basalt	√	x	√	x	√	x
KSC004	W161053	2	Farmers quarry in greywacke hill	1820147	5791889	95	Basement	x	x	x	x	x	x
GF005	W161054	3	Garland Farm	1822822	5790161	200	Hydrothermally altered	√	x	x	√	x	x
GF006	W161055	4	Garland Farm lava flow	1823889	5790096	362	Pyroxene andesite	√	√	√	x	√	√
GF007	W161056	5	Garland Farm	1823542	5789806	365	Pyroxene andesite	√	√	√	x	√	x
GF008	W161057	6	Garland Farm	1823369	5789942	311	Weathered	√	x	x	x	x	x
GF009	W161058	7	Garland Farm	1821809	5790347	276	Basement	√	x	x	x	x	x
MSE010	W161059	8	Maungatautari Enclosure, vertical overhang	1826810	5788444	-	Hornblende dacite	√	√	√	x	√	x
MSE011	W161060	9	Maungatautari Enclosure, stream outcrop	1826753	5788409	-	Hydrothermally altered	√	x	√	√	x	x
MSE012	W161061	9	Maungatautari Enclosure, goldmine	1826753	5788409	-	Hydrothermally altered	√	x	√	√	x	x
MSE013	W161062	9	Maungatautari Enclosure, goldmine	1826753	5788409	-	Hydrothermally altered	√	x	√	x	x	x
MSE014	W161063	9	Maungatautari Enclosure, goldmine	1826753	5788409	-	Hydrothermally altered	√	x	√	√	x	x
KH015	W161064	10	Kairangi Hill	1819842	5790491	-	Basement	√	x	x	x	x	x
GF016	W161065	11	Garland Farm waterfall	1821820	5789696	-	Basement	√	x	x	x	x	x
MSE017	W161066	12	Maungatautari Enclosure, boulder	1824916	5789338	-	Pyroxene andesite	√	√	√	x	√	x
MSE018	W161067	13	Maungatautari Enclosure, Little Rock Peak	1824948	5789743	-	Hornblende dacite	√	√	√	x	√	x
MSE019	W161068	14	Maungatautari Enclosure, Little Rock Base	1824884	5789754	-	Hornblende dacite	√	√	√	x	√	x

Appendix I: Locality and sample catalogue (continued).

Sample ID	Waikato #	Locality #	Site description	Easting (NZTM)	Northing (NZTM)	Elevation (m)	Rock/Sample type	Analyses Undertaken					
								TS	PC	XRF	XRD	LA-ICP-MS	Sr/Nd Isotopes
MRd020	W161069	15	Maru Rd	1823377	5786102	-	Labradorite andesite	√	√	x	x	√	√
MRd021	W161070	16	Maru Rd	1823469	5785891	-	Labradorite andesite	√	x	√	x	x	x
MRd022	W161071	17	Maru Rd	1823078	5785625	-	Labradorite andesite	√	√	√	x	√	x
MSE023	W161072	18	Maungatautari Enclosure, track cutting	1824991	5786351	516	Weathered	√	x	x	x	x	x
MSE024	W161073	19	Maungatautari Enclosure, Quarry #34	1825171	5787245	613	Bulk at 30 cm	√	x	x	x	x	x
MSE025	W161074	19	Maungatautari Enclosure, Quarry #34	1825171	5787245	613	Yellow clast	x	x	x	x	x	x
MSE026	W161075	19	Maungatautari Enclosure, Quarry #34	1825171	5787245	613	Bulk at 90 cm	√	x	x	x	x	x
MSE027	W161076	19	Maungatautari Enclosure, Quarry #34	1825171	5787245	613	Yellow clast	√	x	x	x	x	x
MSE028	W161077	19	Maungatautari Enclosure, Quarry #34	1825171	5787245	613	Dense brick red clast	√	x	x	x	x	x
MSE029	W161078	19	Maungatautari Enclosure, Quarry #34	1825171	5787245	613	Orange porphyritic clast	√	x	x	x	x	x
MSE030	W161079	19	Maungatautari Enclosure, Quarry #34	1825171	5787245	613	Purple/red clast	√	x	x	x	x	x
MSE031	W161080	19	Maungatautari Enclosure, Quarry #34	1825171	5787245	613	Grey porphyritic clast	√	x	x	x	x	x
MSE032	W161081	19	Maungatautari Enclosure, Quarry #34	1825171	5787245	613	Assorted small lithics	x	x	x	x	x	x
MSE033	W161082	19	Maungatautari Enclosure, Quarry #34	1825171	5787245	613	Bulk at 2 m	√	x	x	x	x	x
MSE034	W161083	19	Maungatautari Enclosure, Quarry #34	1825171	5787245	613	Bulk at 3.2 m	√	x	x	x	x	x

Appendix I: Locality and sample catalogue (continued).

Sample ID	Waikato #	Locality #	Site description	Easting (NZTM)	Northing (NZTM)	Elevation (m)	Rock/Sample type	Analyses Undertaken					
								TS	PC	XRF	XRD	LA-ICP-MS	Sr/Nd Isotopes
MSE035	W161084	19	Maungatautari Enclosure, Quarry #34	1825171	5787245	613	Bulk at 4.1 m	√	x	x	x	x	x
MSE036	W161085	19	Maungatautari Enclosure, Quarry #34	1825171	5787245	613	Bulk at 4.35 m	√	x	x	x	x	x
MSE037	W161086	19	Maungatautari Enclosure, Quarry #34	1825171	5787245	613	Bulk at 5 m	√	x	x	x	x	x
PH038	W161087	20	Pukekura Hill	1820729	5796767	306	Basement	√	x	x	x	x	x
ORE039b	W161088	21	Oreipunga Cone	1830124	5787184	311	Hornblende dacite	√	√	√	x	√	√
ORE040	W161089	22	Oreipunga Cone, gully	1828633	5786950	386	Hornblende andesite	√	√	√	x	√	√
ORE041	W161090	24	Ignimbrite bluffs	1831136	5786929	205	Rocky Hill Ignimbrite	√	x	x	x	x	x
HF043	W161091	26	Hicks Farm, track cutting	1825509	5791213	331	Hornblende andesite	√	√	√	x	√	x
HF044	W161092	27	Hicks Farm lava flow	1825178	5790935	457	Hornblende andesite	√	√	√	x	√	x
MSE045	W161093	28	Maungatautari Enclosure, Quarry #58	1825594	5788373	660	Labradorite andesite	√	x	√	x	√	x
MSE046	W161094	28	Maungatautari Enclosure, Quarry #58	1825594	5788373	660	Labradorite andesite	√	x	√	x	x	x
MSE047	W161095	28	Maungatautari Enclosure, Quarry #58	1825594	5788373	660	Labradorite andesite	√	x	√	x	x	x
MSE048	W161096	30	Maungatautari Enclosure, Summit quarry	1825820	5789190	795	Bulk at 1 m	√	x	x	x	x	x
MSE049	W161097	30	Maungatautari Enclosure, Summit quarry	1825820	5789190	795	Porphyritic lava lithic	√	x	x	x	x	x
MSE050	W161098	30	Maungatautari Enclosure, Summit quarry	1825820	5789190	795	Bulk at 2.2 m	√	x	x	x	x	x
MSE051	W161099	30	Maungatautari Enclosure, Summit quarry	1825820	5789190	795	Andesitic blocks	√	x	x	x	x	x

Appendix I: Locality and sample catalogue (continued).

Sample ID	Waikato #	Locality #	Site description	Easting (NZTM)	Northing (NZTM)	Elevation (m)	Rock/Sample type	Analyses Undertaken					
								TS	PC	XRF	XRD	LA-ICP-MS	Sr/Nd Isotopes
MSE052	W161100	30	Maungatautari Enclosure, Summit quarry	1825820	5789190	795	Bulk at ground level	√	x	x	x	x	x
MSE053	W161101	30	Maungatautari Enclosure, Summit quarry	1825820	5789190	795	Pyroxene andesite	√	√	√	x	√	x
MSE054	W161102	31	Maungatautari Enclosure, Quarry #45	1825456	5787687	648	Pyroxene andesite	√	√	√	x	√	x
MSE055	W161103	32	Maungatautari Enclosure, track cutting	1825656	5787418	678	Weathered rock	√	x	√	x	x	x
MSE056	W161104	33	Maungatautari Enclosure, Pukeatua Peak	1825752	5787356	766	Hornblende dacite	√	√	√	x	√	x
MSE057	W161105	34	Maungatautari Enclosure, Rocky Outcrop	1825495	5787267	727	Hornblende dacite	√	√	√	x	√	x
SF058	W161106	35	Scott Farm	1830123	5789474	268	Basement	√	x	x	x	x	x
SF059	W161107	35	Scott Farm	1830123	5789474	268	Weathered rock	√	x	√	x	x	x
SF060	W161108	35	Scott Farm	1830123	5789474	268	Hornblende andesite	√	√	√	x	√	x
SF061	W161109	35	Scott Farm	1830123	5789474	268	Weathered rock	√	√	x	x	x	x
MSE062	W161110	39	Maungatautari Enclosure, Trig	1826127	5788957	822	Hornblende andesite	√	x	√	√	√	x
MSE063	W161111	39	Maungatautari Enclosure, Trig	1826127	5788957	822	Hornblende andesite/ weathered	√	x	√	√	x	x

TS = thin section; PC = point counting; XRF = X-ray fluorescence spectrometry; XRD = X-ray powder diffraction; LA-ICP-MS = Laser Ablation Inductively Coupled Plasma Mass Spectrometry.

Appendix II:

Peak numbers for mineral phase identification in XRD

Appendix II: d values and intensities for the three strongest peaks of each mineral phase identified in XRD traces

Mineral Name	°2θ	Å	I (%)	Mineral Name	°2θ	Å	I (%)
Cristobalite				*Albite*			
d_1	21.93	4.04	100	d_1	27.8	3.20	100
d_2	36.12	2.48	20	d_2	21.95	4.04	67
d_3	31.46	2.84	13	d_3	23.67	3.75	45
Tridymite				*K-feldspar*			
d_1	21.62	4.1	100	d_1	27.33	3.26	100
d_2	20.50	4.33	90	d_2	27.68	3.22	90
d_3	32.28	3.82	50	d_3	23.96	3.77	75
Quartz				*Amphibole*			
d_1	26.65	3.34	100	d_1	33.03	2.70	100
d_2	20.85	4.26	22	d_2	28.69	3.11	83
d_3	50.14	1.82	14				
Alunite				*Augite*			
d_1	29.90	2.98	100	d_1	29.86	2.99	100
d_2	17.90	4.95	51	d_2	35.54	2.52	42
d_3	39.56	2.28	30	d_3	30.34	2.94	32
Kaolinite				*Hematite*			
d_1	12.33	7.17	100	d_1	33.25	2.69	100
d_2	62.26	1.49	90	d_2	54.02	1.69	60
d_3	24.85	3.58	80	d_3	35.74	2.51	50
Labradorite				*Opal*			
d_1	28.04	3.18	100	d_1	21.78	4.07	100
d_2	27.77	3.21	70	d_2	20.60	4.30	60
d_3	23.64	3.76	70	d_3	35.94	2.49	23

Appendix III:

Raw XRF Geochemical Data

Sample Name	**KSC001**	**KSC002**	**GF006**	**GF007**	**MSE010**	**MSE013**	**MSE017**	**MSE018**	**MSE019**
Major elements (XRF, wt.%)									
(Raw data; all Fe expressed as Fe_2O_3)									
SiO_2	48.90	49.04	59.54	60.08	61.42	60.38	58.66	61.65	62.33
Al_2O_3	14.39	14.27	16.23	16.46	16.97	17.58	16.17	17.17	16.75
TiO_2	1.48	1.48	0.66	0.65	0.56	0.64	0.76	0.46	0.48
MnO	0.17	0.16	0.11	0.12	0.09	0.02	0.14	0.09	0.11
Fe_2O_3	10.71	10.64	7.09	6.83	5.95	4.81	7.54	5.93	5.80
Na_2O	2.87	2.87	3.24	3.42	3.22	2.59	3.28	3.32	3.60
MgO	8.42	8.42	3.25	3.29	1.47	1.67	3.61	1.82	2.01
K_2O	1.34	1.31	2.00	2.01	2.07	2.28	1.97	2.13	2.09
CaO	9.85	10.13	5.79	6.27	4.67	2.42	6.42	4.19	5.13
P_2O_5	0.35	0.35	0.21	0.21	0.14	0.10	0.22	0.21	0.22
LOI (%)	0.62	0.69	1.72	0.92	3.60	7.23	1.48	3.35	1.72
Sum (%)	99.40	99.68	100.06	100.50	100.50	101.48	100.46	100.52	100.43
Trace elements (XRF, ppm)									
F	221	308	96	115	350	222	166	86	63
S	-	12	-	-	262	15014	-	81	-
Cl	290	292	197	217	1065	367	211	176	224
Sc	22	22	16	15	16	16	15	10	11
V	243	245	135	132	112	149	154	80	86
Cr	450	475	42	42	18	27	62	8	8
Co	48	49	22	22	28	31	26	14	18
Ni	147	150	18	21	15	14	27	10	8
Cu	47	47	112	53	33	28	44	24	24
Zn	83	86	58	56	61	29	62	49	50
Ga	20	19	20	18	19	19	19	21	19
As	5	6	5	5	5	13	5	4	6
Rb	35	33	76	71	56	73	70	76	74
Sr	524	530	436	468	402	288	456	372	437
Y	24	30	39	34	16	15	20	16	18
Zr	151	146	161	157	152	160	157	159	152
Nb	24	23	10	9	8	8	10	9	9
Mo	4	4	4	4	4	4	4	4	4
Sn	-	2	-	1	2	1	1	-	2
Sb	-	-	-	-	1	-	-	1	1
Cs	12	12	7	7	6	7	7	6	6
Ba	453	488	634	688	650	977	611	772	737
La	26	37	53	43	16	15	24	12	19
Ce	62	48	66	56	46	41	52	43	47
Nd	25	27	47	30	22	18	23	18	28
Tl	-	-	-	-	-	-	-	-	-
Pb	3	3	3	5	7	7	3	7	5
Th	6	6	10	9	10	11	9	10	9
U	3	3	3	3	3	3	3	3	3

Appendix III: Raw XRF geochemical data (continued).

Sample Name	MSE019	MRd20	MRd21	MRd22	MSE027	ORE039B	MSE40	HF043	HF044
Major elements (XRF, wt.%)									
(Raw data; all Fe expressed as Fe_2O_3)									
SiO_2	62.33	61.38	60.88	57.57	44.96	62.15	57.68	57.82	56.89
Al_2O_3	16.75	17.24	17.50	17.31	22.82	17.71	17.20	16.78	17.29
TiO_2	0.48	0.65	0.58	0.67	0.73	0.57	0.69	0.67	0.66
MnO	0.11	0.11	0.10	0.12	0.13	0.14	0.13	0.20	0.15
Fe_2O_3	5.80	5.89	5.84	7.84	7.97	6.43	7.78	7.80	7.88
Na_2O	3.60	3.67	3.71	3.21	2.32	3.34	3.14	3.12	2.83
MgO	2.01	2.53	1.62	3.36	3.11	0.65	3.42	3.66	3.72
K_2O	2.09	1.97	1.94	1.89	0.59	2.36	1.93	1.92	1.90
CaO	5.13	5.60	5.99	6.60	5.20	3.99	6.00	6.73	5.88
P_2O_5	0.22	0.23	0.22	0.23	0.30	0.25	0.22	0.20	0.22
LOI (%)	1.72	1.31	?	1.63	12.17	2.84	2.03	1.58	3.18
Sum (%)	100.43	100.78	98.61	100.65	100.70	100.82	100.51	100.72	100.88
Trace elements (XRF, ppm)									
F	63	254	192	115	15	92	117	12	70
S	-	-	-	-	1268	865	276	-	-
Cl	224	224	203	230	670	1018	569	295	441
Sc	11	12	13	15	13	12	16	18	16
V	86	131	120	153	131	119	160	161	162
Cr	8	4	28	23	6	6	17	37	117
Co	18	25	24	27	19	34	25	42	27
Ni	8	10	15	12	12	11	14	19	27
Cu	24	25	29	30	52	25	40	41	44
Zn	50	66	53	62	84	65	71	69	64
Ga	19	19	19	20	25	20	20	18	20
As	6	5	6	6	5	5	5	6	5
Rb	74	67	75	69	22	86	69	70	70
Sr	437	421	466	454	402	414	368	399	363
Y	18	21	23	22	20	24	93	74	166
Zr	152	155	141	145	226	178	139	147	144
Nb	9	8	8	8	11	9	8	8	8
Mo	4	4	4	4	5	4	4	4	4
Sn	2	2	2	-	2	3	-	-	-
Sb	1	-	2	-	-	-	-	-	-
Cs	6	6	7	7	6	2	7	6	9
Ba	737	644	702	561	889	713	798	726	709
La	19	19	21	18	12	29	41	62	160
Ce	47	56	53	48	46	55	43	65	71
Nd	28	23	20	22	22	26	53	65	130
Tl	-	-	-	-	-	-	-	-	-
Pb	5	3	5	4	9	6	4	5	5
Th	9	7	8	7	16	11	8	7	8
U	3	3	3	3	3	3	3	3	3

Sample Name	**MSE045**	**MSE046**	**MSE047**	**MSE053**	**MSE054**	**MSE055**	**MSE056**	**MSE057**
Major elements (XRF, wt.%)								
(Raw data; all Fe expressed as Fe_2O_3)								
SiO_2	57.69	56.34	56.03	56.85	58.18	63.31	61.19	63.72
Al_2O_3	17.80	18.07	18.33	17.51	17.38	17.46	17.29	16.16
TiO_2	0.66	0.64	0.68	0.69	0.75	0.44	0.50	0.50
MnO	0.10	0.12	0.13	0.13	0.10	0.10	0.09	0.05
Fe_2O_3	6.95	7.44	7.32	8.27	7.07	4.62	5.76	4.92
Na_2O	2.83	2.39	2.31	3.14	3.23	2.40	3.10	3.28
MgO	2.79	2.59	2.59	3.66	3.30	1.02	1.89	1.06
K_2O	2.05	2.11	2.12	1.87	1.93	2.79	2.27	2.65
CaO	4.46	3.40	3.08	6.80	6.72	1.85	3.54	3.39
P_2O_5	0.21	0.21	0.22	0.24	0.24	0.12	0.18	0.16
LOI (%)	5.11	7.17	8.00	1.64	1.73	6.43	4.05	3.75
Sum (%)	100.86	100.71	101.02	101.00	100.85	100.76	100.03	99.88
Trace elements (XRF, ppm)								
F	124	40	-	100	165	55	107	242
S	56	276	93	-	-	124	-	-
Cl	267	412	305	240	157	166	110	211
Sc	14	16	15	16	17	10	12	9
V	150	144	151	162	173	83	91	83
Cr	30	28	1	15	16	3	4	9
Co	24	20	23	25	25	13	14	17
Ni	7	8	10	16	13	8	8	9
Cu	21	30	24	45	31	23	28	26
Zn	67	72	70	66	68	230	57	61
Ga	19	20	21	20	20	19	19	18
As	5	5	4	5	4	5	4	5
Rb	72	74	76	66	65	109	84	103
Sr	305	242	219	468	459	203	322	358
Y	21	22	21	20	19	17	21	20
Zr	147	155	156	148	145	134	150	177
Nb	8	7	8	7	7	10	8	11
Mo	4	4	4	4	4	4	4	5
Sn	2	-	2	1	1	2	2	3
Sb	-	-	1	-	-	-	1	1
Cs	6	6	6	7	7	-	5	5
Ba	734	738	833	556	564	844	722	845
La	18	18	20	15	21	14	26	33
Ce	44	41	45	48	41	44	50	58
Nd	21	22	21	19	23	20	29	29
Tl	-	1	1	-	-	1	-	-
Pb	3	12	18	6	4	46	6	7
Th	8	8	10	8	7	9	10	14
U	3	3	3	3	3	3	3	3

Sample Name	**MSE057**	**SF059**	**SF060**	**MSE062**	**MSE063**
Major elements (XRF, wt.%)					
(Raw data; all Fe expressed as Fe_2O_3)					
SiO_2	63.72	52.67	57.54	59.95	56.35
Al_2O_3	16.16	15.59	17.87	17.84	19.04
TiO_2	0.50	0.58	0.65	0.55	0.64
MnO	0.05	0.13	0.15	0.13	0.15
Fe_2O_3	4.92	6.51	7.65	6.88	7.93
Na_2O	3.28	3.12	2.88	3.08	2.85
MgO	1.06	2.58	2.99	1.73	2.44
K_2O	2.65	1.72	1.99	2.21	1.90
CaO	3.39	5.64	4.71	3.99	3.76
P_2O_5	0.16	0.19	0.22	0.23	0.22
LOI (%)	3.75	11.98	4.15	4.09	5.51
Sum (%)	99.88	100.89	100.99	100.88	100.97
Trace elements (XRF, ppm)					
F	242	-	11	-	-
S	-	-	-	-	5
Cl	211	193	174	227	86
Sc	9	14	16	12	14
V	83	129	151	130	55
Cr	9	10	31	5	22
Co	17	22	23	23	18
Ni	9	9	11	12	15
Cu	26	28	31	15	29
Zn	61	55	63	61	76
Ga	18	17	20	19	20
As	5	4	6	5	9
Rb	103	60	68	80	54
Sr	358	393	326	400	396
Y	20	22	17	17	19
Zr	177	129	151	170	165
Nb	11	7	8	8	7
Mo	5	4	4	4	4
Sn	3	-	2	1	1
Sb	1	-	1	1	1
Cs	5	6	6	2	2
Ba	845	573	651	716	704
La	33	23	12	19	21
Ce	58	41	47	42	46
Nd	29	26	15	18	23
Tl	-	-	2	-	-
Pb	7	3	5	3	7
Th	14	7	10	10	11
U	3	3	3	3	3

Appendix IV:

LA-ICP-MS Specifications, Raw Data and Statistical Comparison with Standards

Instrument settings for LA-ICP-MS		
ICP-MS		
Model		Elan 6100 DRCII ICP-MS (Perkin Elmer Sciex)
Gas flows	Plasma (Ar)	15 L.min
	Auxiliary (Ar)	1.2 L.min
	Carrier (He)	1.0 L.min
	Nebuliser	0.6 to 0.7 optimised range
Shield torch		Used for most analyses
Vacuum pressure		1 x 10^{-5} Torr
Software		Elan 3.4
LASER		
Model		RESOlution SE series excimer laser
Wavelength		193 nm
Repetition rate		5 Hz
Pre-ablation laser warm-up		Laser fired continuously
Spot size		30 µm (60 for NIST)
Incident pulse energy		c. 0.04 mJ
Energy density on sample (fluence)		c. 6 J.cm^2
Software		Geostar v8.50
DATA ACQUISITION PARAMETERS		
Data acquisition protocol		Time resolved analyses
Scanning mode		Peak hopping, 1 point per peak
Detector mode		Pulse counting, dead time correction applied
Isotopes determined		Al_{27}, Si_{28}, K_{39}, Sc_{45}, Ti_{47}, V_{51}, Rb_{85}, Sr_{88}, Y_{89}, Zr_{90}, Nb_{93}, Sn_{118}, Cs_{133}, Ba_{138}, La_{139}, Ce_{140}, Pr_{141}, Nd_{142}, Sm_{152}, Eu_{153}, Gd_{158}, Dy_{164}, Ho_{165}, Er_{166}, Yb_{174}, Lu_{175}, Pb_{208}, Th_{232}, U_{238}.
Dwell time per isotope		10 ms (Al, Si, K) and 50 ms (all other elements)
Quadrapole settling time		c. 2 ms
Data acquisition		85 s (40 s background, 45 s ablation)
Software		Elan 3.4

Sample:	**NIST612-1**	**NIST612-2**	**NIST612-3**	**NIST612-4**	**NIST612-5**	**StHs-1**	**StHs-2**	**ML3-1**
Major element concentrations (ppm)								
Al	10980	11390	11210	11180	11110	95600	96100	72690
Al (2σ)	160	150	130	120	110	1400	1300	870
K	66.4	66.4	66	65.8	67	14240	14510	3177
K (2σ)	1.5	1	1.3	1.6	1.7	290	190	48
Ti	45.3	41.5	43.5	44.7	44.2	4081	4220	12040
Ti (2σ)	1.4	1.6	1.6	1.3	1.9	60	66	180
Trace element concentrations (ppm)								
Sc	41.76	40.13	40.56	41.48	41.06	10.18	10.15	29.68
Sc (2σ)	0.66	0.66	0.65	0.65	0.56	0.27	0.25	0.58
V	39.62	37.95	39.05	39.54	38.93	81.4	84.6	271.6
V (2σ)	0.62	0.65	0.59	0.77	0.63	1.1	1.2	3.4
Rb	31.94	31.05	30.96	31.84	31.36	28.49	28.58	5.63
Rb (2σ)	0.49	0.39	0.46	0.42	0.39	0.71	0.6	0.21
Sr	79.38	76.2	78	79.2	78.44	459.8	475.4	294.5
Sr (2σ)	0.99	1.3	1.3	1.3	0.81	9.5	7.6	5.6
Y	38.38	37.09	38.03	38.47	37.86	10.8	10.68	22.04
Y (2σ)	0.44	0.55	0.54	0.58	0.56	0.29	0.3	0.51
Zr	38.95	37.33	37.98	38.48	37.92	113.4	113.2	113.7
Zr (2σ)	0.73	0.5	0.49	0.61	0.51	1.8	1.9	2.1
Nb	40.52	38.95	40.14	40.33	39.96	6.34	6.72	7.94
Nb (2σ)	0.54	0.62	0.57	0.63	0.44	0.21	0.16	0.24
Sn	38.76	36.91	38	39.2	37.73	2.81	1.98	1.78
Sn (2σ)	0.82	0.82	1	1.1	0.95	0.54	0.17	0.21
Cs	42.51	41.18	42.12	42.31	41.89	1.85	1.904	0.129
Cs (2σ)	0.48	0.52	0.51	0.56	0.66	0.12	0.09	0.032
Ba	40.2	38.68	39.52	40.48	39.67	290.9	303.9	75.4
Ba (2σ)	0.52	0.67	0.74	0.85	0.49	4.8	4.9	1.9
La	36.39	35.06	35.6	36.31	35.7	11.61	11.98	8.3
La (2σ)	0.54	0.55	0.52	0.54	0.51	0.36	0.29	0.3
Ce	39.14	38.05	38.67	39.45	38.46	25.47	26.04	21.8
Ce (2σ)	0.48	0.47	0.55	0.65	0.61	0.66	0.48	0.61
Pr	37.89	36.59	37.18	37.92	37.13	3.03	3.1	3.31
Pr (2σ)	0.57	0.46	0.53	0.77	0.55	0.11	0.14	0.15
Nd	36.58	34.9	35.62	36.46	35.77	15.98	15.92	16.88
Nd (2σ)	0.65	0.71	0.66	0.64	0.73	0.57	0.46	0.57
Sm	39.07	37	38.09	38.72	38.06	2.86	2.75	4.61
Sm (2σ)	0.81	0.74	0.75	0.92	0.76	0.27	0.19	0.42
Eu	36.04	34.16	34.97	35.49	34.85	0.95	0.91	1.47
Eu (2σ)	0.84	0.62	0.61	0.61	0.59	0.11	0.11	0.15
Gd	37.68	35.44	36.1	37.08	36.95	2.35	2.38	4.84
Gd (2σ)	0.82	0.92	0.86	0.91	0.77	0.26	0.25	0.4
Dy	37.05	35.1	35.5	36.63	35.83	2.15	2.11	4.6
Dy (2σ)	0.9	0.74	0.86	0.69	0.8	0.21	0.21	0.28
Ho	38.51	37.04	37.57	38.52	38.07	0.421	0.412	0.844
Ho (2σ)	0.51	0.66	0.66	0.7	0.55	0.049	0.06	0.074
Er	38.67	37.05	37.5	39.02	37.86	1.21	1.12	2.14
Er (2σ)	0.76	0.82	0.78	0.84	0.65	0.14	0.14	0.2
Yb	40.08	38.15	38.74	40.17	39	1.27	1.14	1.92
Yb (2σ)	0.93	0.92	0.71	0.83	0.8	0.17	0.12	0.18
Lu	37.19	36.05	36.6	37.55	36.89	0.141	0.172	0.259
Lu (2σ)	0.37	0.57	0.56	0.65	0.53	0.029	0.034	0.031
Pb	39.9	37.6	37.58	38.78	39.2	9.31	9.38	1.26
Pb (2σ)	1.1	1	0.98	0.91	1	0.44	0.41	0.13
Th	38.12	37.25	37.53	38.58	37.57	2.212	2.38	0.521
Th (2σ)	0.47	0.5	0.56	0.56	0.48	0.088	0.13	0.047
U	37.76	36.77	37.08	38.29	37.18	0.974	0.922	0.418
U (2σ)	0.55	0.6	0.54	0.63	0.5	0.08	0.07	0.044

Appendix IV: LA-ICP-MS raw geochemical data (continued).

Sample:	ML3-2	GOR128-1	GOR128-2	KSC001	KSC002	GF006	GF007	MSE010	MSE017-1
Major element concentrations (ppm)									
Al	72700	52740	51760	57000	57200	68200	68900	70900	67700
Al (2σ)	1100	390	700	1900	2000	3500	3200	3400	3300
K	3168	329.2	329.4	9450	9070	14140	14150	14580	13740
K (2σ)	56	6.9	7.4	180	170	260	290	250	270
Ti	12060	1669	1664	8430	8210	4750	4680	3997	5080
Ti (2σ)	170	22	21	200	170	100	140	99	120
Trace element concentrations (ppm)									
Sc	29.39	31.67	30.09	25.2	24.5	13.86	13.08	12.09	14.86
Sc (2σ)	0.63	0.49	0.45	1.7	1.5	0.91	0.73	0.87	0.97
V	273.1	177.2	180.2	244.4	239.1	171.9	173	135.4	183.3
V (2σ)	3.6	1.8	3.2	5.4	6	4.3	4.8	4.6	4.7
Rb	5.74	0.38	0.381	21.1	21	52.9	49	37.6	48.3
Rb (2σ)	0.19	0.054	0.042	1.3	1.4	1.6	2	2.2	2
Sr	293.6	29.39	29.25	421	417.1	346.4	384.5	326.2	364
Sr (2σ)	6.3	0.62	0.57	11	9.4	8.2	9.1	7.3	10
Y	21.72	11.27	11.03	17.55	21.27	27.4	25.7	11.7	14.39
Y (2σ)	0.42	0.25	0.19	0.87	0.86	1.3	1	0.77	0.96
Zr	112.6	9.21	9.29	113.6	108.4	118.2	120.1	113	117.4
Zr (2σ)	1.9	0.26	0.27	3.9	3.4	2.7	4	3.6	2.8
Nb	8.05	0.099	0.085	18.9	17.96	7.41	7.17	7.21	7.71
Nb (2σ)	0.18	0.02	0.016	1.1	0.91	0.61	0.57	0.58	0.58
Sn	1.69	1.45	1.27	10	4.79	3.82	2.94	3.1	2.95
Sn (2σ)	0.21	0.16	0.12	1.5	0.98	0.96	0.81	0.65	0.73
Cs	0.143	0.222	0.184	0.46	0.32	1.87	1.75	1.53	1.04
Cs (2σ)	0.02	0.026	0.03	0.17	0.13	0.32	0.39	0.28	0.29
Ba	75.7	1.055	0.95	320.2	327.2	512	515	512	475
Ba (2σ)	2	0.061	0.088	7.5	7.8	14	15	15	12
La	8.3	0.121	0.1	23	28.5	41.9	35.2	18.9	20.4
La (2σ)	0.27	0.032	0.023	1.3	1.7	1.4	1.8	1.1	1.2
Ce	22.21	0.452	0.444	40.9	37.4	45.3	41.5	35.7	37.6
Ce (2σ)	0.43	0.055	0.045	1.6	1.9	2.1	1.7	1.7	1.9
Pr	3.03	0.095	0.101	4.93	5.06	8.56	6.2	3.55	4.42
Pr (2σ)	0.13	0.023	0.022	0.5	0.44	0.76	0.49	0.41	0.49
Nd	17.02	0.68	0.59	25.7	25.7	38	27.6	19.2	22
Nd (2σ)	0.57	0.11	0.1	2.1	2	2.6	1.8	1.8	1.8
Sm	4.4	0.55	0.46	4.71	4.8	6.4	3.78	2.39	3.33
Sm (2σ)	0.37	0.14	0.085	0.93	1.1	1.1	0.93	0.79	0.84
Eu	1.53	0.237	0.297	1.19	1.47	1.99	1.44	0.95	1.33
Eu (2σ)	0.14	0.041	0.055	0.27	0.5	0.39	0.42	0.42	0.4
Gd	4.72	1.14	1.03	3.54	3.98	6.2	4.9	2.04	3.05
Gd (2σ)	0.41	0.16	0.14	0.77	0.82	1.1	1.1	0.79	0.95
Dy	4.55	1.94	1.83	2.9	4.2	4.94	3.91	2.04	3.18
Dy (2σ)	0.26	0.16	0.21	0.76	1	0.74	0.88	0.7	0.93
Ho	0.853	0.439	0.381	0.71	0.69	0.92	0.77	0.39	0.59
Ho (2σ)	0.077	0.047	0.039	0.17	0.2	0.22	0.2	0.15	0.19
Er	2.14	1.34	1.46	1.94	2.2	2.88	1.45	1.7	1.56
Er (2σ)	0.22	0.14	0.18	0.43	0.62	0.81	0.45	0.53	0.6
Yb	1.76	1.49	1.3	2.03	1.33	2.93	2.29	0.98	1.85
Yb (2σ)	0.19	0.18	0.15	0.72	0.59	0.63	0.61	0.44	0.64
Lu	0.229	0.212	0.194	0.19	0.29	0.42	0.38	0.2	0.2
Lu (2σ)	0.035	0.032	0.035	0.1	0.15	0.14	0.13	0.14	0.1
Pb	1.31	0.261	0.25	1.92	2.85	3.29	4.6	3.39	3.36
Pb (2σ)	0.16	0.061	0.049	0.42	0.59	0.76	1	0.7	0.68
Th	0.536	0.0058	0.0055	3.36	3.37	6.94	7.08	7.36	6.96
Th (2σ)	0.058	0.0055	0.0052	0.45	0.43	0.7	0.69	0.69	0.7
U	0.402	0.0077	0.0159	0.98	0.93	1.42	1.73	1.43	1.68
U (2σ)	0.032	0.0058	0.009	0.24	0.22	0.32	0.31	0.26	0.32

Appendix IV: LA-ICP-MS raw geochemical data (continued).

Sample:	**MSE017-2**	**MSE018-1**	**MSE018-2**	**MSE019-1**	**MSE019-2**	**MSE020**	**MSE022**
Major element concentrations (ppm)							
Al	68500	74500	73400	73000	72100	72600	73500
Al (2σ)	3300	3900	3200	3500	3600	3800	4200
K	13770	15140	14920	15040	15050	13970	13240
K (2σ)	210	230	210	210	240	220	210
Ti	5080	4250	4300	4279	4308	4190	4860
Ti (2σ)	100	100	82	92	91	110	120
Trace element concentrations (ppm)							
Sc	16.8	9.72	10.15	10.27	11.17	11.6	15.75
Sc (2σ)	1.3	0.82	0.96	0.73	0.98	1.2	0.93
V	188.3	135.7	132.2	135.4	134.5	151.4	197.2
V (2σ)	4.8	3.7	3.7	3.3	3.8	4.9	4.8
Rb	47.3	52.3	53.7	53.7	52.2	48.4	49.6
Rb (2σ)	1.6	2.1	1.8	1.7	1.8	2.3	2.1
Sr	367.8	302.4	300.3	365.3	366.3	353.9	382.1
Sr (2σ)	8.2	7.6	6.1	7.2	8.7	9.6	7.9
Y	14.91	12.01	12.26	15.19	15.2	15.9	16.9
Y (2σ)	0.85	0.66	0.69	0.97	0.79	0.96	0.9
Zr	117.7	122.8	122.9	119.5	123.1	118.1	111.7
Zr (2σ)	3.5	5.3	3	3.3	3.8	4.1	4
Nb	7.61	7.7	8.11	8.04	7.8	7.37	6.98
Nb (2σ)	0.65	0.4	0.74	0.52	0.65	0.61	0.57
Sn	3.46	3.61	3.31	4.1	3.7	1.69	3.32
Sn (2σ)	0.87	0.98	0.85	1	0.93	0.88	0.83
Cs	1.27	1.65	2	1.26	1.26	0.79	1.47
Cs (2σ)	0.24	0.26	0.29	0.27	0.32	0.32	0.32
Ba	483	553	559	601	608	519	481
Ba (2σ)	11	15	13	10	14	14	13
La	20.6	19.8	18.6	23.4	24.1	22.9	21.5
La (2σ)	1.1	1.3	1.2	1.2	1.1	1.4	1.5
Ce	37.6	34.7	35.6	41.4	41.2	43.7	39.3
Ce (2σ)	2	1.8	1.7	1.5	1.6	2.4	2.4
Pr	4.37	3.8	4.22	4.95	5.57	4.44	4.09
Pr (2σ)	0.44	0.49	0.52	0.57	0.59	0.54	0.52
Nd	21.2	20.9	21.6	26	25.4	24.3	23.1
Nd (2σ)	1.9	1.6	1.6	1.7	1.4	2.2	1.6
Sm	3.66	2.79	3.15	4.9	4.5	2.86	4.9
Sm (2σ)	0.99	0.76	0.98	1.4	1.3	0.81	1.1
Eu	1.1	0.97	0.76	1.01	1.23	1.16	0.99
Eu (2σ)	0.39	0.32	0.33	0.32	0.38	0.39	0.35
Gd	3.5	2.28	2.68	3.43	2.51	3.4	4.2
Gd (2σ)	1	0.74	0.93	0.98	0.88	1.2	1.2
Dy	2.77	2.37	1.78	2.42	2.8	2.68	2.5
Dy (2σ)	0.82	0.75	0.67	0.6	0.6	0.83	0.55
Ho	0.52	0.49	0.38	0.37	0.59	0.47	0.55
Ho (2σ)	0.19	0.17	0.11	0.15	0.21	0.17	0.15
Er	1.18	0.94	1.72	1.76	1.37	1.05	1.26
Er (2σ)	0.48	0.43	0.64	0.6	0.39	0.46	0.47
Yb	2.22	1.09	1.39	1.61	1.47	2.12	1.67
Yb (2σ)	0.56	0.38	0.47	0.54	0.57	0.62	0.46
Lu	0.22	0.206	0.13	0.22	0.155	0.33	0.2
Lu (2σ)	0.11	0.091	0.085	0.11	0.098	0.12	0.11
Pb	3.25	4.4	4.8	3.71	3.97	2.45	4.99
Pb (2σ)	0.6	0.76	0.64	0.75	0.67	0.43	0.93
Th	6.73	6.86	6.94	7.32	7.38	6.92	5.92
Th (2σ)	0.85	0.76	0.59	0.83	0.74	0.67	0.71
U	1.37	1.8	1.93	1.77	1.63	1.59	1.53
U (2σ)	0.27	0.4	0.39	0.34	0.38	0.34	0.34

Appendix IV: LA-ICP-MS raw geochemical data (continued).

Sample:	MSE039b-1	MSE039b-2	ORE040	HF043	HF044	MSE045	MSE053	MSE054
Major element concentrations (ppm)								
Al	75200	75300	72600	70200	71300	74200	73800	72200
Al (2σ)	3900	4200	3900	3700	3700	4100	4100	4200
K	16850	16920	13560	13450	13180	14510	13460	13620
K (2σ)	230	280	220	230	240	230	210	250
Ti	4390	4280	4970	4980	4850	4960	5213	4990
Ti (2σ)	110	120	110	110	110	110	94	130
Trace element concentrations (ppm)								
Sc	10.32	9.61	16.3	19.1	17.9	16.7	18.6	17.6
Sc (2σ)	0.76	0.92	1	1.2	1.1	1	1.1	1.3
V	152.9	150.3	205.6	214.5	207.8	197.6	224.4	199.2
V (2σ)	5.2	4.3	5.2	4.9	6.6	4.8	4.6	5.1
Rb	62.9	63.1	48.1	50.8	48.9	49.7	47	48.7
Rb (2σ)	2.6	2.8	2.1	2	2.5	2.4	1.6	1.8
Sr	346.2	348	304.6	330.4	303.1	259.3	406.9	398.6
Sr (2σ)	7	7.1	7	7	6.1	5.3	8.2	7.9
Y	18.8	19.2	74.6	57.8	131.6	17.67	15.95	16.6
Y (2σ)	1	0.73	2.4	1.8	3.6	0.87	0.68	0.87
Zr	140.4	143.4	107.4	112.9	109.6	115.2	115.1	113.2
Zr (2σ)	4.6	3.8	3.8	4.1	3.8	3.9	4.1	3.1
Nb	8.83	8.72	6.84	6.02	6.3	6.51	6.77	5.74
Nb (2σ)	0.54	0.59	0.57	0.62	0.54	0.72	0.64	0.6
Sn	3.16	3.52	2.6	2.3	2.81	3.03	3.02	1.53
Sn (2σ)	0.91	0.86	0.89	1	0.88	0.75	0.97	0.77
Cs	1.08	1.09	1.63	1.56	1.34	2.43	0.98	1.15
Cs (2σ)	0.26	0.25	0.26	0.34	0.26	0.54	0.24	0.24
Ba	604	596	488	567	531	598	469	495
Ba (2σ)	15	13	11	15	16	13	9.7	13
La	28.9	29.1	34.1	48	116.3	19	19.3	20.7
La (2σ)	1.7	1.3	1.8	1.7	3.3	1.4	1.3	1.2
Ce	49.1	47.5	37.6	50.4	54	37.5	37.5	40.9
Ce (2σ)	2.3	2.4	2	2.6	2.6	1.5	1.8	1.7
Pr	6.19	6.66	9.73	12.8	27.1	4.74	4.18	5.74
Pr (2σ)	0.58	0.57	0.76	1.1	1.4	0.56	0.65	0.57
Nd	28.9	28.1	42.1	49.8	97.9	22.1	22	23.4
Nd (2σ)	2.1	1.4	3.1	3.2	3.4	1.8	1.7	2.4
Sm	5.3	4.62	10.2	12.1	21.6	3.5	2.54	3.83
Sm (2σ)	1.3	0.76	1.6	1.4	2.5	1.1	0.72	0.86
Eu	1.15	0.99	3.07	2.74	6.5	0.9	1.11	0.83
Eu (2σ)	0.33	0.33	0.68	0.65	1	0.32	0.31	0.32
Gd	3.8	3.13	12.3	10.3	23.2	2.71	2.1	2.89
Gd (2σ)	1.1	0.85	1.9	1.8	2.2	0.89	0.6	0.73
Dy	3.59	3.04	12.7	8.4	21.1	3.33	2.85	2.96
Dy (2σ)	0.72	0.8	1.7	1.4	2.1	0.89	0.96	0.63
Ho	0.84	0.67	2.44	1.97	4.36	0.53	0.57	0.66
Ho (2σ)	0.27	0.21	0.4	0.36	0.5	0.22	0.15	0.25
Er	1.95	2.05	6.4	6.2	12.6	1.1	1.62	2.01
Er (2σ)	0.59	0.6	1.2	1.2	1.6	0.48	0.58	0.59
Yb	2.51	2	6.4	5.4	10.7	1.98	1.47	1.37
Yb (2σ)	0.72	0.65	1.3	1.1	1.1	0.7	0.47	0.56
Lu	0.31	0.38	1.12	0.84	1.63	0.25	0.28	0.21
Lu (2σ)	0.11	0.16	0.21	0.22	0.33	0.14	0.14	0.15
Pb	6.26	5.73	4.32	4.83	3.84	3.96	5.5	3.77
Pb (2σ)	0.84	0.92	0.8	0.84	0.81	0.65	1.1	0.75
Th	8.61	9.66	5.99	6.31	6.5	6.97	5.68	6.22
Th (2σ)	0.9	0.74	0.83	0.82	0.79	0.56	0.58	0.77
U	1.91	2.15	1.54	1.39	1.36	1.36	1.76	1.72
U (2σ)	0.36	0.3	0.29	0.24	0.26	0.3	0.35	0.29

Sample:	**MSE056**	**MSE057**	**MSE060**	**MSE062**
Major element concentrations (ppm)				
Al	73100	68500	74900	74300
Al (2σ)	3900	3600	4600	4200
K	16200	18970	14170	15800
K (2σ)	220	260	230	190
Ti	4369	4178	5100	4380
Ti (2σ)	90	96	110	110
Trace element concentrations (ppm)				
Sc	11.9	9.39	15.34	11.1
Sc (2σ)	1.1	0.74	0.84	1.1
V	143.4	127.9	202.4	181
V (2σ)	4.7	3.6	5.8	5.6
Rb	58.2	72.2	50.2	57.4
Rb (2σ)	2.4	2.9	2.3	2.4
Sr	263.5	296.9	278.2	343.8
Sr (2σ)	6.3	7.5	7.7	7.3
Y	16.11	16.3	12.86	14.2
Y (2σ)	0.69	1	0.72	1.1
Zr	123.9	146.7	118	136.4
Zr (2σ)	3.8	5.4	3.7	4.9
Nb	7.51	9.35	7.17	7.95
Nb (2σ)	0.64	0.66	0.69	0.7
Sn	1.97	2.23	2.35	2.31
Sn (2σ)	0.82	0.81	0.79	0.84
Cs	1.71	1.83	1.43	1.6
Cs (2σ)	0.29	0.3	0.29	0.26
Ba	615	690	550	603
Ba (2σ)	17	18	14	13
La	27.7	32	16.5	20.1
La (2σ)	1.5	1.7	1	1.5
Ce	42.6	43.4	36	38
Ce (2σ)	2.2	2.5	1.9	1.8
Pr	6.22	6.64	3.79	3.87
Pr (2σ)	0.68	0.66	0.49	0.58
Nd	29.4	27.5	18.8	21.9
Nd (2σ)	2.2	2.2	1.7	2
Sm	4.5	3.81	2.02	2.45
Sm (2σ)	1.1	0.97	0.65	0.85
Eu	1.1	0.7	0.91	0.92
Eu (2σ)	0.37	0.33	0.36	0.34
Gd	3.3	2.94	3	2.88
Gd (2σ)	1.1	0.96	1.2	0.95
Dy	2.77	1.92	2.72	2.63
Dy (2σ)	0.77	0.65	0.71	0.93
Ho	0.47	0.47	0.62	0.41
Ho (2σ)	0.15	0.17	0.21	0.19
Er	1.53	1.71	0.97	1.73
Er (2σ)	0.67	0.56	0.39	0.49
Yb	1.37	1.74	1.3	2.22
Yb (2σ)	0.64	0.67	0.55	0.78
Lu	0.3	0.33	0.19	0.17
Lu (2σ)	0.16	0.14	0.1	0.12
Pb	4.05	4.77	3.58	4.62
Pb (2σ)	0.67	0.75	0.6	0.95
Th	8.31	10.87	6.96	7.64
Th (2σ)	0.82	0.95	0.81	0.63
U	1.63	2.35	1.41	1.98
U (2σ)	0.3	0.4	0.36	0.45

Element	Certified value	±	*n*	Mean	SD	%diff	%RSD
Major elements							
Al_2O_3 (wt.%)	17.8	0.2	2	18.1	0.0472	2%	0.3%
K (wt.%)	1.29	0.02	2	1.73	0.0163	34%	1%
Ti (wt.%)	0.703	0.021	2	0.692	0.0116	-2%	2%
Trace elements (ppm)							
Sc	11.5	0.8	2	10.2	0.0150	-12%	0.1%
V	90.3	6.7	2	83.0	1.60	-8%	2%
Rb	30.7	1.7	2	28.5	0.0450	-7%	0.2%
Sr	482	8	2	468	7.80	-3%	2%
Y	11.4	0.4	2	10.7	0.0600	-6%	1%
Zr	118	3	2	113	0.100	-4%	0%
Nb	6.94	0.25	2	6.53	0.190	-6%	3%
Sn	1.1	0.2	2	2.4	0.42	118%	17%
Cs	1.75	0.11	2	1.88	0.0270	7%	1%
Ba	298	9	2	297	6.50	0%	2%
La	12	0.3	2	12	0.19	-2%	2%
Ce	26.1	0.7	2	25.8	0.285	-1%	1%
Pr	3.2	0.06	2	3.1	0.035	-4%	1%
Nd	13	0.3	2	16	0.030	23%	0%
Sm	2.78	0.05	2	2.81	0.0550	1%	2%
Eu	0.953	0.022	2	0.930	0.0200	-2%	2%
Gd	2.59	0.09	2	2.37	0.0150	-9%	1%
Dy	2.22	0.06	2	2.13	0.0200	-4%	1%
Ho	0.42	0.011	2	0.42	0.00450	-1%	1%
Er	1.18	0.04	2	1.17	0.0450	-1%	4%
Yb	1.13	0.03	2	1.21	0.0650	7%	5%
Lu	0.168	0.006	2	0.157	0.0155	-7%	10%
Pb	10.3	0.9	2	9.35	0.0350	-9%	0.4%
Th	2.28	0.07	2	2.30	0.0840	1%	4%
U	1.01	0.04	2	0.948	0.0260	-6%	3%

Certified Reference Values obtained from Jochum et al. (2005).
The value "n" is the number of replicate data determinations. CV is the certified standard value.
The mean, standard deviation, certified value, and range of concentrations are presented to the same significant figures and units as the certified value.

Element	Certified value	±	*n*	Mean	SD	%diff	%RSD
Major elements							
Al_2O_3 (wt.%)	13.6	0.2	2	13.7	0.000945	1%	0.0%
K (wt.%)	0.385	0.004	2	0.382	0.000542	-0.00738	0%
Ti (wt.%)	2.13	0.09	2	2.01	0.00167	-6%	0.1%
Trace elements (ppm)							
Sc	31.6	1.6	2	29.5	0.145	-7%	0%
V	268	23	2	272	0.750	2%	0%
Rb	5.8	0.21	2	5.7	0.055	-2%	1%
Sr	312	4	2	294	0.450	-6%	0%
Y	23.9	0.7	2	21.9	0.160	-8%	1%
Zr	122	3	2	113	0.550	-7%	0%
Nb	8.61	0.22	2	8.00	0.0550	-7%	1%
Sn	1.14	0.33	2	1.74	0.0450	52%	3%
Cs	0.14	0.012	2	0.14	0.0070	-3%	5%
Ba	80.1	2.2	2	75.6	0.150	-6%	0%
La	8.99	0.13	2	8.30	-	-8%	0
Ce	23.1	0.3	2	22.0	0.205	-5%	1%
Pr	3.43	0.06	2	3.17	0.140	-8%	4%
Nd	16.7	0.2	2	17.0	0.0700	1%	0%
Sm	4.75	0.07	2	4.51	0.105	-5%	2%
Eu	1.67	0.02	2	1.50	0.0300	-10%	2%
Gd	5.26	0.23	2	4.78	0.0600	-9%	1%
Dy	4.84	0.07	2	4.58	0.0250	-5%	1%
Ho	0.906	0.018	2	0.849	0.00450	-6%	1%
Er	2.44	0.05	2	2.14	-	-12%	0%
Yb	2.06	0.04	2	1.84	0.0800	-11%	4%
Lu	0.286	0.006	2	0.244	0.0150	-15%	6%
Pb	1.38	0.07	2	1.29	0.0250	-7%	2%
Th	0.548	0.011	2	0.529	0.00750	-4%	1%
U	0.442	0.018	2	0.410	0.00800	-7%	2%

Certified Reference Values obtained from Jochum et al. (2005).
The value "n" is the number of replicate data determinations. CV is the certified standard value.
The mean, standard deviation, certified value, and range of concentrations are presented to the same significant figures and units as the certified value.

Element	Certified value	±	*n*	Mean	SD	%diff	%RSD
Major elements							
Al_2O_3 (wt.%)	9.91	0.17	2	9.87	0.0926	0%	0.9%
K (wt.%)	0.036	0.005	2	0.040	0.000012	10%	0%
Ti (wt.%)	0.288	0.012	2	0.278	0.000417	-3%	0%
Trace elements (ppm)							
Sc	32.1	1.4	2	30.9	0.790	-4%	3%
V	189	13	2	179	1.50	-5%	1%
Rb	0.406	0.025	2	0.381	0.000500	-6%	0%
Sr	30	1	2	29	0.070	-2%	0%
Y	11.8	0.5	2	11.2	0.120	-6%	1%
Zr	10	0.5	2	9.3	0.040	-8%	0%
Nb	0.099	0.007	2	0.092	0.0070	-7%	8%
Sn	0.224	0.092	2	1.36	0.0900	507%	7%
Cs	0.24	0.025	2	0.20	0.019	-15%	9%
Ba	1.06	0.03	2	1.00	0.0525	-5%	5%
La	0.121	0.004	2	0.111	0.0105	-9%	10%
Ce	0.45	0.016	2	0.45	0.0040	0%	1%
Pr	0.1	0.004	2	0.1	0.003	-2%	3%
Nd	0.784	0.047	2	0.635	0.0450	-19%	7%
Sm	0.525	0.02	2	0.505	0.0450	-4%	9%
Eu	0.264	0.008	2	0.267	0.0300	1%	11%
Gd	1.17	0.04	2	1.09	0.0550	-7%	5%
Dy	1.98	0.07	2	1.89	0.0550	-5%	3%
Ho	0.443	0.019	2	0.410	0.0290	-7%	7%
Er	1.4	0.06	2	1.4	0.060	0%	4%
Yb	1.41	0.06	2	1.40	0.0950	-1%	7%
Lu	0.206	0.009	2	0.203	0.00900	-1%	4%
Pb	0.345	0.043	2	0.256	0.00550	-26%	2%
Th	0.008	0.001	2	0.006	0.0002	-29%	3%
U	0.0121	0.0012	2	0.0118	0.00410	-2%	35%

Certified Reference Values obtained from Jochum et al. (2005).
The value "n" is the number of replicate data determinations. CV is the certified standard value.
The mean, standard deviation, certified value, and range of concentrations are presented to the same significant figures and units as the certified value.

Appendix V:

TIMS Raw Data for Sr and Nd Isotopes

	GF006	KSC001	MRD020	ORE039b	ORE040	AGV-2	987 Standard2	987 Standard3	J&M standard 1	J&M standard 2
$^{84}Sr/^{86}Sr$	0.056488	0.056488	0.056490	0.056492	0.056493	0.056488	0.056492	0.056488	-	-
2σ	0.0000016	0.0000018	0.0000018	0.0000016	0.0000015	0.0000016	0.0000017	0.0000017	-	-
2σ ppm	28	32	31	28	26	28	29	29	-	-
$^{87}Sr/^{86}Sr$	0.704478	0.703850	0.704555	0.704784	0.704645	0.703980	0.710256	0.710256	-	-
2σ	0.0000038	0.0000037	0.0000037	0.0000039	0.0000038	0.0000040	0.0000039	0.0000035	-	-
2σ ppm	5	5	5	6	5	6	5	5	-	-
$^{143}Nd/^{144}Nd$ corrected	0.512810	0.512849	0.512807	0.512771	0.512775	-	-	-	0.511817	0.511819
2σ	0.0000039	0.0000060	0.0000106	0.0000035	0.0000039	-	-	-	0.0000036	0.0000030
2σ ppm	8	12	21	7	8	-	-	-	6.9	5.9